INFORMATION TO USERS

This manuscript has been reproduced from the microfilm master. UMI films the text directly from the original or copy submitted. Thus, some thesis and dissertation copies are in typewriter face, while others may be from any type of computer printer.

The quality of this reproduction is dependent upon the quality of the copy submitted. Broken or indistinct print, colored or poor quality illustrations and photographs, print bleedthrough, substandard margins, and improper alignment can adversely affect reproduction.

In the unlikely event that the author did not send UMI a complete manuscript and there are missing pages, these will be noted. Also, if unauthorized copyright material had to be removed, a note will indicate the deletion.

Oversize materials (e.g., maps, drawings, charts) are reproduced by sectioning the original, beginning at the upper left-hand corner and continuing from left to right in equal sections with small overlaps.

Photographs included in the original manuscript have been reproduced xerographically in this copy. Higher quality 6" x 9" black and white photographic prints are available for any photographs or illustrations appearing in this copy for an additional charge. Contact UMI directly to order.

ProQuest Information and Learning
300 North Zeeb Road, Ann Arbor, MI 48106-1346 USA
800-521-0600

STUDY OF VORTEX DYNAMICS IN HIGH TEMPERATURE SUPERCONDUCTORS USING THE CORBINO GEOMETRY

BY

ANA MAZILU
M.S., University of Illinois at Chicago, Chicago, 2000

THESIS

Submitted as partial fulfillment of the requirements
for the degree of Doctor of Philosophy in Physics
in the Graduate College of the
University of Illinois at Chicago, 2001

Chicago, Illinois

THE UNIVERSITY OF ILLINOIS AT CHICAGO
Graduate College
CERTIFICATE OF APPROVAL

07/17/2001

I hereby recommend that the thesis prepared under my supervision by

ANA MAZILU

entitled STUDY OF VORTEX DYNAMICS IN HIGH TEMPERATURE SUPERCONDUCTORS USING THE CORBINO GEOMETRY

be accepted in partial fulfillment of the requirements for the degree of

DOCTOR OF PHILOSOPHY

W.9. Shmidt

Adviser (Chairperson of Defense Committee)

I concur with this recommendation

Department Head/Chair

Recommendation concurred in:

W.9. Shmidt

Members of Thesis or Dissertation Defense Committee

UIC University of Illinois at Chicago

This thesis is dedicated to my parents, R. and D.-H., who lead my steps towards high education and to my husband, P., without whom my work would have never been completed.

ACKNOWLEDGEMENTS

I would like to thank my committee, J. C. Campuzano, Jim Kouvel, John Marko, Hugo Safar and Andreas Schroeder, for their support and assistance. I would like to bring special thanks to my advisor, Andreas Schroeder, who corrected my thesis and guided me throughout my last research years. I would also like to acknowledge Hugo Safar and Daniel Lopez for introducing me to experimental vortex physics. This work could have not been completed without the help and support provided by Wai-Kwong Kwok and George Crabtree from Materials Science Division, Argonne National Laboratory, where I improved my experimental skills and expanded my knowledge. The theoretical calculations presented in this thesis would have never been done without the help Alex Koshelev. I would like to thank Maria Cristina Marchetti for her many encouraging words and for sharing her ideas with me. There are many others who have been helpful in my professional development: Andra Petrean, Goran Karapetrov, Bob Olsson, Helmut Claus, Valentina Tobos, Lisa Paulius, Daniel Rosenmann, Reginald Ronningen. Thank you all!

TABLE OF CONTENTS

TABLE OF CONTENTS (continued)

LIST OF FIGURES

LIST OF ABBREVIATIONS

LTSC	Low Temperature Superconductor
HTS, HTSC	High Temperature Superconductor
BSCCO	$Bi_2Sr_2CaCu_2O_8$
YBCO	$YBa_2Cu_3O_{7-\delta}$

SUMMARY

A study of the transport properties of $Bi_2Sr_2CaCu_2O_8$, a high temperature superconducting compound, was made using a special contact configuration called Corbino disk geometry. Numerous $Bi_2Sr_2CaCu_2O_8$ single crystals were cleaved and prepared for the transport measurements that were carried out in a He^4 cryostat provided with a superconducting magnet of 12T maximum field capability. The transport experiments consisted of measuring the samples' ac resistivity at various temperature and magnetic fields. Some of the Corbino samples were irradiated with high energy heavy ions in order to study the influence of the irradiation on the vortex dynamics of the superconducting materials.

The transport data of $Bi_2Sr_2CaCu_2O_8$ Corbino samples have been compared with the measurements obtained from a $Bi_2Sr_2CaCu_2O_8$ standard bar sample patterned in the four-probe configuration. No significant difference has been found, indicating that the effect of the surface barriers on the transport properties of the studied material is negligible.

The electrical resistance data from three $Bi_2Sr_2CaCu_2O_8$ Corbino samples with multiple voltage contacts showed evidence of transverse vortex correlation due to shear viscosity in the vortex liquid state. Two of these specimens were irradiated with 2Gev Au ions and then measured again. The samples still show evidence of vortex viscosity. Due to the presence of the irradiated boundaries, information about the correlation length associated with the shear viscosity could be extracted for the first time.

1. INTRODUCTION

Since the discovery of superconductivity in 1911 by H. Kamerlingh Onnes (1), superconductors have been the subject of considerable study, because of their special characteristics of perfect diamagnetism and zero electrical resistivity when cooled below a critical temperature T_c. After more careful investigations, it was established that a superconducting material can expel the magnetic field only if its magnitude is below a critical value H_c (2). Also, these materials are perfect conductors only if the electrical current applied to them does not exceed a critical value I_c (3).

The perfect diamagnetism, or the Meissner effect (2), was explained by the London equations (3), in which an important length scale for the superconductor λ, the penetration length, is defined. This characteristic length gives a measure of the distance on which the magnetic field is attenuated inside the material.

From the Ginzburg-Landau theory of superconductivity (4) arises the second important length scale: ξ, the coherence length, which characterizes the distance on which superconductivity can be recovered. In this theory, Ginzburg and Landau introduced the order parameter ψ, whose magnitude indicates the type of the state, superconducting or normal, at each point of the material. If, for some reason at some point in the sample, the superconductivity is destroyed (ψ=0), the coherence length is the distance around this point on which the magnitude of the order parameter recovers back to the value characteristic of the superconducting state.

For magnetic fields higher than the critical field H_c, superconducting materials cannot totally expel the magnetic field. The magnetic field then starts to penetrate the sample, forcing parts of it to become normal. The energy of the normal-superconductor interface has been calculated and a very interesting consequence follows. Since the interface energy is proportional

to the difference (ξ-λ), it turns out that the relation between the two lengths is very important to the physics of superconductors. If the coherence length is larger, then the interface has a positive energy, which will make its formation unfavorable from the energetic point of view. The materials that satisfy $\xi>\lambda$ are called type I superconductors.

If instead, the penetration length is larger ($\xi<\lambda$), then the interface energy is negative and it will become favorable for the system to form as many interfaces as necessary for bringing the system to an equilibrium state. Using the flux quantization rule (5), which states that the magnetic flux which penetrates the sample is quantized ($\Phi=n\Phi_0$, where $\Phi_0=2.07\cdot10^{-7}Gcm^2$ is the flux quantum and n is an integer), the result is that the magnetic field will enter the sample as bundles of field lines called vortices, each of them carrying only one flux quantum. This way, the maximum number of interfaces will appear to reduce the overall energy. These materials form the type II superconductors group and they exhibit a new state, intermediary between the Meissner and the normal state, called the mixed state.

There is a repulsive interaction between the flux lines, which forces the vortices arrange themselves in a triangular lattice, called the Abrikosov lattice (6). Since it is now possible for the sample to be penetrated by the magnetic field without becoming normal, H_c has no physical meaning anymore. Instead, one has to define the limits for the mixed state; $H_{c1}\approx\Phi_0/4\pi\lambda^2$ is called the lower critical field below which the material expels the vortices, and $H_{c2}\approx\Phi_0/2\pi\xi^2$ is called the upper critical field above which the material behaves like a normal metal and is completely penetrated by the magnetic field.

One can also distinguish two categories of type-II superconductors that are related to the temperature at which each material becomes superconductor - the critical temperature, Tc. There are the low T_c superconductors (LTSC) with critical temperature values up to ~30K and there are high T_c superconductors (HTSC) with critical temperatures from 30K up to 130K. Also, the

coherence length in HTSC is smaller than the one in LTSC, so that the corresponding H_{c2} is larger. A high critical temperature and a large H_{c2} ensures that the mixed state in HTSC provides us with a wide range of temperature and magnetic fields to study its properties.

In the presence of a transport current, the flux tube experiences a Lorentz force $J \times \Phi_0/c$ per unit length. In a response to this driving force, the vortices will move inside the sample and in doing so they dissipate energy (7). The zero resistance, or zero dissipation state, is achieved only in the situation when vortices do not move at all. For this, pinning centers are needed in the material to impede the vortex motion. Fortunately, any imperfection in the underlying crystalline structure acts as a pinning site. No matter what kind of defects there are in the sample, the pinning produced by them is effective only if vortices form a solid phase; that is, if there are strong bonds between the flux lines.

The qualitative difference between the electrical properties of LTSC and HTSC is determined by the thermal fluctuations. A LTSC material becomes superconductor at a temperature where the vortices form a solid state, more precisely a lattice (8); they immediately get pinned by the defects present in the material so that the electrical resistance is zero. In a HTSC, the elevated temperatures keep the vortices in a disordered liquid-like state so that electrical dissipation is finite at all currents. When eventually the resistance vanishes, a phase transition has occurred as the vortices freeze into a solid phase (9).

In summary, in the magnetic phase diagram of HTSC, there is a wide field and temperature range in which there exist novel liquids and solids consisting entirely of magnetic flux lines that possess many of the characteristics associated with normal matter. The vortex liquid to solid phase transition can take place discontinuously, through a first-order phase transition (10-14), when the formed solid is a vortex lattice, or continuously, through a second or higher order phase transition, in which case the vortex solid state is completely disordered. First

order phase transitions occur in clean high-Tc superconducting samples with a low level of disorder. In such systems, phase transitions will be of first order at low magnetic fields, but they will become of second order at high fields. The crossover is determined by the upper critical point, which is further determined by the amount of disorder present in the crystal.

Vortices interact with the environment in a number of controllable ways. One can vary the density of vortices present in a sample by modifying the applied external magnetic field. They can be localized or pinned in place by defects in the underlying crystal or can be thermally set in motion about their equilibrium position by heat. They can also be driven to move in a preferential direction by an applied current. Several novel vortex glassy phases can be obtained by freezing the vortex liquid in a variety of defect environments. The environment could be a random set of point defects, created by irradiating the sample with protons (15) or electrons (16), line defects created by heavy ion irradiation (17), or may be even a periodic defect array, which can be created on the crystal's surface by magnetic decoration (18), vapor deposition (19) and even by etching (20), in which case an array of holes (antidots) is produced. All of these types of defects can be introduced in the system in a controlled way. The vortex matter can be studied in a number of experimentally controllable ways which may not all be possible in atomic solids. One such example is the transformation of a first order transition into a continuous one in the presence of disorder. This problem has theoretically been studied in magnetic systems, however related experiments have been hampered due to the difficulty in introducing quenched disorder into the system in a controlled way. Thus, the vortex matter can be a powerful tool for the study of real matter and also to provide a platform to investigate fundamental problems in the physics of phase transitions.

One of the most often encountered practical applications of the superconductors is the superconducting magnet, which is capable of producing magnetic fields much larger than a regular solenoid carrying the same electrical current. Magnetic resonance imaging (MRI) is

playing an ever-increasing role in diagnostic medicine. The intense magnetic fields needed for these instruments require the use of superconducting magnets. Despite the fact that there are many technological applications of LTSCs, their use is still limited due to the fact that they need liquid helium, which is expensive, in order to be cooled. The discovery of HTSC in 1986 (21) created the possibility of even more technological applications: superconducting generators and motors (22), magnetic shielding devices, energy storage (23), and microwave devices (24). Since the cuprate materials can remain superconducting up to higher temperatures, liquid nitrogen, which is cheaper and easier to use, can be used for cooling instead of liquid helium. However, due to their complex structure, the cuprates have a high manufacturing cost and often develop inhomogeneities, which produce a change in their local superconducting properties - a feature that makes them less commercially viable. Recently discovered, the intermetallic compound MgB_2 with a critical temperature of 39K (25) - high enough to be reached by closed cycle coolers - seems to offer a simpler crystalline structure that could be more easily controlled while manufacturing superconducting devices. However, since this material was just discovered, much research is needed before possible commercial use.

The technological applications of HTSC are primarily hindered by their low critical current densities - the maximum current the material can still carry before losing its superconducting properties. Most technological applications require large current densities in applied magnetic fields. The magnetic behavior of the high temperature superconductors has been the subject of intense study since their discovery. It was found that by increasing the number of defects in the sample, the critical current is increased. The interaction between vortices and defects is not yet completely understood. Due to the fact that it allows control over the number and type of defects introduced, radiation damage (17) is now extensively used to study the vortex-defect interaction.

Most of the electrical transport experiments conducted on HTSC employ samples prepared in the four-probe configuration. The subject of this thesis is to present and analyze issues of the vortex dynamics involved in a different kind of geometry called the Corbino disk geometry. I believe this geometry is special, because it can elucidate aspects of the vortex dynamics that cannot be observed by using a standard bar geometry. Both contact configurations, Corbino and four-probe, are described in chapter 3. A comparison between the two sample geometries is made together with a discussion of the advantages and disadvantages of the Corbino disk over the four-probe configuration. The material used for all Corbino disk experiments from this thesis was $Bi_2Sr_2CaCu_2O_8$ (BSCCO 2212), a layered cuprate with a critical temperature of approximately 88K in the optimally doped state. Due to its layered structure, this high-Tc superconductor is highly anisotropic, having an electrical resistivity in the direction perpendicular to the CuO_2 layers four orders of magnitude larger than the resistivity along the layers. This should be a concern when experiments involving samples with nonuniform current distributions, like the Corbino disk geometry, are carried out. Since the current distribution may affect the experimental transport results, I have developed a model for the estimation of these effects, which is presented in chapter 3.

Chapter 2 contains details about the growth recipes and sample preparation procedures for the two materials used in this thesis, BSCCO and $YBa_2Cu_3O_{7-\delta}$ (YBCO 123) single crystals. It also contains descriptions of the measurement system used for acquiring all data presented in this work and of the irradiation setup and procedure used for exposing the superconducting samples to the heavy ion beam.

Chapters 4,6 and 7 describe the Corbino disk experiments and they represent the main results of this work. Chapter 4 contains the study of the surface barrier effects on the transport properties of BSCCO 2212 using Corbino disk and standard bar samples (26). One of the special

characteristics of the Corbino geometry, which will be explained in detail in chapter 3, is that when electrical current is applied the vortices move on closed trajectories inside the sample and never cross the crystal edges. On the other hand, in the rectangular bar geometry the vortices enter the sample at one edge and exit at the opposite one. Measurements performed on samples patterned into the two different geometries are compared and conclusions about the surface effects are presented.

Chapters 6 and 7 have a common purpose: to show evidence of the vortex matter shear viscosity and extract information about it from the transport data. These experiments involve solely Corbino disk samples. The experiments exploit another important characteristic of the Corbino configuration, namely that the current density along the disk is nonuniform due to the geometry of the current contacts (see chapter 3). A nonuniform current density creates a nonuniform vortex velocity distribution, which provides the possibility of studying the drag between adjacent moving vortices. The experiment presented in chapter 6 shows that there is transverse vortex correlation at high magnetic fields in BSCCO Corbino samples. It cannot however, derive any numerical value for the vortex viscosity due to the fact that the experimental data could not be fitted to the theoretical model that assumes vortex viscosity. This model solves the equation of motion for vortex matter provided that the boundary conditions of the system are known. The boundary conditions could not be specified for the pristine Corbino samples measured in chapter 6.

Chapter 7 solves the problem encountered in chapter 6 by setting the boundary conditions for the vortex motion in the Corbino geometry to zero vortex velocity. This was achieved by irradiating the boundary regions, which coincide with the current contacts, with high-energy heavy ions. The electrical current is fed into a Corbino sample through a point-like contact situated in the center of the disk and is removed at the periphery of the disk. The columnar defects produced in these regions by the irradiation pin down vortices, and therefore,

impose the boundary conditions. A theoretical overview of the model for the hydrodynamic flow of the vortex matter is presented in detail. A very clear similarity is observed between the measurements obtained after irradiation and the model predictions. From the fitting of the transport data with the model, I extracted, for the first time, numerical values for the correlation length for the vortex liquid in BSCCO at various temperatures and magnetic fields.

Since the crystal irradiation was used in chapter 7, I will present a study of the effects of the columnar defects on the properties of high-Tc superconductors in chapter 5. The irradiation technique and setup are described in chapter 2 and the experimental transport results are presented and analyzed in chapter 5. A different number of columnar tracks were introduced into two sets of samples constituted by four $YBa_2Cu_3O_{7-\delta}$ optimally doped single crystals and three YBCO thick films (27). The data analysis shows that the columnar defects are efficient vortex pinning centers, which ensures the boundary conditions required for the experiment performed in chapter 7.

2. MATERIALS AND DESCRIPTION OF THE EXPERIMENTAL SETUPS

2.1 Introduction

This chapter gives information about the synthesizing processes for the two superconducting materials measured in our experiments and describes the irradiation stage together with the electrical measurement setup. The latter was by far the most frequently used system; most of the experimental transport data were obtained by running it continuously throughout the year. The irradiation setup, while also very important, was used only sporadically, every six months or more, whenever a heavy ion irradiation session was scheduled. The cryogenic measurement system is located in the Materials Science Division at Argonne National Laboratory and the crystal irradiation was performed either at the linear accelerator facility ATLAS also at Argonne National Laboratory or at the National Superconducting Cyclotron Laboratory (NSCL) at Michigan State University. The two types of materials used in the electrical transport experiments presented in this work are YBCO 123 and BSCCO 2212 single crystals, both high temperature superconductors with critical temperatures of approximately 94K and 88K respectively. Chapter 5 contains results obtained from measuring a series of optimally doped irradiated YBCO single crystals and the conclusion of that chapter provides the motivation for the main experiment of the thesis described in chapter 7.

The YBCO single crystal preparation was done in the laboratories of the Superconductivity and Magnetism group, from the Materials Science Division in Argonne National Laboratory, and it consists of a long sequence of processes. It usually takes about six full weeks to obtain a good quality detwinned and polished sample ready to use in an experiment. By quality one refers to the magnitude of the crystal's critical temperature and the width of its superconducting transition in zero applied magnetic field. The central subject of the thesis being the Corbino BSCCO samples, studied in chapters 4, 6 and 7, ī will also talk about the way this

type of superconducting single crystals is produced, although I will give fewer details since the actual growing was done by our collaborators.

2.2 Materials

2.2.1 Crystal Growth

One of the collaborating groups, P. Guptasarma and D. Hinks, grows single crystals of $Bi_2Sr_2CaCu_2O_8$ from a travelling solvent floating melt-zone (TSFZ) without crucible contact (28). Polycrystalline rods were consecutively passed twice at growth rates of 10mm/hr and 0.15-0.25mm/hr respectively through a mirror-focussed image of two infrared lamps. Flowing a high purity mixture of 20% O_2 in Ar instead of static air during growth yielded crystals with high as-grown Tc (92K). Oxygen content x of the crystals was varied by annealing in thermodynamically controlled $P(O_2)$ until equilibrium was reached. A second collaborator, K. Kadowaki, grows high quality BSCCO single crystals by the same TSFZ technique (29). However, the as-grown crystals consist of aggregates of thin plate-like single crystal slabs. He finds that the surface of the as-grown boule has a texture running along the growth direction due to extremely anisotropic growth rate of the crystal, which is much faster along the ab-plane than the c-axis. The single crystals are picked up from the boule and the largest crystal obtained is approximately 10mm×10mm×0.1mm. The temperature dependence of the ac susceptibility performed afterwards shows that the critical temperature of the optimally doped crystals is around 89K consistent with our value obtained from transport measurements.

The rest of the section consists of a detailed description of the YBCO growth method. Single crystals of $YBa_2Cu_3O_{7-\delta}$ were grown using the self-flux method (30). I will begin with high purity compounds, $BaCO_2$ (99.999 % pure), CuO (99.999 % pure) and Y_2O_3 (99.999 % pure). A total of about 7.5 grams of these ingredients are weighed with a Y : Ba : Cu molar ratio of 5:27:68. The mixture is then ground with agate mortar and pestle until a uniform powder is obtained. The powder is afterwards pressed with a hydraulic press to a pressure of approximately

3000 psi (pounds per square inch) into a 3/4" diameter, 1/4" tall pellet. The pellet is then placed in the center of a 3" x 3"1.5" gold crucible and the crucible is introduced in a box furnace, centered at 10" from the furnace door, in order to avoid temperature gradients. The crucible is heated up from room temperature to a maximum of 983 °C and then cooled slowly.

Figure 1 shows the temperature program used to grow the crystals in the gold crucibles. The program takes about 6 days to complete. When the program ends, the gold crucible is pulled out of the furnace and the single crystals are visible in the crucible. The cylindrical pellet in the center of the crucible has partially melted and then solidified and it remains at the center of the crucible. The crystals grow everywhere on the bottom of the crucible, but mostly in the corners of the crucible.

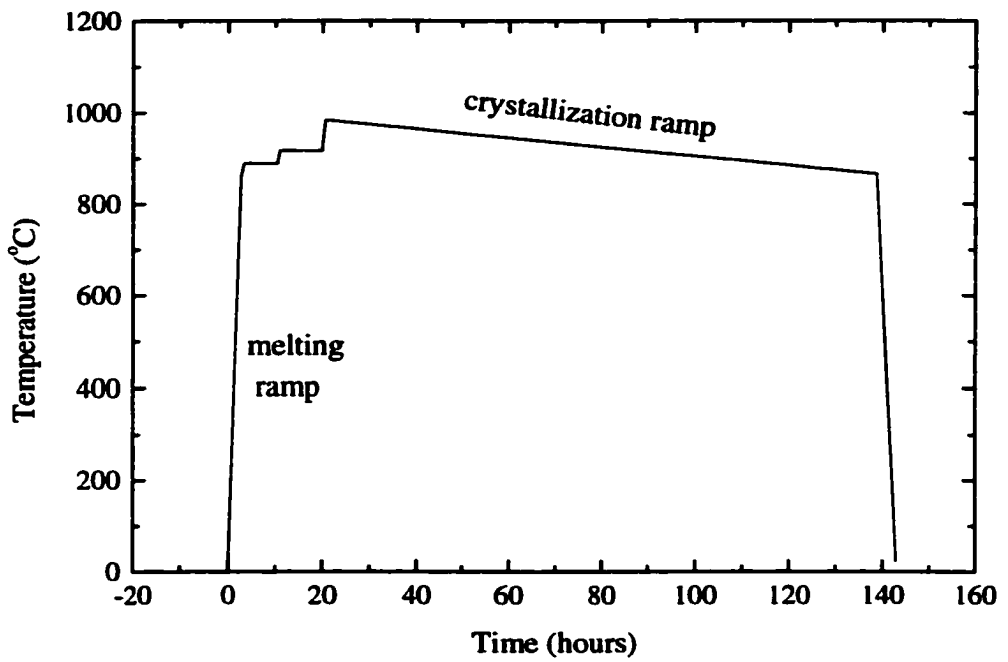

Figure 1. Temperature program for growth of single crystals of $YBa_2Cu_3O_{7-\delta}$ in gold crucibles.

The crystals are extracted from the crucible by turning the crucible upside down and gently tapping from the back. Besides the $YBa_2Cu_3O_{7-\delta}$ single crystals, where parameter suggests that the oxygen doping can vary from batch to batch, a lot of flux and CuO single crystals fall out of the crucible. However, the $YBa_2Cu_3O_{7-\delta}$ single crystals are easy to identify by their typical rectangular parallelepiped shape and black shiny surfaces.

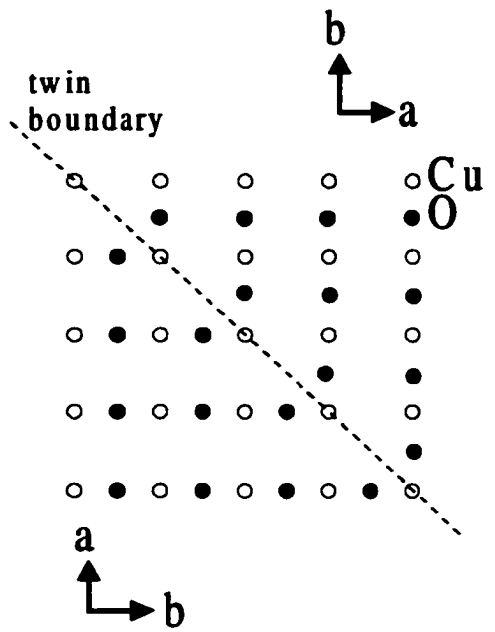

Figure 2. Sketch of the arrangement of atoms in the Cu-O chains in twinned YBCO. A twin boundary (shown as a dotted line) forms when the a and b axis switch from a region to another one in the YBCO single crystal.

At the tetragonal to orthorhombic phase transition, in order to reduce the stress associated with the CuO chains, the a and b direction interchange and create the twin boundaries (see Figure 2). The twinning pattern can be very different from one crystal to another and therefore not only they will influence the results taken on individual samples but also they can make impossible a

comparison between data coming from different crystals. There are studies about the effect of different orientation twins to the transport properties of the YBCO crystals (31), however this is not the subject of the present thesis and therefore we used a thermal mechanical procedure in order to remove the twin defects completely.

The study described in chapter 5 is done on optimally doped YBCO samples, the ones that exhibit the highest superconducting transition temperature. The as-grown single crystals lack oxygen from their structure and so we anneal them for 10 days at 420°C in oxygen flow, after which their typical critical temperature is $T_c \sim 93K$.

2.2.2 Sample Preparation

After the annealing the crystals still contain planar defects in the form of twin boundaries. The twin boundaries are planar structures that most times extend through the whole thickness of the crystal. The twin boundaries in the as-grown crystals can be viewed with a polarized light microscope, as seen in Figure 3.

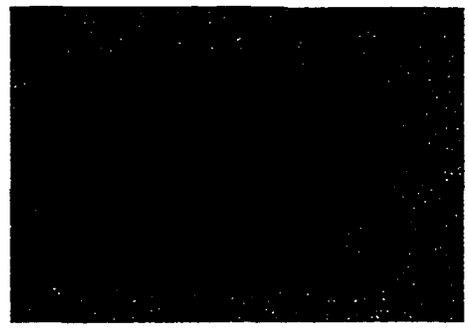

Figure 3. Picture of a partially twinned YBCO single crystal. All the lines that form an angle of 45 degrees with the crystal edges are twin boundaries. Picture was taken through a polarized light microscope with the magnification 10x.

When viewed with a polarized light microscope, the twin boundaries separate two different colored regions, which appear as light and dark gray in Figure 3, where the basal plane is rotated by 90 degrees. In Figure 4 I am showing the picture of a detwinned crystal also taken with a polarized light microscope.

The twin boundaries act as highly anisotropic defect planes, and the effects from the defects introduced by irradiation and those already present due to the twin boundaries would be difficult to isolate. Therefore, it is necessary to remove the twin boundaries in order to be able to study the effects of irradiation-induced defects. The twin boundaries are removed by applying uniaxial pressure in the ab plane (32,33) as shown in figure 5a.

Figure 4. Picture of a fully detwinned YBCO single crystal.

The crystals are placed in a detwinning device where uniaxial pressure is applied with a spring controlled by an adjusting micrometer. The device is placed in a furnace and heated to 420°C in flowing oxygen to ensure that the oxygen content in the crystal does not vary during the detwinning. The applied uniaxial pressure is typically of the order of $\sim 10^7$ N/m^2. The pressure causes the oxygen atoms in the basal plane to align along the b-axis while leaving the basal a-axis

empty of oxygen atoms, as shown in Figure 5b which sketches the arrangement of atoms after detwinning. In this way, the a-axis naturally becomes aligned with the uniaxial stress direction throughout the entire crystal, hence removing the twin boundaries.

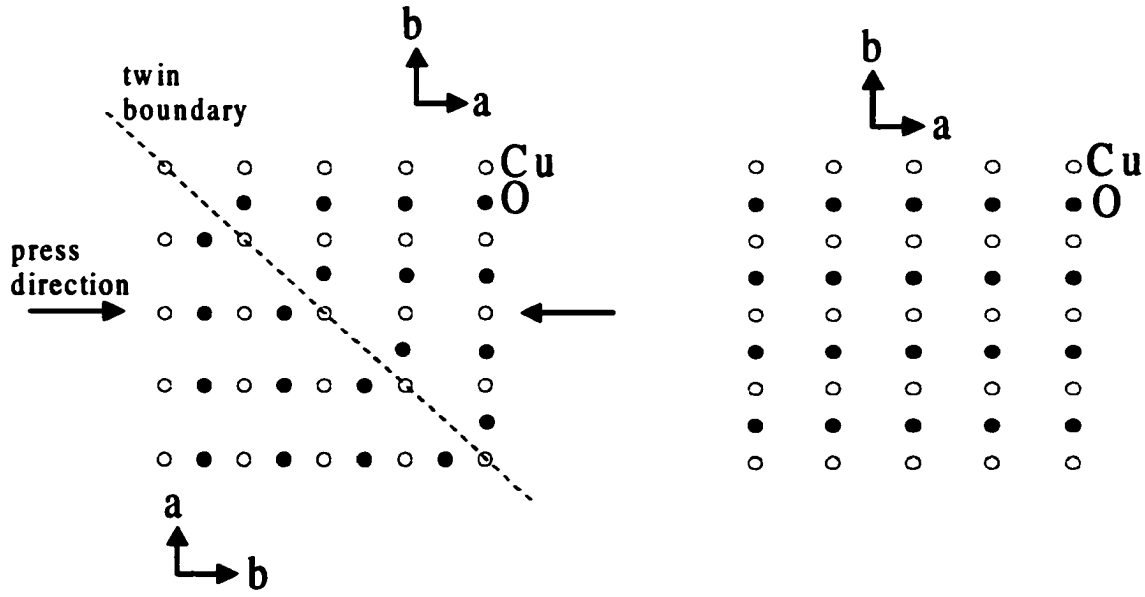

Figure 5. a) Sketch showing the Cu and O atoms arrangement before and after detwinning. The two horizontal arrows indicate the direction on which mechanical pressure is applied during the detwinning process.

For heavy ion irradiation experiments, all crystals, either YBCO or BSCCO, must be thinned to less than 30μm along the c-axis, (for the ion energies usually employed, GeV order) in order to ensure that the heavy ions go all the way through the crystal and produce continuous straight defect tracks throughout the sample. The choice of crystal thickness was based on the results obtained from running the Transport of Ions in Matter (TRIM) Monte Carlo calculation program (34,35).

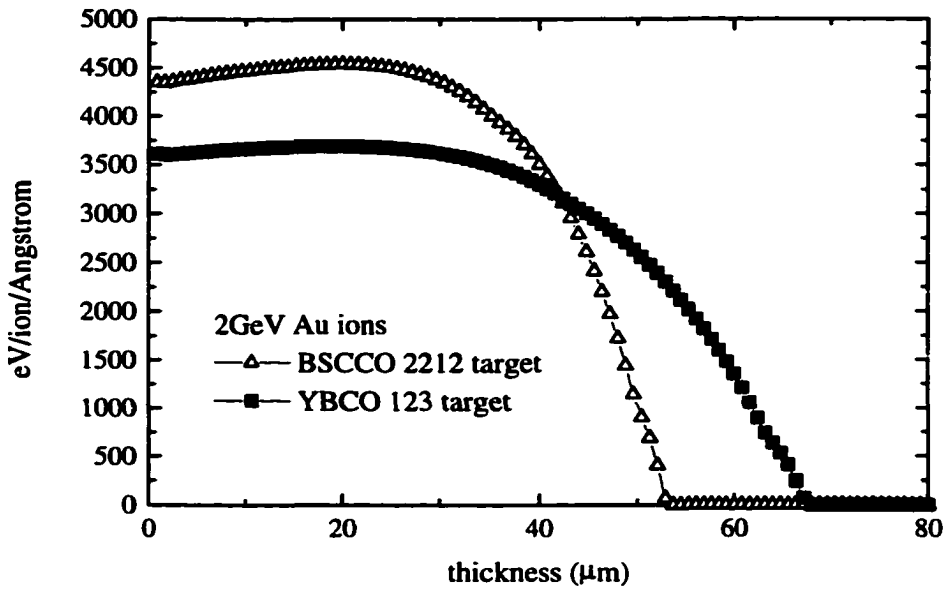

Figure 6. Energy lost by the bombarding ion (Au) per unit length for two types of targets: BSCCO (open triangles) and YBCO (full squares).

This program takes as inputs the ion type, their initial energy and the target material, producing a statistical distribution of the final ion penetration depth and energy transferred to the target material along the ion path. A typical distribution consists of 1000 or more ions simulated trajectories. In Figure 6, I am showing the thickness dependencies of the stopping powers for a gold ion beam with the energy of 2GeV which strikes a 80μm-thick target of YBCO and BSCCO respectively.

The program assumes a random distribution of target atoms with a density of 6.54g/cm^3 for both YBCO and BSCCO in the fully oxygenated state. The results of the simulation show clearly that after the first 30μm inside the YBCO or BSCCO crystal, the stopping power decreases indicating that the ion energy has decreased. As a consequence, the ion trajectories start

to curve, deviating from the initial direction of the incident beam, that is perpendicular to the surface of the crystal, and eventually stopping.

The crystal is thinned by mounting it with crystal bond onto a metal holder and then grinding it using 1 to 30μm grit polishing discs and diamond-in-water suspensions. Final polishing is conducted using 0.1μm diamond suspension. Using this method, flat millimeter-sized crystals less than 30μm thick can be obtained.

2.3 Experimental setups

2.3.1 Measurement setup

Transport measurements are conducted using the Corbino disk geometry as well as the standard four-probe technique, both to be described in the following chapter. Low resistance contacts are necessary in order to obtain meaningful experimental data. Gold contacts, approximately 2000Å thick, are deposited on the crystal using different types of masks by gold evaporation in an evaporation chamber. Crystals are afterwards placed on a substrate made of glass or sapphire and gold wires 12 or 25 μm in diameter are attached to the gold pads using silver epoxy. The samples are then cured for 5-10 minutes at relatively low temperatures, usually around 150° C, in order for the epoxy to get dry, resulting in final contact resistances of about 1 to 5 Ω.

The system used for characterizing the single crystals at low temperatures is shown in Figure 7. The continuous flow cryostat was manufactured by Oxford from a custom design and is capable of reaching temperatures as low as 1.6K. Only the main sections of the ^{4}He cryostat are shown in the Figure 7. It is a top loading system, with a sample chamber diameter of 21mm. The tail of the sample chamber is built of non-magnetic stainless steel and is equipped with a valve, a Cernox temperature sensor, a heat exchanger and a capillary tube which connects the sample chamber to the helium reservoir. When the needle valve is closed, the sample chamber is isolated

from the liquid helium bath by an inner vacuum can. On the other hand, when the valve is open and the sample chamber is pumped continuously, liquid helium flows through the capillary, passes through the heat exchanger where it vaporizes and then reaches the sample chamber as helium gas. The gas is warmed up to the desired temperature by applying current to the heat exchanger and the temperature is measured by the Cernox sensor, all these processes being managed by a temperature controller.

The cooling rate of the sample can be changed by adjusting the liquid helium flow rate and by varying the temperature of the incoming helium gas. For example a high flow rate or a low gas temperature at the heat exchanger will produce a very fast cooling rate of the sample, which could be harmful for the sample contacts. Usually, we maintain a gradient of 2°C between the sample and the heat exchanger and we adjust the pumping rate such that the sample cools down with a constant rate of 0.03°C/minute.

The superconducting magnet surrounding the tail of the cryostat has a 4cm diameter bore and could produce a 11.5 Tesla longitudinal magnetic field. The magnet is controlled with a power supply capable of delivering 120 Amperes. The following steps define the cooling operation down to the 70-100K temperature regime typically employed in studying the high temperature superconductors. The sample chamber, inner, and outer vacuum cans are evacuated with a rotary pump/diffusion pump system to about $\sim 10^{-6}$ Torr. The bath of the dewar is then filled to capacity with liquid nitrogen to pre-cool the superconducting magnet.

The dewar is equiped with two liquid nitrogen sensors, one attached to the bottom of the magnet, the other located one foot above the upper limit of the magnet and an Allen Bradley resistor situated close to the valve. These sensors provide information about the level of the liquid nitrogen such that we do not accidentally overfill the dewar. The Allen Bradley resistor is particularly important since its value can indicate the presence or absence of frozen liquid

nitrogen at the valve. Subsequently, the liquid nitrogen is removed from the dewar by supplying a back pressure of nitrogen gas.

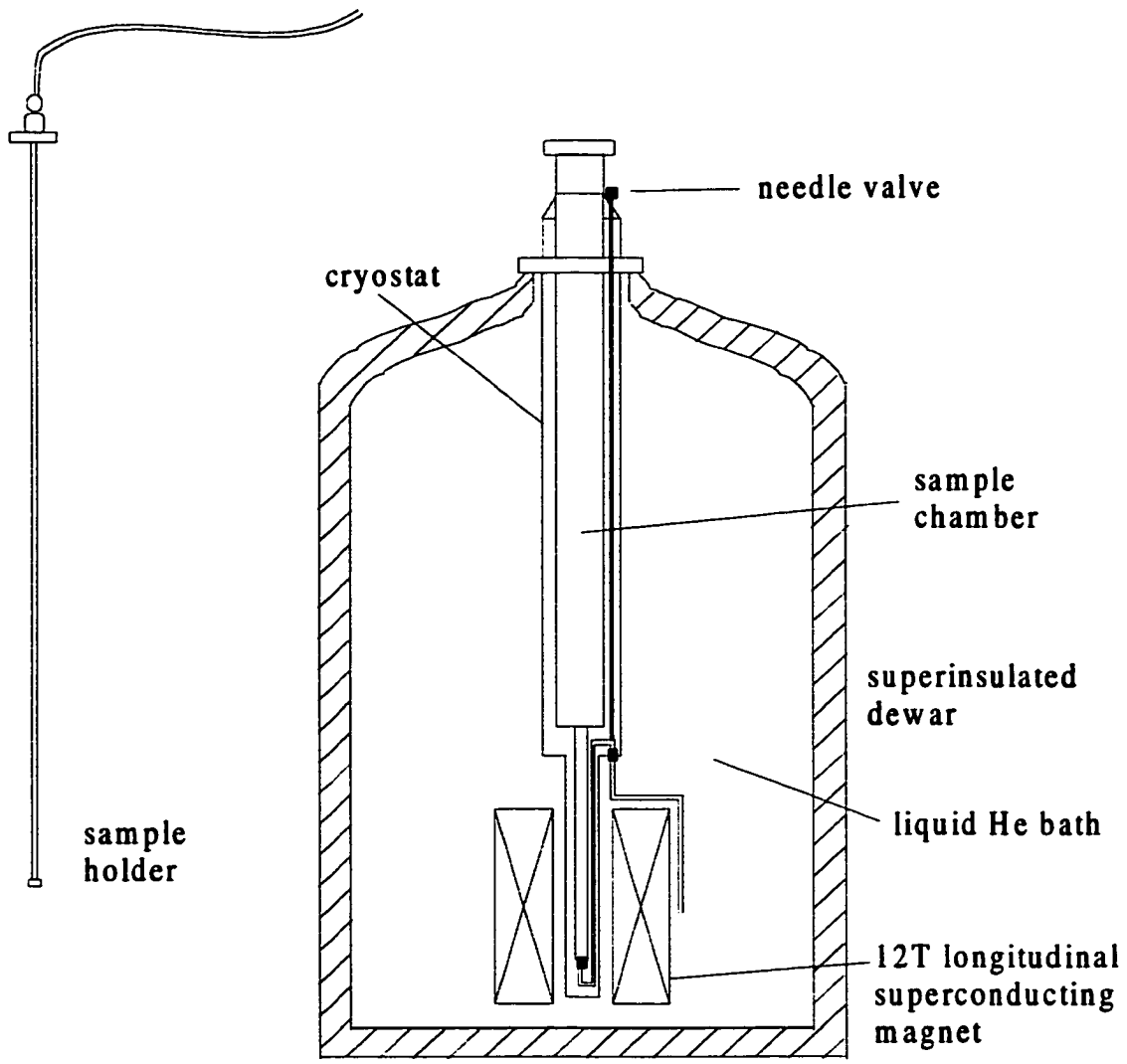

Figure 7. Drawing of the ^{4}He cryostat, dewar and superconducting magnet (right). The capillaries, through which the liquid He reaches the sample chamber, are also shown in the lower part of the cryostat. The sample is positioned in the center of the magnet using a sample holder probe (left). From the probe, the electrical signals are taken by the wires to the various electronics.

When all the liquid is displaced, and we know when this happens by monitoring the lower LiN sensor, the bath is flushed several times with warm ^{4}He gas to ensure that no liquid nitrogen drops remain at the bottom of the dewar. The valve is also opened during the last minutes of this process in order to flush with He gas the capillaries that will ensure the sample cooling later. It is very important to remove all the nitrogen or air that remained caught inside the capillary, otherwise these gasses will freeze when the liquid helium is transferred into the dewar making the functioning of the system impossible. Next, the bath is filled with liquid ^{4}He to capacity. The sample chamber cooling occurs via conduction. Temperature control is maintained locally by a non-inductively wound phosphor bronze heater wire wrapped around a copper cap which surrounds the sample.

The tail of the sample holder probe consists of a Cernox thermometer calibrated from 300K to 0.33 K, a longitudinal Hall probe, an eight-pin receptacle for the sample, and a cap heater consisting of a copper cap wrapped non-inductively with 36 gauge Phosphor Bronze heater wire. The sample holder consists of a G-10 insulating body and Phosphor Bronze posts. In order to perform resistivity measurements the superconducting single crystals are typically mounted on a sapphire or glass substrate with silver epoxy. The sapphire substrate with the sample is then attached to the G-10 disk with varnish. Contacts from the sample to the posts are made with 12 or 25μm gold wire which are attached with silver epoxy to the sample, and attached to the posts with indium solder. The G-10 disk with the sample attaches to a commercially available 8-pin receptacle at the bottom of the probe. Connection from the sample to the top of the probe is made with 14 twisted pairs of 38 gauge copper wire, terminating at a hermetically sealed 32 pin connector at the top. An O-ring slip connection, which connects the probe to the cryostat, enables the probe to be vertically adjustable, so the sample can be placed exactly in the center of the magnet. We can achieve this by previously building a longitudinal field profile using the Hall probe.

In order to measure the ac resistivity of the samples an ac current, usually of 23Hz, is generated by a Stanford Research function generator in series with a 1kΩ resistor. This enables the function generator to provide a constant current source to the sample even though the resistivity of the sample changes drastically as the temperature is reduced. An additional 1Ω resistor in series with the sample is used to monitor the sample current independently. The sample voltage and current (measured across the 1Ω resistor) leads are each connected to a SR 830 lock-in amplifier. For dc resistivity measurements, the function generator and the associated resistors are replaced with a Keithley dc current source and the dc voltage is measured using a Keithley 2001 nanovoltmeter, making sure to reverse the current direction several times to avoid thermal drift voltages.

The data acquisition system consists of a desktop computer connected with the laboratory instruments via an IEEE 488.2 GPIB interface, running LabView data acquisition programs written especially for this measurement system.

2.3.2 Irradiation setup

The coherence lengths for YBCO and BSCCO crystals for magnetic fields parallel to the crystallographic c-axis are 16Å (36) and 30Å (37) respectively at T=0K and they increase with the temperature to approximately 100Å. This length is a measure of the radius of the normal vortex core. The idea of using irradiation in order to produce defects in the crystals came from the fact that the size of the amorphous tracks produced by the heavy ions is comparable to the vortex core dimension. In addition to this, the defect region loses the superconducting properties and therefore it becomes an energetically favorable location for the normal vortex core and this is the reason for which we use the term pinning site for the irradiation defects. And finally, a very important characteristic is that the tracks are linear, much like the vortex shape, therefore it is

expected that this kind of defects, if aligned with the direction of the magnetic field, constitute very efficient pinning centers.

Columnar defects are created in YBCO and BSCCO by the impingement of high energy ions, which cross the thickness of the crystal producing defect tracks. In order for these defects to be linear, the ions must have enough energy to go completely through the sample with only negligible stray from the initial direction, as well as transfer enough energy to the material to create the track. A concern in the production of continuous columnar defects is the stopping power. The energy transfer from the ion to the target material, defined as the stopping power dE/dx, depends not only on the ion type, ion energy and on the target material. From electron microscopy studies a lower limit of approximately 2000eV/ion has been established for the stopping power (38). For stopping powers below this threshold, aligned spherical defects have been produced instead of continuous columnar defects (39). Note from Figure 6 that, for gold ions with the energy of 2GeV, the stopping power is above the threshold. As a result, the defects produced in the experiments presented in this work are truly columnar.

For high ion energies it has been found that the ions interact mostly with the electrons, the nuclear scattering being far less important. As the ion traverses the crystal, it causes local ionization along the path. The atoms located within the now electron-depleted region feel a net repulsive force and if this force is greater than the atomic bond strength, the atoms are displaced along the path. This way, a cylindrical region of defects is established. The track region must be depleted of electrons for enough time as to allow the atoms to repel one another. This criterion is not satisfied for most metals, except for those with a density of conduction electrons less than $10^{20}cm^{-2}$ (40). In addition, the mobility of the created defects must be less than an interatomic distance otherwise the defects would disperse over time.

In order to study the interaction between vortices and defects researchers introduced various concentrations of columnar defects by irradiating the high-Tc superconducting crystals

with heavy ions (17). The heavy ion irradiations were performed at two facilities: The 36" diameter ATSCAT chamber at the Argonne Tandem Linear Accelerator System (ATLAS), located at Argonne National Laboratory, and the N3 chamber at the National Superconducting Cyclotron Laboratory (NSCL) at Michigan State University.

The basic chamber configuration is shown in Figure 8. The samples are placed on a ladder located at the center of the chamber on a rotating pivot, which can also be vertically adjusted. The ladder consists of several rectangular aluminum plates stacked vertically on top of one other, as shown in the lower right corner of Figure 8. A Faraday cup is placed at the back end of the chamber and connected to an electrometer to measure the beam current. During irradiation, the beam current impinging on the samples on the ladder is also monitored with an electrometer. The ions striking the samples produce ejection of surface electrons from the target. For the high-energy ions used in the irradiation the mean energy of an ejected electron is on the order of 250eV (41). To counteract this effect and to obtain an accurate record of the beam current, a suppressor plate with a collimator hole is connected to –300V and is placed in close proximity in front of the target samples. Monitoring the beam current on the conducting suppressor plate helps to steer the beam onto the target. The Faraday cup is geometrically suppressed i.e. any ejected electrons will be collected by the long cylindrical wall of the cup, thereby yielding an accurate reading.

After the sample alignment has been completed, the chamber is closed and pumped down to approximately 10^{-6}torr. The ions enter the chamber with a net positive charge. Given the ion charge Q in Coulomb units, the beam flux can be calculated in the following manner: the beam is adjusted such that almost the entire beam passes through the hole with radius r on the topmost plate of the ladder, and the current I_{FC} is measured by the downstream Faraday Cup. The ion flux F, defined as the numbers of ions per cm^2 per second, is obtained from this current:

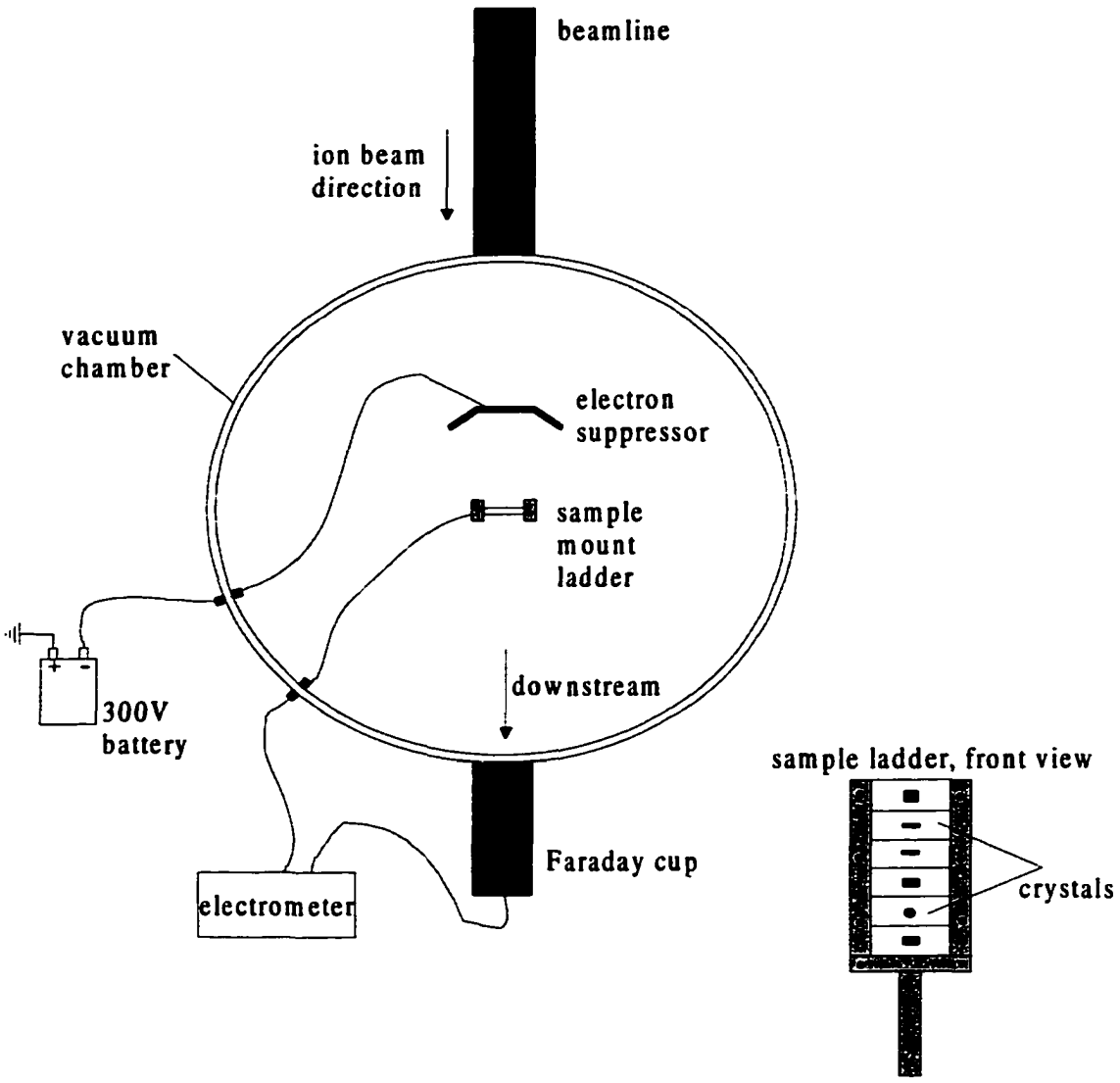

Figure 8. Experimental setup used for the crystal irradiation. The crystals are attached to the sample ladder (lower right corner), which is then positioned in the center of the vacuum chamber on a vertically adjustable pole. The beam passes through the electron suppressor and then hits the ladder.

$$F = \frac{I_{FC}}{QA} = \frac{I_{FC}}{Q\pi r^2} \quad , \tag{2.1}$$

where A is the area through which the ions pass, i.e. the area of the hole in the topmost plate on the ladder. In order to obtain a particular irradiation dose, n, where n is the columnar defect density, expressed in particles per cm^2, the irradiation has to take place over a time t such that n = Ft. Therefore, the time t to obtain a particular irradiation dose is:

$$t = \frac{n}{F} = \frac{nQA}{I_{FC}} \tag{2.2}$$

Any columnar defect density n is equivalent to a matching vortex density from which we can calculate the matching field with the following equation:

$$n = \frac{B_\Phi}{\Phi_0} \tag{2.3}$$

where Φ_0 is the flux quantum and B_Φ is the magnetic field expressed in Tesla units.

An accurate determination of the dose is very important, as the vortex-defect interaction is drastically affected by the ratio between the number of defects and the number of vortices. In chapter 5 we will discuss the influence of the columnar defects on the transport properties of YBCO single crystals. We will show the comparison between data obtained by measuring four samples each irradiated with a different dose.

The main experiment of this work described in chapter 7 uses the knowledge already acquired by numerous experimentalists who studied the direct influence of the columnar defects to the physics of the vortices. I irradiated the Corbino samples in order to study an indirectly related phenomenon. In a way I can call this an "application" of the heavy ion irradiation since I

use it just as a tool for pinning down the vortices in some specific parts of the sample while the measurements are performed in other regions of the same sample.

3. DESCRIPTION OF THE CONTACT CONFIGURATIONS

3.1 Introduction

Much of the research on the cuprate superconductors has consisted of experiments on samples prepared in the four-probe geometry; firstly because it is a standard technique for sensitive transport measurements, and secondly because in the beginning the HTS single crystals could be grown only in small dimensions that could barely fit a few contacts. As soon as the growing techniques improved, experimentalists started to use larger crystals to study the influence that size and shape could have on the transport properties of various HTS materials. The Corbino disk geometry is a novel configuration that requires fairly large specimens. In this chapter, I will describe in great detail the Corbino and the standard bar geometry and in the same time I will compare their features. As we will see, the disk geometry possesses a series of advantages over the rectangular one, fact that makes it possible for us to study aspects of the vortex physics from a new perspective. Later chapters in this work present experiments that treat each of the properties of the circular geometry.

3.2 Description of standard 4-probe geometry

In the four-probe geometry, as the name already announces it, there are a total of four leads; two of them used for inputting the current into the sample and the other two for collecting a voltage signal from the sample (Figure 9).

The reason for which the voltage contacts do not coincide with the current contacts lies in the sensitivity of the resistivity measurements. Since the studied crystals are superconductors, there is a range of temperatures specific to each material when they will exhibit very low electrical resistance, which is possibly orders of magnitude lower than the resistance of the contacts.

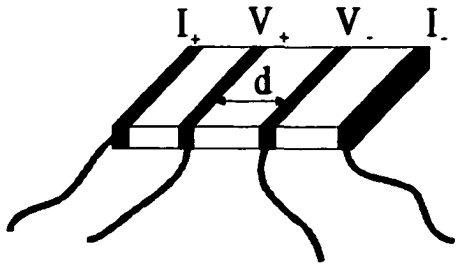

Figure 9. Four-probe measurement configuration also known as standard bar geometry containing two sets of contacts one pair for the current (I_+,I_-) and the other for the voltage (V_+,V_-)

If one measured the voltage from the same contacts as the ones we feed the current through, then the size of the collected signal would be given by the following expression:

$$V_{2probe} = I\,(R_s + R_{contacts}), \qquad (3.1)$$

where I is the inputted current, R_s is the electrical resistance of the superconducting material and $R_{contacts}$ is the total resistance of the contacts. Whenever the material becomes superconducting, its resistance is zero or almost zero, in any case much smaller than the resistance of the contacts.

$R_s << R_{contacts} \rightarrow V_{bad} \equiv IR_{contacts}$ and $V_{bad} >> IR_s$

Therefore, the measured signal does not reflect the behavior of the studied superconductor since this is covered by the large contribution coming from the contacts. In a four-probe configuration the signal measured from the voltage contacts V_+ and V_- is given by:

$V_{4probe} = IR_s + iR_{contacts}$, where i is a very small electrical current generated by the measuring device, in our case a nanovoltmeter or an ac lock-in amplifier. In this expression $R_{contacts}$ is the total resistance of the voltage contacts, however it has a similar value to the one of the current contacts, I_+ and I_-. In the case of the four probe configuration since the contact contribution to the measured signal is very small, we can trust the data as being representative for the electrical properties of the studied material:

$i << I \rightarrow V_{4probe} \cong IR_s$

The current pads cover completely the ends of the crystal so that, under the assumption of a homogeneous crystal, the current density will be uniform throughout the sample. In the vortex liquid phase with an electrical current applied to the sample, there will be a Lorentz force F_L acting on the vortices perpendicular to the current and to the magnetic field direction, see Figure 10. As a result, the flux lines will move across the sample and they will exit it at one side. It is known that the external magnetic field dictates the number of the vortices present in the sample. Since the external magnetic field is kept constant one should have a constant number of vortices penetrating the crystal. Consequently, an equal number of vortices must simultaneously enter the crystal on the other side of the sample, where they are pulled into the crystal by the Lorentz force.

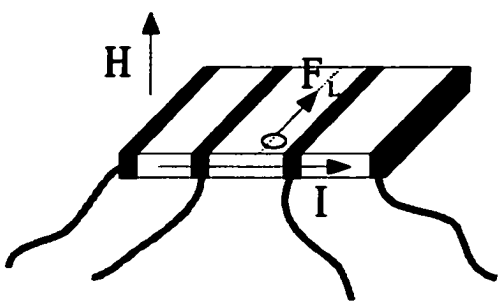

Figure 10. Path followed by a vortex, symbolized by the small circle, in a standard bar geometry in the presence of an applied electrical current I. The Lorentz force, F_L, is perpendicular to the external field H and to the current.

In 1964 Bean and Livingston developed a treatment of the interaction between a flux thread and the specimen surface for type-II superconductors (42). The central result is the existence of an energetic barrier that will impede or slow down the motion of vortices across the

edges of the sample. Because of this, there exist concerns among the experimentalists that the transport measurements obtained using the four-probe technique do not reflect entirely the electrical properties of the bulk of the material since they could contain contributions from the surface effects (43). How large these contributions are depends on the external parameters such as temperature and magnetic field and also on the type and quality of material, and shape and roughness of the sample edges.

The Lorentz force is balanced by a friction force, which is determined by the friction of the vortices with the underlying crystal structure,

$F_L = \gamma v$, where γ is the friction coefficient, (3.2)

such that the flux lines move with a constant velocity. Since the Lorentz force is uniform, the vortex velocity will also be uniform throughout the sample according to the above relation. According to Maxwell's equation, the transversal motion of the magnetic flux lines creates a longitudinal electric field given by:

$$\vec{E} = \vec{B} \times \frac{\vec{v}}{c} \tag{3.3}$$

This produces voltage difference that is collected from the central contacts:

V = Ed, where d is the distance between V_- and V_+ (Figure 9). Thus, the signal is proportional to the number of vortices that move in the space between the voltage contacts and to the speed of the vortices. In other words, the motion of the vortices gives the dissipation in a type-II superconductor, which according to Maxwell's equation creates a voltage along the direction of the current.

The procedure of applying the contacts to a YBCO or BSCCO crystal starts with the cleaning of the surface prior to evaporating gold pads. For obtaining the desired pattern of pads, either slit masks for the four-probe geometry or circular masks for the Corbino samples are placed on top of the crystals. When first deposited, the gold contacts have high resistance. Hence, the gold contacts are subsequently sintered at 420°C in flowing oxygen for approximately six hours to ensure good bonding of the gold to the ceramic crystal surface. The sintering temperature of 420°C period will make sure that the doping of the crystal will still be optimal, so that the superconducting properties of the material are not affected. After that, the process is continued by attaching gold wires to the pads using silver epoxy and curing the sample on the hot plate for about 15min at approximately 150°C. At this point the sample is ready to be mounted on a sample holder which can be attached to the measurement probe and introduced into the cooling system.

3.3 Description of Corbino geometry

A Corbino disk has concentric inner and outer electrical contacts, exhibiting cylindrical symmetry with respect to an axis that passes through the center of the disk and is perpendicular to the disk plane (Figure 11).

Most of the measurements in the presence of magnetic field are usually done applying the field parallel to the symmetry axis of the disk. This type of geometry is named after O.M. Corbino, who in 1911 reported magnetoresistance measurements on several metals using this configuration. The current is fed into the nonsuperconducting sample through the inner pad and removed at the outer frame. In zero applied field, the lines of current are simply radial, but in the presence of an axial magnetic field they lengthen due to spiraling see (Figure 12a and 12b).

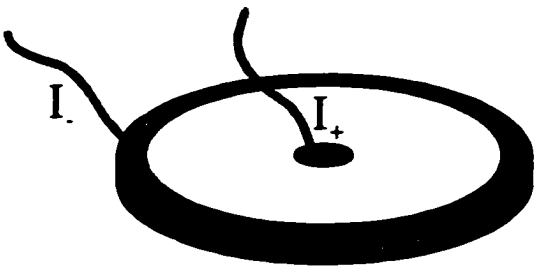

Figure 11. Corbino disk configuration showing the current contacts: the central pad I_+ and the outer frame I_-.

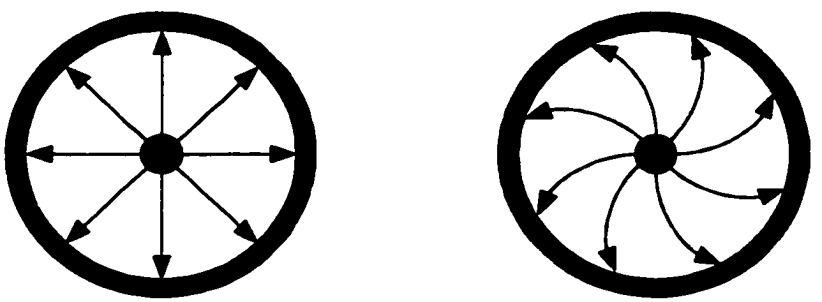

Figure 12. Current distributions in the Corbino disk geometry for the cases of (a) no magnetic field and (b) external field applied perpendicular to the plane of the disk.

This spiraling of the current flow occurs because the geometry of the disk is such that the Lorentz force acting on the charge carriers is not counterbalanced by a Hall-effect electric field. Largely as a result of the geometrical magnetoresistance effect associated with the lengthening of the current path the resistance of the disk increases as indicated by the definition of the electrical resistance. If B is the magnetic induction, the resistance of the Corbino disk can be expressed by the following equation:

$$R(B)=R(0)(1+\tan^2\theta)\rho_{xx}(B)/\rho_{xx}(0) \quad (3.4)$$

where θ, the Hall angle is defined by: $\theta=\rho_{yx}/\rho_{xx}=\mu B$. (3.5)

Here, ρ_{xx} is the in-plane resistivity, ρ_{yx} is the Hall resistivity and μ is the carrier mobility.

Although the Corbino geometry has been around for quite a long time and is used mostly for measuring electrical properties of semiconductors, it has not generally been used for the study of superconductors with the exception of reference (44). In the past five years, there were published only a few experiments involving the normal state properties of high-temperature superconductors using the disk geometry and only recently, concomitant with the development of the present work, have there been reports of experiments done on HTS Corbino samples in order to study different aspects of the vortex physics in the mixed phase (26,45-48).

Given the fact that high-temperature superconductors samples have a platelet-like shape, having the dimensions along the a and b directions much larger than the size along c direction, there is only one way in which the Corbino geometry can be prepared. Namely, the disk plane has to coincide with the crystallographic ab-plane and therefore the symmetry axis of the disk is parallel to the c-axis of the crystal. In our calculations we will use the common coordinate notations xyz, therefore we will need to identify the coordinate axis with the crystallographic directions: ab plane is usually chosen to be the xy plane and consequently the z direction and the c-axis of the crystal are parallel.

In zero external magnetic field, the electrical current, I, flows radially and the current density at distance r from the center of the disk is given by the following expression:

$$J(r)=\frac{I}{2\pi Wr} \quad (3.6)$$

where W is the thickness of the layer where the current spreads. Two assumptions have been made deriving the above relationship: (i) the current flows in a layer of constant thickness W at the surface of the sample and, (ii) for a given r the current density does not vary with z. The current density expression was obtained by writing the definition of the current density for a cylindrical surface of arbitrary radius r that surrounds the central electrical contact.

In the presence of a magnetic field applied parallel to the c-axis of the crystal, the sample will be penetrated by a number of vortices, if it is in the mixed phase. If we imagine a flux line situated at an arbitrary point A in Figure 13, there will be a Lorentz force acting on the vortex that is both perpendicular to the vortex and to the line that connects the vortex and the center of the disk. As a consequence the vortex will move ds to point B in the direction of the driving force. Once here, the Lorentz force will now have a new direction, which is perpendicular to the new vector position of our vortex and, therefore, the vortex will follow again the driving force and it will move to point C and so forth. Thus, the vortex trajectory becomes a circle.

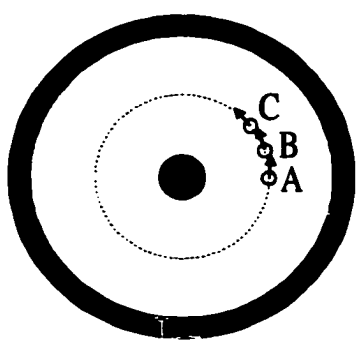

Figure 13. Corbino disk geometry showing a vortex path in the presence of an applied electrical current when the external magnetic field is perpendicular to the plane of the figure.

The Corbino geometry possesses two interesting features. In the present work I will carefully investigate both of them. First, the fact that the current density is nonuniform is providing one with a nonuniform Lorentz force throughout the sample. Consequently, the nonuniform driving force will ensure that the vortices move with different velocities in different regions of the sample or, in other words, the gradient of the vortex velocity will be different from zero. Since there is a velocity gradient it is possible, in principle, to observe and study the vortex shear (see chapter 7).

Second, a distinct advantage of the Corbino geometry is the absence of edges where flux lines enter and leave the sample. In a Corbino geometry the Lorentz force is perpendicular to the disk radius in every point of the sample. Therefore, vortices move on close circular trajectories about the central inner dot, without crossing the edges of the sample. As a result, only the bulk properties will affect the vortex motion with no contribution of the surface effects. In other words, the circular geometry is appropriate for the study of bulk vortex pinning. Moreover, one can compare the results obtained using a standard four-probe sample with the ones coming from a Corbino sample made from the same type of material to draw conclusions about the surface barrier effects, as shown in chapter 4. I should add that the vortices could experience a drag from the top and bottom surfaces of the crystal. However this is true for Corbino as well as for the four-probe configuration, and therefore the effect will be included in the data taken on both configurations. This effect will not alter the conclusions presented in chapter 4 about the edge barriers resulted from a Corbino-four probe comparison.

There are, however, factors that can impede the effectiveness of the Corbino geometry. One is the sample quality, because crystal inhomogeneities will cause vortex trajectories to be irregular-shaped closed loops rather than circles. Inhomogeneities can include regions with structural defects that present different superconducting properties from the rest of the sample, like the critical temperature, or different electrical properties, like the local resistivity value. The

quality of our crystals is investigated, see chapter 4, by probing locally different parts of the disk and comparing the respective measurements. I should add that for a standard bar geometry such inhomogeneities cannot be singled out since the crystal is probed as a whole and the measured voltage will represent a volume average of the sample.

The second factor that could alter the circular trajectory of the vortices is the Hall effect. As we saw from the very definition of the circular geometry, the current lines might get curved which will prevent the Lorentz force from being perpendicular to the radius, and consequently, will prevent the flux lines from moving on circles. In such a case, the trajectories of the vortices will not be closed loops anymore, but they will be spirals. Therefore, the vortices will have to cross the edges of the sample at some point. Under these conditions, the Corbino geometry would become useless.

The Hall effect is caused in the flux flow regime of conventional type II superconductors by the hydrodynamical Magnus force acting on the moving flux lines. A relevant physical quantity is the Hall angle, which corresponds to the angle of the direction of the flux line motion relative to the direction of the Lorentz force. When a vortex moves in a type-II superconductor, dissipation is produced by the scattering of quasiparticles within the vortex core. The finite lifetime, τ, of quasiparticles trapped in the core leads to a broadening of the energy levels. Usually, the spacing $h\omega_0$ between the core levels is so much smaller than the width $1/\tau$, i.e. $\omega_0\tau<<1$, so that it is a good approximation to treat the core as a column of normal material like in Bardeen-Stephen model (49). The discrete nature of the levels becomes important and the dissipative processes have to be considered in the opposite limit, $\omega_0\tau>>1$, which is called the superclean regime. The parameter $\omega_0\tau$ is estimated to be ~14 in 90K YBCO at temperatures below 15K, which places YBCO firmly in the latter regime. Microscopic calculations (50) predict that tangent of the Hall angle θ_H in a pure type-II superconductor increases linearly as $\pm\omega_0\tau$ when

$\omega_0\tau>>1$. The vortex velocity changes from near alignment with J × B towards parallelism with ±J as $\omega_0\tau$ increases (J is the current density and B the field). However, the values of θ_H observed in YBCO mostly at temperatures T>70K are small $|\theta_H|<0.05$ rad and for BSCCO, which is the material used by us for the Corbino samples, even smaller $|\theta_H|<0.006$ rad for 45K<T<90K (51). In conclusion, I can ignore the Hall effect in our experiments.

3.4 Analysis basis for the Corbino data

My typical Corbino sample has a thickness between 15 and 30μm and a radius of 250 to 450μm, so that I can fit four or more voltage probes along one radius as shown in Figure 14a and 14b, the latter being an actual picture of such a sample. In order to investigate different regions of the crystal, voltage contacts are placed along two radii at an angle of approximately 90 degrees to each other. This arrangement also becomes useful during the measurements when some of the voltage contacts deteriorate due to thermal cyclings.

The analysis of the Corbino geometry begins by considering the voltage difference $V_{n,n+1}$ between contacts n and n+1 located one next to each other. From equation (3.6), the current density is given by

$$J(r) = \frac{I}{2\pi W r},$$

so that the electric field

$$E(r) = \rho J(r) = \frac{\rho I}{2\pi W r} \tag{3.7}$$

also exhibits radial variation. From the above expression, it is clear that the electric field strength is largest close to the inner current contact and smaller as we move along a radius towards the periphery of the disk.

Figure 14. a) Corbino disk sketch showing a typical voltage probe configuration. Each small black dot represents a voltage contact. b) Picture of an actual Corbino sample with golden leads attached to the contacts.

The voltage difference is obtained by integrating the electric field on the interval comprised between the chosen contacts:

$$V_{n,n+1} = \int_{n}^{n+1} E(r)dr = \frac{\rho I}{2\pi W} \ln\left(\frac{r_{n+1}}{r_n}\right) \tag{3.8}$$

For the case of a Corbino sample with four radial dots acting as voltage contacts, with $r_1<r_2<r_3<r_4$, where r_n represents the distance between the nth dot and the center of the disk and the innermost contact is r1. If the voltage probes are placed on the radius equidistantly, I can find a strict relation between the values of the signals coming from consecutive pairs of contacts:

$$V_{12}>V_{23}>V_{34}\,. \tag{3.9}$$

This voltage hierarchy can also be readily understood by considering how the vortex velocity varies with the radius;

$$v = F_L/\gamma = J\Phi_0/\gamma c \tag{3.10}$$

$$J(r) = \frac{I}{2\pi W r}$$

From these two equations we can see that the vortex velocity is inversely proportional to the distance from the center of the disk. This means that the flux lines closer to the center of the sample move faster in comparison with the vortices near the outer frame. Since dissipation and vortex motion are equivalent, the faster the motion is the larger the dissipation is and hence, the larger the voltage is. In a Corbino sample, the fastest motion takes place closer to the center of the disk so that we expect that V_{12} will be larger than V_{23} and V_{23} larger than V_{34}, etc.

Expression (3.8) is true if I make some assumptions about the prefactor $\rho I/2\pi W$: namely, the resistivity has the same value everywhere in the sample, that is the sample is homogeneous, and the thickness W where the current flows is also the same at every point. In these conditions, aside from the numerical factor $\ln(r_{n+1}/r_n)$, the signals collected from all pairs of voltage contacts should be identical. If this numerical factor is divided from the measured data correspondingly,

all curves should collapse. This reasoning is true for the case of the normal state of the high-T_c superconductors, where the sample is just a plain circularly shaped resistor and it can also be extended for the vortex liquid regime in which we are sure there is vortex motion and hence dissipation. It would be incorrect, however, to apply it to the case of the vortex solid state.

In the vortex liquid state, the flux lines move freely following the magnitude and the direction of the local Lorentz force; where the Lorentz force is large the vortices move fast and where the Lorentz force is small the vortices move slowly. This motion is called flux flow, and it is characteristic to the vortex liquid state when there is no interaction between vortices and the vortex pinning from various defects in the crystal is very weak. In contrast, in the solid phase, both the vortex-vortex interaction and the pinning effects are strong. Sometimes these interactions can be stronger than the Lorentz force and will alter or completely stop the motion of the flux lines. Whenever the vortex motion is altered, we can no longer expect the hierarchy relation between voltages to be true since the vortices do not follow anymore the Lorentz force, which was the reason behind expression (3.9).

The interaction between the flux lines is the cause for nonzero shear force or viscosity of the vortex matter that, for the case of the Corbino geometry, can lead to the modification of the distribution of vortex velocities along the radius. Recall that vortices move on circular loops about the center of the disk and that the radial profile of the vortex velocity is proportional to 1/r, as depicted schematically in Figure 15.

When vortex matter possesses viscous properties, adjacent moving flux lines can influence each other's speed, thus creating transversal correlation of the vortex motion. By transversal, I mean transverse to the direction of motion so that the correlation takes place along the disk radius.

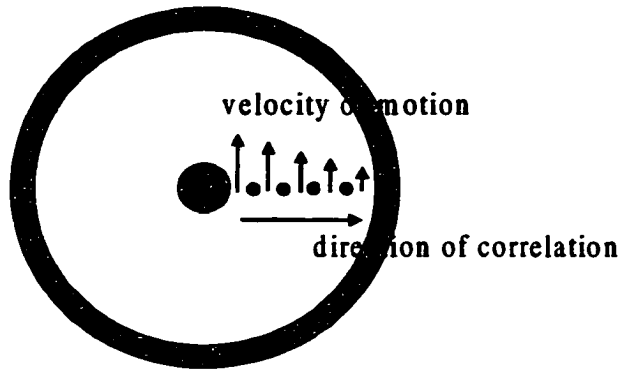

Figure 15. The series of parallel arrows symbolize the velocity vector of the moving vortices. Also indicated in the figure is the direction of motion correlation, which is perpendicular to the direction of motion.

One important consequence is that the distribution of vortex velocities may now be different from 1/r depending on the strength of the vortex shear. It is important to note that in both for a vortex solid and viscous vortex liquid the current distribution will still have a 1/r radial dependence, despite the fact that the vortex velocity will not display this behavior anymore.

3.5 Hydrodynamic treatment of the resistivity

One question that arises after the discussion from the previous section is: what equation describes the vortex dynamics? As soon as this equation is identified, I can solve it with the appropriate set of conditions and actually prove the statements from the above paragraphs. Eleven years ago Marchetti and Nelson developed a theory of the hydrodynamics of the vortex line flow (52). According to the two theorists the motion of flux lines in the vortex liquid state of high-T_c superconductors is equivalent to a hydrodynamic fluid flow. For the case in which a uniform current distribution is applied to a cuprate single crystal, the authors of reference 9 obtain a simplified hydrodynamic motion equation:

$$-\gamma v + \eta \nabla_{\perp}^{2} v + F_L = 0 \tag{3.11}$$

The first term represents the friction force arising from the interaction of the normal core electrons with the underlying crystal structure. Hence, the friction term represents the vortex pinning produced by different types of defects in the sample. The second term is called the viscous drag, η being the viscosity coefficient. Note that it contains the transversal gradient of the vortex velocity. Therefore, in the case of uniform velocity flux flow the viscous drag term will vanish from the equation and the viscosity coefficient cannot be calculated. This supports the statement from section 3.3, that viscosity phenomena can, in principle, only be observed in a sample geometry that allows a nonuniform distribution of vortex velocities. Of course, the Corbino geometry provides such a condition. Finally, the third term of the equation represents the Lorentz force acting on a flux quantum.

In section 3.3, I argued that for the case of the flux flow the vortex lines respond to the local Lorentz force and, since the Lorentz force varies as 1/r, it was expected that the vortex velocity will have the same kind of radial dependence. Let us see whether a 1/r velocity distribution satisfies the hydrodynamic equation. For this, we write the hydrodynamic equation (3.11) in cylindrical coordinates, as indicated by the symmetry of the Corbino geometry. In the same time, we need to identify the components of the in-plane two-dimensional vortex velocity:

$$\vec{v} = v_r \hat{r} + v_\theta \hat{\theta} \tag{3.12}$$

Since the vortices move on circles their velocity direction is perpendicular to the radius, so that only the angular component is different from zero and is inverse proportional to the radius, $v_\theta \alpha 1/r$, and the radial component of the velocity is null, $v_r=0$.

Having done this, we calculate separately the middle term of the hydrodynamic equation since it is the one that requires most attention, the others being rather straightforward:

$$\nabla_\perp^2 v = \nabla_r^2 v = \nabla_r^2 (v_\theta) \alpha \nabla_r^2 \left(\frac{1}{r}\right) = \frac{\partial}{\partial r}\left(\frac{\partial v_\theta}{\partial r} + \frac{1}{r} v_\theta\right) = \frac{\partial^2 v_\theta}{\partial r^2} + \frac{1}{r}\frac{\partial v_\theta}{\partial r} - \frac{1}{r^2} v_\theta = \frac{2}{r^3} - \frac{1}{r^3} - \frac{1}{r^3} = 0 \tag{3.13}$$

Therefore the hydrodynamic equation becomes:

$$-\gamma v + F_L = 0 \tag{3.14}$$

Thus, we find that a velocity inversely proportional to the radius not only satisfies the hydrodynamic equation, but also excludes the possibility of obtaining a numeric value for the vortex viscosity due to the fact that the viscous drag term is equal to zero. Moreover, expression (3.8), which gave the magnitude of the measured voltage signal in a Corbino sample with a 1/r velocity distribution, is also valid.

What about the cases when the vortex motion is not a flux flow, where do we expect to see a deviation from the 1/r behavior? How can we find the velocity distribution under these conditions? All these questions will be answered if we solve the hydrodynamic equation and for that we need to know the boundary conditions. For the Corbino geometry there are two boundaries, inner and outer, both of which are circular. The inner boundary surrounds the central current contact and the outer one is at the interior limit of the frame contact. For a pristine crystal patterned in the Corbino geometry, we cannot specify the boundary conditions. This is the case

described in chapter 6 of this work. In their Physical Review B paper published in 1999, Marchetti and Nelson suggest that the boundary conditions can be created by irradiating the boundary regions with heavy ions (53), to produce columnar defects that pin down the vortices. As a result, a boundary condition of zero velocity can be assumed in the irradiated boundary regions. In this case, presented in chapter 7 of this thesis, the hydrodynamic equation can be solved and expressions for the voltage drops for our contact pairs can be found.

3.6 Anisotropic resistivity model

Before proceeding to the next chapter, I need to make a very important comment. Recall that in order to write the current density as in equation (3.6), we made the assumption that the current flows in a layer of constant thickness W. This approximation may or may not be appropriate depending on the sample thickness and on the material characteristics. One can write the charge continuity equation for an arbitrary point in the sample that is not on any of the current pads:

$$\vec{\nabla} \cdot \vec{J} = 0 \tag{3.15}$$

Knowing that

$$\vec{J} = -\frac{1}{\rho}\vec{\nabla}V \tag{3.16}$$

we can rewrite equation (3.15) in the following way:

$$\frac{1}{\rho_{ab}}\frac{\partial^2 V}{\partial x^2} + \frac{1}{\rho_c}\frac{\partial^2 V}{\partial z^2} = 0$$

or

$$\frac{\partial^2 V}{\partial x^2}+\frac{\rho_{ab}}{\rho_c}\frac{\partial^2 V}{\partial z^2}=0 \quad . \tag{3.17}$$

whereρ_{ab} and ρ_c are the resistivities along the ab-plane and along the c-axis respectively. Here, if we rescale the z coordinate into $z'=z(\rho_c/\rho_{ab})^{1/2}$, then the potential differential equation (3.17) becomes isotropic:

$$\frac{\partial^2 V}{\partial x^2}+\frac{\partial^2 V}{\partial z'^2}=0 \tag{3.18}$$

Of course, in an isotropic material the current propagates the same way in all directions, therefore the above transformation of the z-coordinate can help us find the equivalent length scales in-plane and along the z-axis. In other words, for a material with a large anisotropy, the anisotropy being defined as $(\rho_c/\rho_{ab})^{1/2}$, it is expected that most of the current will flow mainly in the topmost layer of the crystal and that the spreading W on the z-axis is given by:

$$W=\frac{R_{out}-R_{in}}{2}\sqrt{\frac{\rho_{ab}}{\rho_c}} \tag{3.19}$$

where $(R_{out}-R_{in})/2$ is the half of the distance between the current contacts. This is the case for BSCCO, which has an anisotropy of approximately 700 (54). For this type of material, in order to ensure that the current flows in a constant thickness layer, one needs to make the sample very thin, so that the current will spread over the whole z-axis dimension of the sample and so provide a uniform current density. Another way would be to drill a hole through the center of the disk and

then fill it with silver paste so it will constitute the current electrode. This way the current will be forced to distribute uniformly throughout the sample's thickness. All sample drilling attempts were unsuccessful and therefore, the only alternative was to apply the current contact on the top surface of the crystals. In this situation, if the BSCCO crystal is not thin enough, the current distribution would look like in Figure 16, and we believe that this is the case of our Corbino samples.

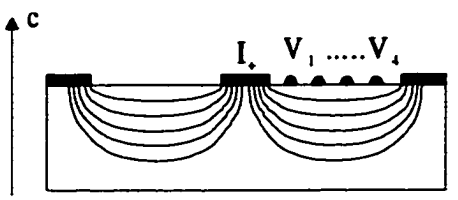

Figure 16. Cross section of a Corbino disk sample made out of a BSCCO 2212 single crystal. Note the curent and voltage contacts at the top of the figure. The curved lines constitute the current distribution for this particular material.

You can see that the thickness of the layer where the current flows varies with the position from the center of the disk and is, therefore, different for various pairs of voltage probes. Clearly in this case, the current distribution will affect the value of the $V_{n,n+1}$ given by expression (3.8). On the other hand, for a material with a moderate anisotropy, for example YBCO, the current tends to spread along the entire thickness of the sample much faster, so that underneath the voltage contacts the current is distributed in an effectively constant thickness layer (see Figure 17). In other words, the latter situation is much closer to the isotropic case, when the current goes everywhere inside the sample, than the former case, as indicated by the corresponding mass anisotropy values.

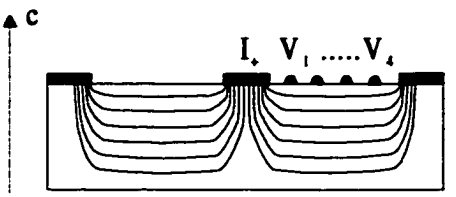

Figure 17. Cross section of a Corbino geometry showing the current distribution if the material the sample is made of is YBCO 123 single crystal.

All our Corbino samples were made out of BSCCO 2212, an extremely anisotropic material. As a result, we expect to see deviations of $V_{n,n+1}$ from expression (3.8). Looking at Figure 16, we see a larger concentration of current lines close to the center of the disk and close to the outer edge. This means that in the above mentioned regions the current density is slightly larger than it would have been if the current had spread uniformly on the z-axis. Since the Lorentz force is proportional to the current density, it will also have higher values than the ideal case in the same regions. As a consequence, one would expect that vortices will move faster and that the voltage drops will be larger than the calculated value for the voltage contacts located in the affected regions; that is, close to the inner pad or the outer frame, namely V_{12} and V_{34}. The middle contact pair voltage, V_{23}, should be the least affected. We would also expect that the order relation (3.9), $V_{12}>V_{23}>V_{34}$, should still be valid. In fact, the anisotropic nature of the sample will enhance V_{12} relative to V_{23}. The deviation from the ideal case will also increase the value of V_{34} above the calculated one. However, the fact that is located further on the radius than V_{23}, still allows V_{34} to be smaller than V_{23}, even if anisotropy corrections are applied. Indeed, we believe that the deviation from due to anisotropy is not strong enough to make V_{34} larger than V_{23}. To support this statement, we apply a linear anisotropic resistivity model developed in 1992 by Busch and collaborators for a four-probe transformer geometry (55).

We start with the charge continuity equation as Busch et al indicate in their paper:

$$\vec{\nabla} \cdot \vec{J} = \frac{1}{\rho_{ab}} \frac{\partial^2 V}{\partial x^2} + \frac{1}{\rho_c} \frac{\partial^2 V}{\partial z^2} = 0$$

to which we attach the proper boundary conditions for the circular geometry. In the above equation V is the potential and ρ_{ab} and ρ_c represent the resistivities parallel and perpendicular to the ab-plane respectively. Note that this model does not take into account the vortices, therefore its boundary conditions are different from the ones used by Marchetti and Nelson (53). This model treats the sample as an anisotropic material without any other special properties and predicts how the current flows inside the bulk. Here the equation is two-dimensional since the potential does not depend on the third coordinate, y. In our case, the Corbino geometry has cylindrical symmetry and therefore the potential will not depend on the polar angle. Thus, we rewrite the differential equation in cylindrical coordinates and we retain only the terms that show a variation along the radius and along the z direction:

$$\frac{1}{\rho_{ab}} \frac{1}{r} \frac{\partial}{\partial r} \left(r \frac{\partial V}{\partial r} \right) + \frac{1}{\rho_c} \frac{\partial^2 V}{\partial z^2} = 0 \quad . \tag{3.20}$$

For our problem, the variable r ranges from zero at the center of the disk to R_{max} at the periphery of the sample (see Figure 18). We also choose that z = 0 at the bottom of the sample and z = t at the top of the sample, where t is the thickness of the crystal.

To correctly solve the problem we need to add the appropriate boundary conditions. We know that the electrical current goes in the sample through the inner pad, that it comes out at the outer frame, and of course, no charge transfer occurs through any other part of the crystal. As a result, we have the following boundary conditions:

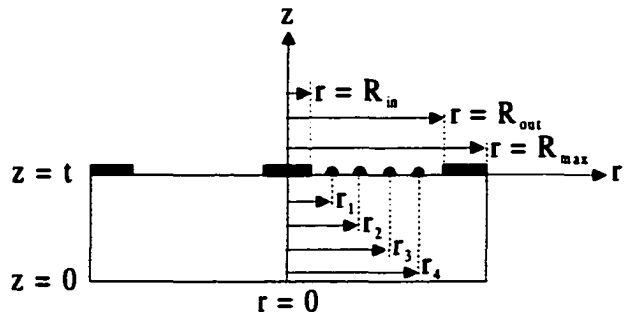

Figure 18. Cross section of the Corbino disk sample indicating the notations used in text for the position of the contacts, etc.

$$1)\qquad J_z(r,z=t)=\begin{cases} I/\pi R_i^2 & \text{for } 0\le r\le R_i \\ 0 & \text{for } R_i<r<R_{out} \\ -I/\pi(R_{max}^2-R_{out}^2) & \text{for } R_{out}\le r\le R_{max}\end{cases} \qquad (3.21)$$

$$2)\qquad J_z(r,z=0)=0 \Leftrightarrow E_z(r,z=0)=0 \qquad (3.22)$$

$$3)\qquad J_r(r=R_{out},z=t)=0 \Leftrightarrow E_r(R_{out},t)=0 \qquad (3.23)$$

Writing

$$V(r,z)=R(r)\,Z(z) \qquad (3.24)$$

and substituting the above expression into the differential equation (3.20) yields

$$\frac{Z}{r}\frac{d}{dr}\left(r\frac{dR}{dr}\right)+\frac{\rho_{ab}}{\rho_c}R\frac{d^2Z}{dz^2}=0 \quad , \tag{3.25}$$

so that a set of two one-dimensional equations is obtained:

$$\frac{1}{rR}\frac{d}{dr}\left(r\frac{dR}{dr}\right)=-k^2 \tag{3.26}$$

$$\frac{\rho_{ab}}{\rho_c}\frac{1}{Z}\frac{d^2Z}{dz^2}=k^2 \quad . \tag{3.27}$$

Here k is an unknown real number. We have put the condition that k is a real number since the solution of our problem, the electrical potential, is a real number. The two independent solutions of the second equation are the exponential functions:

$$Z_1=exp[(\rho_c/\rho_{ab})^{1/2}kz] \quad \text{and} \quad Z_2=exp[-(\rho_c/\rho_{ab})^{1/2}kz] \; . \tag{3.28}$$

The general solution for equation (3.27) is a linear combination of Z_1 and Z_2:

$$Z = a_1Z_1 + a_2Z_2 \tag{3.29}$$

Recalling that $E=-\nabla V$, the second boundary condition $E_z(r,z = 0) = 0$ is equivalent to:

$$\partial V/\partial z = 0 \text{ at } z = 0 \Leftrightarrow R\cdot\partial Z/\partial z = 0 \text{ at } z = 0 \; . \tag{3.30}$$

Now,

$$\partial Z/\partial z = a_1\cdot\partial Z_1/\partial z + a_2\cdot\partial Z_2/\partial z = (\rho_c/\rho_{ab})^{1/2}k\{a_1\, exp[(\rho_c/\rho_{ab})^{1/2}kz]- a_2\, exp[-(\rho_c/\rho_{ab})^{1/2}kz]\}, \tag{3.31}$$

so that the second boundary condition

$$\partial Z/\partial z\,\big|_{z=0} = (\rho_c/\rho_{ab})^{1/2}k(a_1-a_2)=0 \Rightarrow a_1 = a_2 \quad . \tag{3.32}$$

With the two unknown coefficients a_1 and a_2 equal, we obtain:

$$Z(z) = a_1\{ exp[(\rho_c/\rho_{ab})^{1/2}kz] + exp[-(\rho_c/\rho_{ab})^{1/2}kz]\}, \tag{3.33}$$

or equivalently:

$$Z(z) \alpha \cosh\left[\left(\frac{\rho_c}{\rho_{ab}}\right)^{\frac{1}{2}} kz\right] \tag{3.34}$$

The radial equation (3.26) can be rewritten as:

$$\frac{d^2R}{dr^2} + \frac{1}{r}\frac{dR}{dr} + k^2R = 0 \tag{3.35}$$

Changing the variable from r to r'=kr then gives:

$$\frac{d^2R(r')}{dr'^2} + \frac{1}{r'}\frac{dR(r')}{dr'} + R(r') = 0 \tag{3.36}$$

which is the Bessel equation of zero order (ν=0):

$$\frac{d^2Y}{dx^2} + \frac{1}{x}\frac{dY}{dx} + \left(1 - \frac{\nu^2}{x^2}\right)Y = 0 \tag{3.37}$$

Thus, the solution of the radial equation (3.26) is a linear combination of zero order Bessel functions $J_0(kr)$ and $Y_0(kr)$. Since $Y_0(kr)$ tends to infinity as r approaches zero, it is not a viable solution for the electrical potential, which has to be finite at any point.

In conclusion, the solution to the potential equation (3.20) is a sum composed of terms containing the products $J_0(kr)\cosh(\gamma kz)$, where $\gamma=(\rho_c/\rho_{ab})^{1/2}$. Moreover, since there is no restriction on the real number k, the potential has to be written as an integral over k;

$$V(r,z) = \int dk C_k J_0(kr)\cosh(\gamma kz) \tag{3.38}$$

with C_k unknown real coefficients. Our task is now to determine C_k by matching the above solution to the rest of the boundary conditions. For that, we first calculate the z-component of the current density:

$$J_z(r,z) = -\frac{1}{\rho_c}\frac{\partial V}{\partial z} = -\frac{1}{\rho_c}\int dk C_k J_0(kr)\gamma k \sinh(\gamma kz) \quad . \tag{3.39}$$

The first boundary condition tells us that we know the value of $J_z(r,z)$ at the top surface of the sample, meaning at $z = t$

$$J_z(r,z=t) = \frac{1}{2\pi}\int kdk \frac{2\pi}{\rho_c} C_k \gamma \sinh(\gamma kt) J_0(kr) \tag{3.40}$$

If we write the inverse relation of the above expression, by integrating the left and right hand sides over r, we can in principle calculate the value of C_k for any real k:

$$\begin{aligned} \frac{\gamma}{\rho_c} C_k \sinh(\gamma kt) &= \int r dr J_z(r,t) J_0(kr) \\ C_k &= \frac{\rho_c}{\gamma \sinh(\gamma kt)} \int r dr J_z(r,t) J_0(kr) \end{aligned} \tag{3.41}$$

The problem is that there is an infinity of k values. We can ease this problem by noticing that $C_{-k} = -C_k$: since the zero order Bessel function is symmetrical, $J_0(-kr) = J_0(kr)$, and the hyperbolic sine is antisymmetrical, $\sinh(-\gamma kt) = -\sinh(\gamma kt)$, we then have

$$C_{-k} = \frac{\rho_c}{\gamma \sinh(-\gamma kt)} \int r dr J_z(r,t) J_0(-kr) = -\frac{\rho_c}{\gamma \sinh(\gamma kt)} \int r dr J_z(r,t) J_0(kr) = -C_k \tag{3.42}$$

Now let's look again at the expression (3.38) of the potential. If $C_{-k} = -C_k$ then the potential is zero since the integral over all values of k vanishes. In order to have a nonzero potential k must be limited to either positive or negative values. We choose them to be positive.

Note that so far the potential is still an integral due to the fact that we have no restriction on the values of k. As soon as we are able to make the selection that will leave us with only a limited number of k values, the integral transforms into a over a finite k. We turn to the last boundary condition;

$$Er(r=R_{out}, z=t) = 0 \Rightarrow \partial V/\partial r\,|_{r=Rout} = 0$$

or

$$\int k dk C_k \, (dJ_0(kr)/dr)\,|_{r=Rout} \cosh(\gamma k t) = 0 \qquad (3.43)$$

Cleary, it is appropriate to select those k values for which $dJ_0(kr)/dr\,|_{r=Rout} = 0$. This selection eliminates many k values, however we still have an infinity of terms in our sum since there are an infinity of k values for which $dJ_0(kr)/dr\,|_{r=Rout} = 0$. Basically, we can write our potential as a series of products $C_kJ_0(kr)\cosh(\gamma kz)$, where each k corresponds to a frequency. At this point we make a convergence test to reduce the number of terms in the sum. For that we calculated $C_{0.01}$, $C_{0.1}$, C_1, C_{10}, C_{100}. The value of the C_k coefficient decreases between one and two orders of magnitude when k increases by one order of magnitude. As a consequence one can limit the sum to only small values of k. On the other hand, we cannot have too few terms in our sum because the series would be incomplete and the resulting potential shape would be oscillatory, which is incorrect. In the end, I retained 100 terms with k starting at $0.01\mu m^{-1}$ and ending at $1\mu m^{-1}$, with an interval of approximately $0.01\mu m^{-1}$. Thus, the final solution is:

$$V(r,z) = \frac{2\pi}{D} \sum_{k=0.01}^{1} C_k J_0(kr) \cosh(\gamma kz) \qquad (3.44)$$

I wrote a short sequence in Mathematica that can provide the radial profile of the potential at the top of the sample, z=t, and we present this in figure 19 using open symbols. Note that the value of the potential is arbitrary, but the shape of the curve is unique.

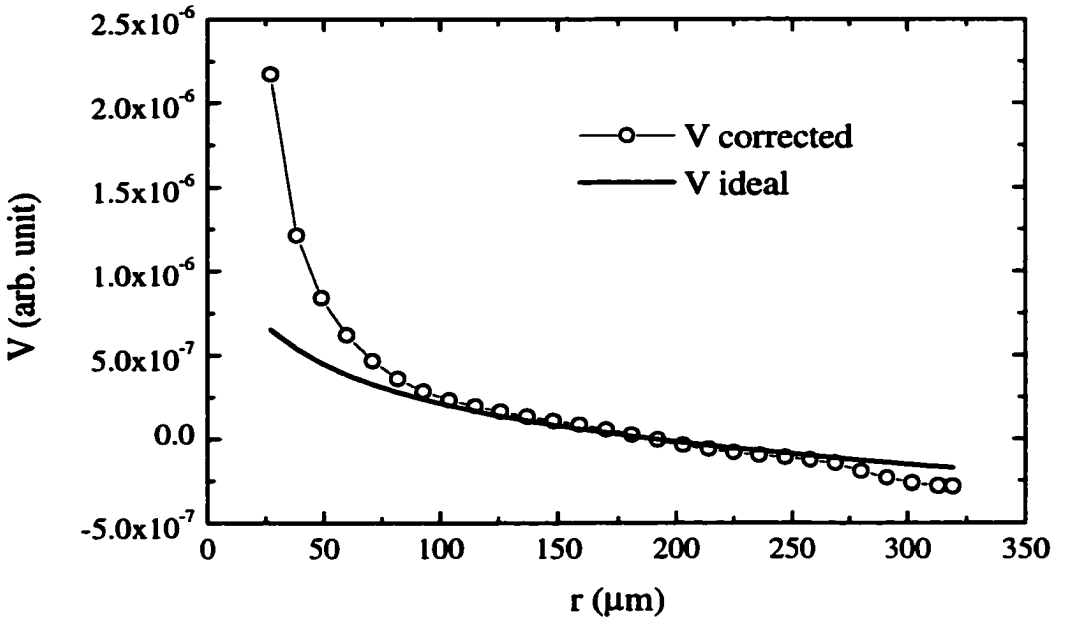

Figure 19. Radial dependence of the calculated potential including corrections due to the current distribution, symbolized with open circles, and the potential obtained from the 1/r current distribution, represented with a continuous line.

In Figure 19, we also show for comparison the potential obtained in the ideal case (continuous line), when the current is distributed in a constant thickness layer at the top of the crystal. As expected, the potential in the middle region of the radius coincides well with the ideal case behavior. In contrast, the center of the disk is very much affected by current spreading, as

evidenced by the larger voltage drop than in the ideal case. The potential at the edge of the disk is also affected by the current distribution, although not as much as the center of the disk. This is due to the fact that at the edge the current density is very small so that even if the current distribution is squeezed into a thin layer at the top of the sample, the potential is not strongly affected. Nonetheless, it is clear that the geometrical factors, $\ln(r_{n+1}/r_n)$, from the expression (3.8) of the potential obtained for a 1/r current distribution are no longer correct for the regions of the sample affected by changes in the current distribution. In fact, the analyzed data measured on a pristine BSCCO single crystal patterned into a Corbino geometry supports this statement.

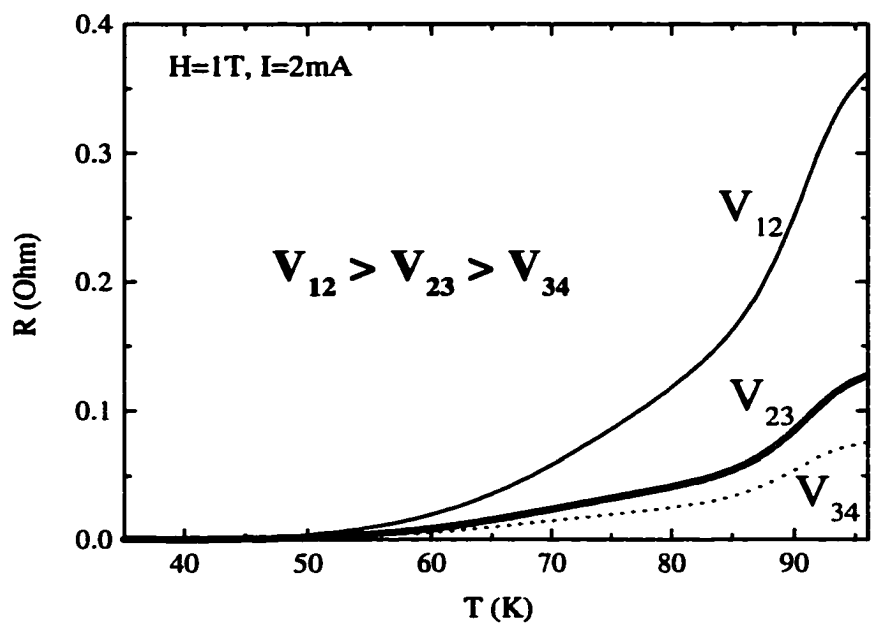

Figure 20. Resistance versus temperature curves of all three radial contact pairs taken on pristine Corbi1 sample with a current of 2mA at a magnetic field of 1T.

In Figure 20, I show three electrical resistance versus temperature curves corresponding to the three voltage pairs taken at a constant magnetic field of 1T. As one can see, the order relation $V_{12}>V_{23}>V_{34}$ is respected at all temperatures. The positions r_n of the voltage contacts are carefully estimated, the maximum error of our measurements being 10μm. Note that due to the fact that the contacts are actually hemispheres of approximately 30μm in diameter, the position of the center of the contact is taken to be r_n. All attempts to make the data overlap by dividing each of the curve by the $\ln(r_{n+1}/r_n)$ factor failed. If, however, we use the scaling factors calculated with our model the curves collapse on top of each other, as shown in Figure 21.

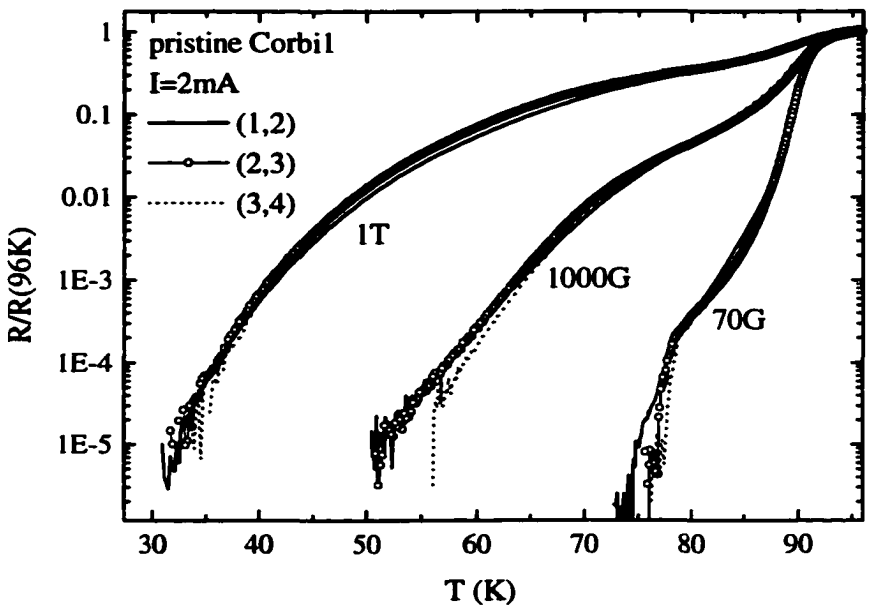

Figure 21. Temperature dependence of the normalized electrical resistance of sample Corbi1 unirradiated for the three radial voltage pairs taken with the same current of 2mA at different applied external fields.

In fact, the scaling is expected to work in all temperature regimes where the high-temperature superconductor is in the normal state or in the vortex liquid state.

Although the Corbino geometry requires more attention in preparation, there are experimental difficulties in applying the dot-like contacts and slight complications in estimating the voltage drop for each contact pair, it is far more interesting than the standard four-probe geometry. The main advantage is that it exhibits a nonuniform current density, which allows one to study the vortex shear. Not many experiments were performed to study this feature. In addition, beside the cited work by Marchetti and Nelson, there is no theoretical modeling or description of the circular geometry. In section 3.6, I have for the first time made calculations for the normal state and the vortex liquid state, because this thesis is only concerned with the liquid state. However, predictions could also be made for the solid state and for the transition to the solid state, where nonlinear phenomena are predominant. For the case of the first order melting transition, it would be interesting to know if the freezing occurs in rings, what are the conditions for slipping motion, etc. I strongly encourage researchers to study thoroughly the Corbino geometry and I hope that the present work will be helpful.

4. COMPARISON BETWEEN THE EFFECTS OF THE BULK PINNING AND SURFACE BARRIERS ON VORTEX MOTION IN THE VORTEX LIQUID STATE

4.1 Introduction

The present chapter will be dedicated to the study of the effect that surface barriers have on the transport properties of BSCCO 2212 single crystals. The experiments designed for this study involve both the Corbino disk and the standard bar geometry. In the previous chapter we described the circular geometry and its advantages. One of the advantages was that the transport measurements from a Corbino sample reveal only the bulk properties of the material with no contribution from the crystal surfaces, due to the fact that the vortices move in circles without crossing the edges of the sample. This characteristic feature of the disk geometry makes it perfect for isolating the bulk from the surface effects. However, measurements using sole the Corbino geometry cannot be conclusive. A comparison needs to be made between a standard bar and a disk sample in order to elucidate if the edge contribution to the electrical transport properties of a superconducting material needs to be taken into account or is negligible. The experimental results of this chapter have been published and can be found in reference (26).

4.2 BSCCO 2212 overview

BSCCO 2212 has a layered structure, which categorizes it as a 2D material. A well-known property of layered high-T_c superconductors is the existence of extended low-temperature tails in the temperature dependence of the in-plane resistivity for magnetic fields applied along c-axis, see Figure 22. For example, in a sample with T_c=88K the vortex liquid has a freezing temperature of 30K for an applied magnetic field of 7T.

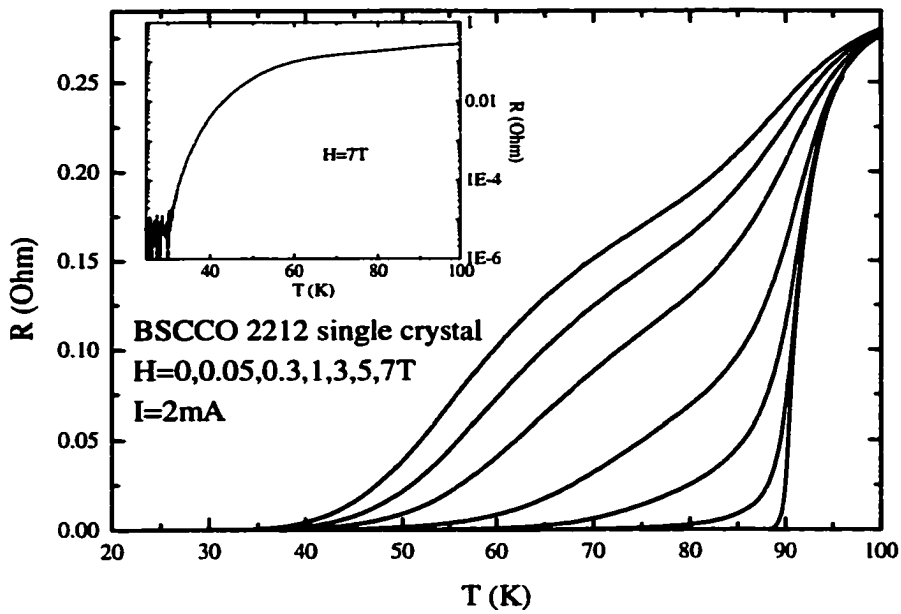

Figure 22. Electrical resistance versus temperature plotted in linear scale at various magnetic fields for a BSCCO 2212 single crystal.

Although the critical temperature is high, as soon as the external magnetic field is turned on, the tail of the resistance versus temperature broadens very much, pushing the regime of zero dissipation towards low temperatures. For this reason, BSCCO 2212 is not a good candidate for applications that require the materials to remain superconducting in the presence of high magnetic fields.

As we already know from the introductory chapter of this thesis, due to the high temperature of the superconducting transition of cuprates, the mixed state is divided into vortex liquid and solid phases. As the high-T_c superconductor is cooled below the critical temperature in the presence of a constant external magnetic field, flux lines start to nucleate in the crystal and form a vortex liquid phase. When we cool the material even more, the vortex liquid undergoes a

phase transition and transforms into a solid. The nature of the transition depends on the applied magnetic field and on the number of defects present in the structure of the crystal. If the system were defect-free, the vortex solid would be a triangular lattice and the transition between the liquid and solid phases would be first-order. If the crystal has a large concentration of structural defects, which can affect the positions of vortices by pinning them down, the solid state will be highly disordered and the transition to it will be of second order or higher. In available BSCCO single crystals, pinning is strong enough to destroy the melting transition in the field range 1-10T. It is widely accepted and proved by J.Fendrich and coauthors (56) that whenever the liquid-solid transition is of the first order, the electrical resistance data show a discontinuity in the form of an abrupt drop from an arbitrary value to zero. We can clearly identify this jump at low fields in Figure 23, which is a semilogarithmic plot to help visualize the discontinuity.

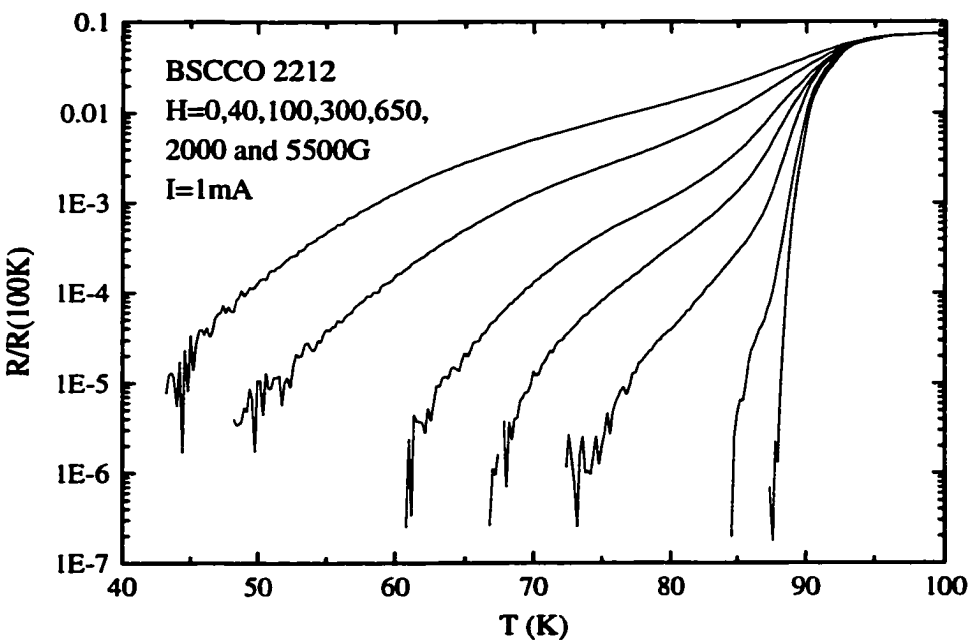

Figure 23. Electrical resistance versus temperature plotted in semilogarithmic scale at various low magnetic fields for a BSCCO 2212 single crystal.

At high fields the jump disappears, leaving a continuous decrease of the resistance until zero is reached. While, for the sample in Figure 23 the upper critical point is approximately 100G, there are publications that show that the so-called upper critical point can actually vary from under 700G down to 0 (57). The magnitude of H_{UP} depends on the number of the defects. If the crystal is very clean, meaning that it has few defects, then H_{UP} will approach the upper limit of the above mentioned range. On the other hand, if the material is dirty or it contains many defects, it is possible that the first order melting is never observed, in which case $H_{UP}=0$. Thus, the upper critical point, which is actually a tri-critical point, is a measure of the single crystal's quality. Another quantity that can provide us information with information about the quality of the material is the critical current. According to the Bean model (58), the size of the critical current increases with the number of pinning sites, which was also obtained experimentally (59).

The work in this chapter is based on the concern that when a type II superconductor is measured in the four-probe configuration the results contain a contribution from the sample edges, as it seems to be indicated by reference (43). I am going to take the following paragraphs to describe what we mean by edge effects.

In 1964, Bean and Livingston developed an elementary treatment of the interaction between a flux quantum and the material surface for type II superconductors (42). When a the flux thread first penetrates a material in the Meissner phase, there are two forces that act on it in the vicinity of the sample edge: (i) the image force from the image flux thread outside the surface and (ii) the Lorentz force due to Meissner currents. In order to satisfy the boundary condition of zero current normal to the surface of the crystal an image flux line of opposite sign is added symmetrically outside the surface. The circular currents around the vortex and its image will combine to give a zero normal component of the current at the surface, as shown in Figure 24.

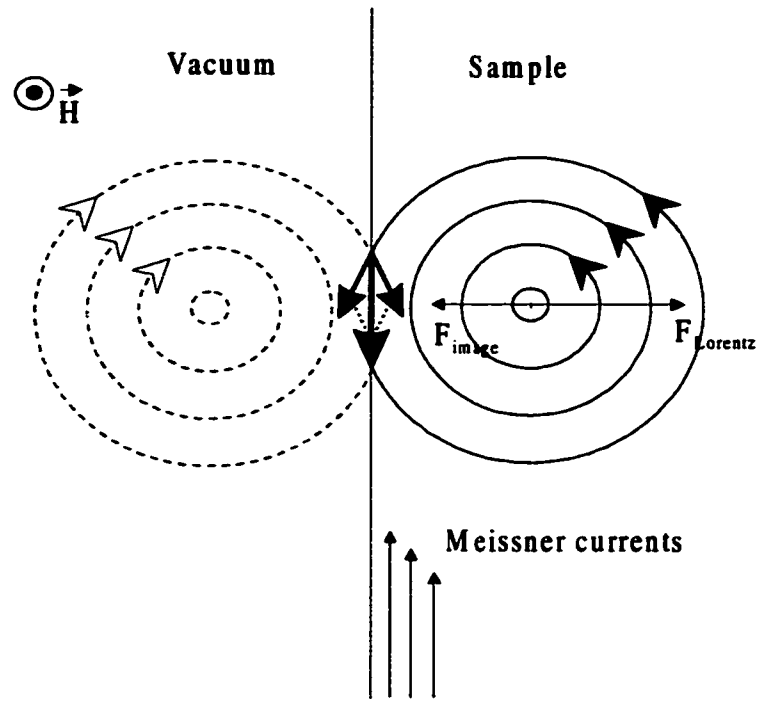

Figure 24. Flux line, right hand side, and its image with respect to the sample edge viewed from above. The external field is applied perpendicular to the plane of the figure, pointing upwards.

Since two vortices of opposite signs attract each other, the flux line is attracted to the surface of the sample. In other words, there is a surface barrier for a vortex that tries to move towards the center of the sample. From expression (4.1) for the interaction energy between two flux threads, we can see that the energy E increases with the distance x from the surface (42):

$$E(x) = \epsilon - (\phi_0/4\pi\lambda)^2 K_0(2x/\lambda) \qquad \text{for } x >> \lambda . \tag{4.1}$$

In this expression, ϵ is the energy per unit length of a single flux line far from the surface, ϕ_0 is the flux quantum, K_0 is the modified Bessel function of zero order, and λ is the penetration length.

Since the material is in the Meissner phase, there are screening currents flowing at the edges of the sample perpendicular to the direction of the external magnetic field. Due to these Meissner currents, a flux line that just penetrated the sample will feel a Lorentz force, which will push it away from the surface. Thus, this interaction produces a repulsive force from the surface, therefore balancing the image force. The energy of the interaction due to the Lorentz force is given by (42):

$$E'(x) = \phi_0 H e^{-x/\lambda} / 4\pi . \tag{4.2}$$

After adding the two contributions from expressions (4.1) and (4.2) and studying the spatial variation of the result with the applied magnetic field, we see that there is an energy barrier to flux motion into or out of the sample for low fields that are larger than H_{c1}, the lower critical field. Due to this energetic barrier, the surface of the sample acts as a pinning center for the flux lines. This is the surface effect that might influence the transport properties of vortices in crystals patterned into standard bar geometries. I should add that the above treatment was developed for a single flux line, while in most of the cases the external magnetic field has such a value that there is a considerable number of vortices in the superconducting sample. However, the Bean-Livingston barrier gives us a good idea about the mechanism of the surface pinning.

The Bean-Livingston barrier, discussed above, was developed for a flat interface. Any irregularity of the sample edge can modify the local surface barrier energy making it harder or easier for the flux line to penetrate the sample, depending of the shape of the irregularity. There is

another contribution to the surface effect, which is called the geometrical barrier, and is due to the shape of the cross section of the sample (60).

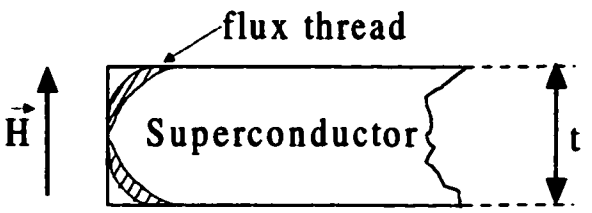

Figure 25. Initial stage of the vortex penetration at the superconductor's edge.

While Bean and Livingston's treatment starts with a vortex next to the surface, which has already penetrated the sample, the geometrical barrier refers to the actual process of crossing the edge of the sample. For a sample with flat surfaces and thickness t, the vortices initially cut through the sharp rims of the crystal without complete penetration, thus effectively rounding off the curvature of the flux lines on the order of t/2, as shown in Figure 25. As a result, in the edge region the vortex energy increases from zero to a maximum value of $\epsilon_0 t$ at a distance t/2 from the surface due to the lengthening of the flux line. This increase in energy constitutes the geometrical barrier that also acts as a pinning center for the vortices.

In this work, I will not distinguish between the two types of surface barriers, but I will treat them together as a surface effect on the transport properties of BSCCO single crystals.

4.3 Quality check and experiment description

The experiment consists of comparing the electrical transport properties of a BSCCO single crystal patterned into a Corbino geometry with the ones of a standard bar geometry made

out from the same material. As I said before, the measurements from a disk geometry reflect information only about the material's bulk properties, while the data from a four-probe configuration contains both bulk and surface contributions. The two resulting sets of data are compared and conclusions are then drawn about the effect of the surface barriers on the transport properties of BSCCO 2212. I prepared the samples out of BSCCO 2212 grown using a modified floating-zone process in a double-mirror image furnace with an external home-built control for very slow growth (28). After repeatedly cleaving the original crystals, I selected thin platelet crystals of about 1mm×1mm×20μm on which the electrical contacts were painted using silver epoxy for each of employed configuration, Corbino and four-probe. Often, the quality of the BSCCO crystals varies a lot, even if the crystals belong to the same batch, this material being very susceptible to variations of the oxygen concentration.

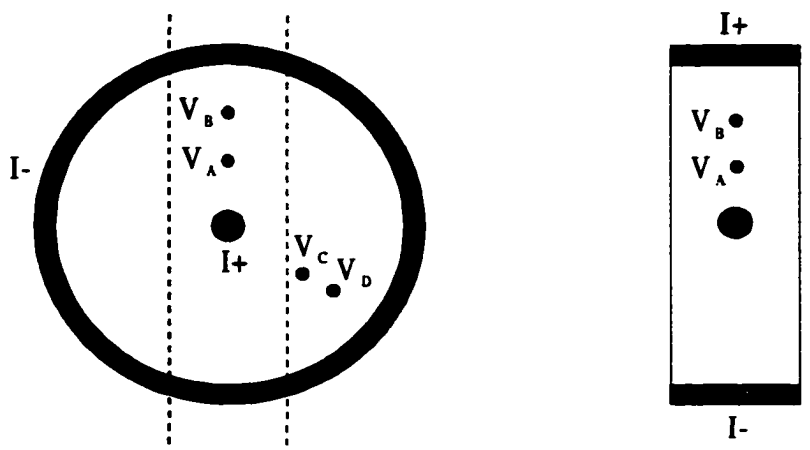

Figure 26. a) the Corbino disk configuration and b) standard bar geometry obtained from cutting the disk along the dotted lines. Voltage contacts V_A and V_B and segments from the outer circle are conserved throughout the experiment.

Therefore, if we compare the properties of two different crystals, possible intrinsic differences between the two specimens could be wrongfully attributed to the change of geometry. I prepared a total of eight samples, both in the disk and standard bar geometry. However, the most convincing experiment consists of measuring the transport properties of a crystal in the Corbino geometry and cutting it afterwards into a rectangular shape, as shown in Figure 26a, so that it could be further measured in the four-probe configuration. For current injection, I used the remainder of the disk's frame contact and, for voltage contacts, a conserved pair of radial contacts from the Corbino geometry. In this manner, the very same crystal with the same underlying properties can be studied in both contact configurations. This experiment can be performed for any superconducting material for the same purpose of studying the surface barrier effects. The Corbino geometry, in particular, can be used for many other interesting experiments such as transverse vortex correlation (see in chapter 7).

As we stated in the previous chapter, the Corbino geometry works properly if the crystal is homogeneous. Before I start the final data analysis and interpreting the results, we should check the quality of the Corbino sample; that is, the crystal patterned into the Corbino geometry. For this purpose, it is required to have voltage contacts placed on different radii, as shown in figure 26. This way, we can probe different regions of the crystal and compare them to each other. If the sample is homogeneous, then the transport data taken at different contact pairs will be similar. I have performed such a quality check on our disk samples and the result is presented in Figure 27. Since all contacts were applied by hand, their radial positions are slightly different from one pair to the other. Thus, from expression (3.8) it is clear that all voltage drops will be different, making it difficult to compare raw data taken from different contact pairs. For the purpose of comparison, in Figure 27 I have plotted normalized resistance data versus temperature at different applied magnetic fields. In the inset of Figure 27, the comparison between the

electrical resistances of the two radial pairs, (V_A, V_B) and (V_C, V_D) respectively, at zero field is presented.

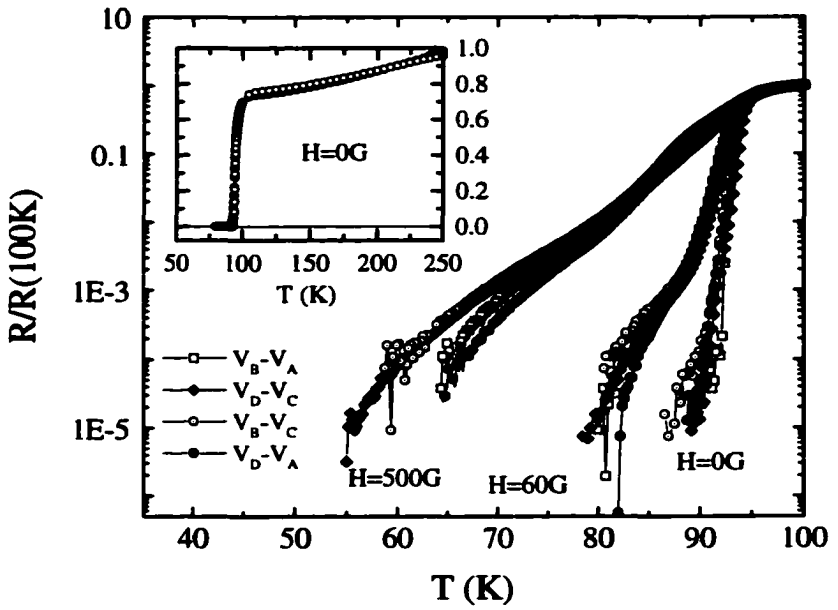

Figure 27. Main panel: Normalized electrical resistance versus temperature for different magnetic fields. The measurements were performed using many equivalent pairs of contacts as described in the text. Inset: Zero field temperature dependence up to room temperature of the resistance measured along the two radii of the disk.

In addition to the data from the same contact pairs as the inset, the figure also shows measurements for the crossed pairs, (V_B, V_C) and (V_A, V_D). If the radial voltage pairs give us information about the properties of a small crystal region around the probed radius, the crossed pairs provide us with data that reflect the properties of the material situated between the two radii. This is a thorough test of the sample homogeneity. As one can see from Figure 27, the electrical resistance measured at all contact pairs follows a similar temperature dependence, indicating homogeneous current flow and material properties. A difference between the measured

resistances becomes appreciable only at very low dissipation levels. These differences are likely to be due to local variations of the pinning properties within the large crystals that were used. All my Corbino samples show similar results when tested for quality, which indicates that the samples have an isotropic radial current distribution.

4.4 Experimental results and interpretation

Shown in Figure 28 is a comparison between the normalized electrical resistance versus temperature obtained in the Corbino disk and standard bar geometry experiments performed in the same, but cut, crystal as described in section 4.3.

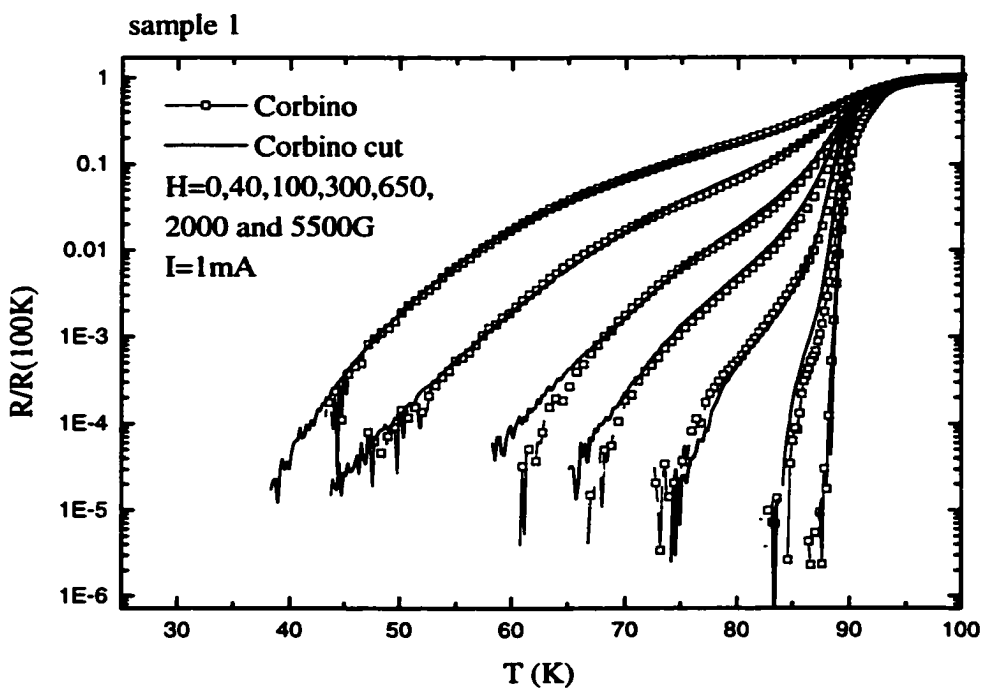

Figure 28. Comparison of the normalized electrical resistance versus temperature for a Corbino disk and a rectangular sample at various applied magnetic fields.

The resistance data are normalized to their values at 100K to account for the different current densities. It can be seen that, for all measured magnetic fields, the electrical resistances in the vortex liquid state are practically indistinguishable. I have obtained similar results for all the Corbino samples, for which I present examples in Figure 29.

In addition to the electrical resistance, other physical parameters can be compared. Early transport experiments on BSCCO 2212 single crystal found that the resistivity in the vortex liquid state is described by a thermally activated temperature dependence of the form (61):

$$\rho(T) = \rho_0 \exp[-U_0(H)/kT] . \qquad (4.3)$$

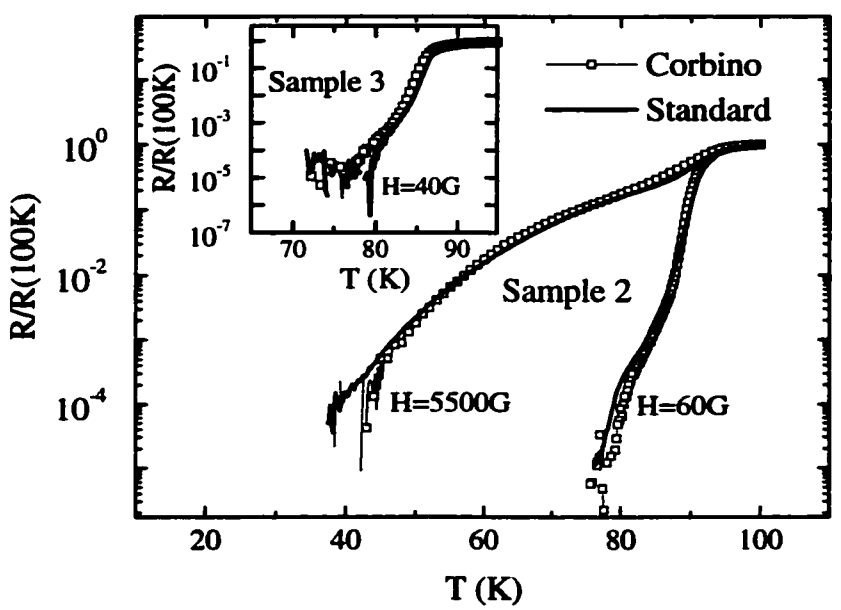

Figure 29. Main panel and inset: Comparison of the normalized electrical resistance versus temperature from additional similar experiments to those illustrated in figure 28.

U_0 is called the activation energy and was estimated to be about 700K for an applied magnetic field of 0.5T. Within a single-particle scenario, the thermally activated behavior of the electrical resistivity is understood as originating from the vortex hopping between pinning centers in the bulk of the superconductor. Therefore, this is a model that disregards the surface effects and assumes that the vortex motion is controlled by bulk properties. I can compare the activation energies of the disk sample and the rectangular one. If they are similar, than the surfaces do not influence the vortex motion. However, if the two activation energies are very different, the comparison makes no longer sense and the contribution from the surface barriers cannot be neglected.

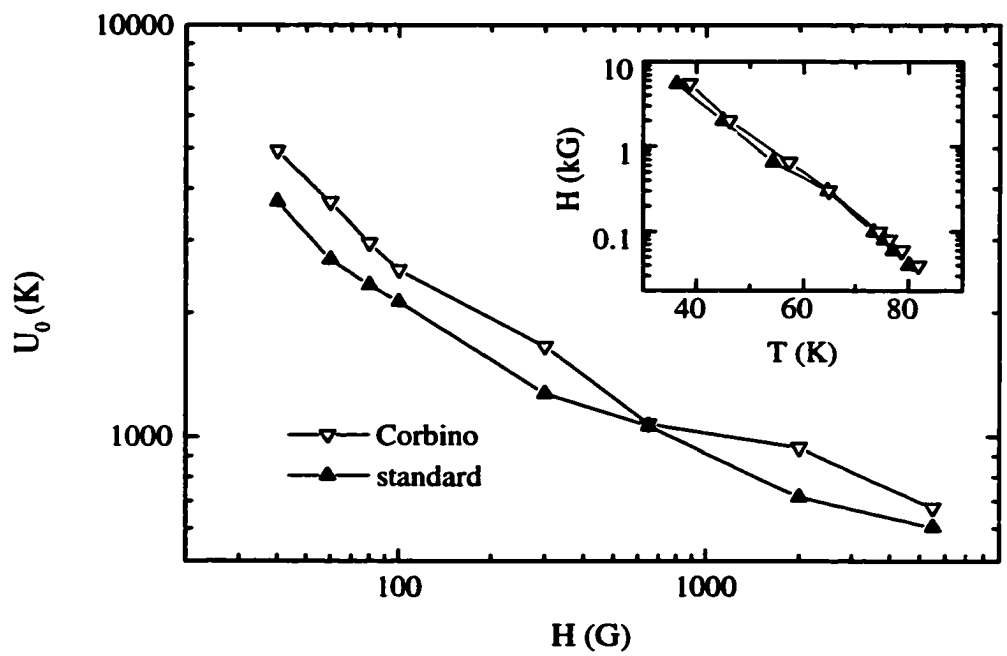

Figure 30. Main panel: Magnetic field dependence of the activation energy U_0 for a disk and a bar-shaped sample. Inset: Zero-resistance lines for the Corbino disk and rectangular samples.

Seen that U_0 is determined from raw resistivity data, which show no appreciable difference between the normalized resistances of the Corbino sample and the standard bar, we expect also that the activation energies corresponding to the two configurations to have a similar trend. Indeed, after plotting together the estimates of U_0 obtained from the two sets of data measured before and after the cutting of the Corbino disk sample, we see that the two activation energy curves are very close one to the other (Figure 30).

In the inset of Figure 30, we present the irreversibility line, defined when the measured electrical resistance drops below 10^{-4} of its value at 100K. These lines are practically identical for both types of samples, which indicates that the same mechanism is governing the flux pinning in the different geometries.

In conclusion, the experiments indicate that the electrical transport properties for our particular BSCCO 2212 samples are not significantly affected by surface effects. Since we know that the surface effect is real, the only explanation is that the edge pinning is very weak in comparison with the bulk pinning so that it is not observed in the temperature and field regimes used in the measurements. On the other hand, soon after the publication of these results (26), a similar experiment was reported by Rycroft and coauthors, in which differences between the transport properties of a Corbino disk and a four-probe configuration were seen (46). This would imply that the surface barrier effects are not negligible. However, I have to make a comment that the crystals used in reference 46 came from a different source. Therefore, their intrinsic properties will be different. In particular, a comparison of the upper critical points of one of our samples with and the crystal from reference 46 reveals that our crystal has a lower H_{cr}, thus a greater concentration of point defects. Although the number of defects is not large enough to completely destroy the first order melting, they could provide a much larger pinning than the edge. In this reasoning, a very clean sample would clearly show the surface effect in its transport properties

when measured using a four-probe configuration, while a dirty crystal would be dominated by the bulk behavior.

5. TRANSPORT PROPERTIES OF IRRADIATED HIGH-TC SUPERCONDUCTORS

5.1 Introduction

The purpose of this chapter is to give an overview of the background information on the effect of the columnar defects created by heavy-ion irradiation on the transport properties of high-temperature superconductors. This information will be needed in chapter 7, when two BSCCO Corbino samples will be irradiated with high energy ions.

The presence of disorder in the crystalline structure of cuprates, in general, drastically affects the vortex motion both in the liquid and solid states. The nature of the vortex melting transition and implicitly the phase diagram are also altered by the defects. In clean samples, the transition from the vortex lattice to the vortex liquid was shown to be of first order (10,12,13,62). The introduction of disorder into the system seems to suppress the first order phase transition (63) since the vortices can no longer form a regular lattice. Depending on the type of disorder, various glassy vortex states have been suggested for the vortex solid phase (64-68), in particular Bose glass for the systems containing columnar defects.

There are many fundamental and practical advantages and applications of the controlled introduction of columnar tracks into the structure of the high temperature superconductors. Phase transitions are an area of fundamental interest in solid-state physics. The irreversibility line is shifted towards higher temperatures - a feature that can be very useful for superconducting devices that are designed to work at high temperatures (24). Another consequence of heavy ion irradiation is that the critical current is enhanced considerably (17). A direct application of this would be the manufacture of superconducting wires that can support a high current. However, in this chapter I will simply describe the effect of the crystal irradiation on the freezing temperature of the vortex liquid in YBCO due to the created pinning centers. The beneficiary is the experiment presented in chapter 7, in which a BSCCO Corbino sample will be selectively

irradiated in order to create a pattern necessary to the study of vortex shear. Although the two materials (YBCO and BSCCO) are slightly different, the effects of the columnar defects on the vortex dynamics are similar. Therefore, I can use the conclusions of the present chapter in support of the data discussed in chapter 7 of this work.

5.2 Experiment description

The experiment consists of irradiating, with different densities of columnar defects, a series of YBCO crystals with similar initial characteristics and studying the change in their electrical properties. The density of defects is usually defined by the equivalent dose matching field B_Φ necessary to produce the same vortex line density as the tracks, i.e. $n_{defects}=N_{defects}/A_{sample}=B_\Phi/\Phi_o$. Single crystals of YBCO were prepared using the flux growth method described in chapter 2. I chose a good quality crystal of considerable dimensions, 1050μm×795μm×85μm and after annealing, detwinning and polishing, it was cut it in five similar slab-like pieces with the approximate dimensions 200μm×795μm×20μm. Note that the last dimension, which corresponds to the thickness, is now 20μm. The sample was thinned down by polishing in order to make sure that all heavy ions would pass through the crystal during the irradiation, producing straight tracks in the crystalline structure as explained in chapter 2.

For a systematic study that aims to individualize the effect of columnar defects on the transport properties of YBCO, it is best to start with a clean, untwinned crystal to which columnar defects can be added. Twin boundaries can behave as correlated defects and introduce extra features in the transport properties due to phenomena like guided motion of the vortices parallel to a twin plane (69). Therefore, the information extracted from an experiment performed on a twinned irradiated sample would also contain a contribution due to the pinning from the twin planes present in the system. For an experiment designed only to monitor the general trend in the change in the electrical properties of HTSC with the dose of columnar defects, it is not critical to

have a clean crystal. In the following sections, I am going to show results in both twinned and untwinned YBCO samples. Note that irradiated BSCCO single crystals, which will be discussed in chapter 7, do not grow twinned. However, they could contain a large number of point defects, which also act as pinning centers.

Returning to the sample preparation, all five pieces resulting from the crystal cleaving are prepared into four-probe configurations by the method described in chapter 2. Four of these samples were irradiated with various doses of defects, while the fifth one was left untouched and kept as a reference crystal. Since all five samples belong to the same original crystal, we can assume that the underlying properties are identical, which is very important for the data analysis. If there were considerable initial differences between the crystals, then one could not be sure if the post-irradiation experimental results were due to the newly-introduced disorder or some inhomogeneities already present in the system. On the other hand, if all crystals have the same intrinsic properties to start with, then the resulting change in electrical properties will only be associated with the additional disorder introduced by the different doses of columnar defects.

The irradiation took place at Michigan State University, National Superconducting Cyclotron Laboratory and used a beam of Au^{62+} ions with the energy of 2 GeV. The direction of the columnar defects was chosen to be parallel to the c-axis of the crystal since all transport measurements are performed applying the magnetic field perpendicular to the ab-plane. As already stated in chapter 2, it is expected that the columnar tracks are most effective pinning centers when aligned with the direction of the flux lines. The defects are straight cylindrical tracks with an amorphous core of approximately 4 to 10nm in diameter (70). The defect size is comparable to that of the vortex core, which ensures that the columnar tracks are highly suitable as anisotropic pinning sites. The chosen dose matching fields were 500G, 1000G, 1T, and 6T. One can clearly divide the doses into two categories: low and high densities of columnar defects.

It will become clear in the following section that the effects of the columnar defects on the transport properties of YBCO can be different depending on the size of the given dose.

5.3 Experimental results

In Figure 31, I present electrical resistance versus temperature measured at different magnetic fields on the unirradiated reference sample yba304. For magnetic fields between 1 and 9T, the pre-irradiation data show a sharp 'kink' in the tail of the resistive transition associated with the first order vortex melting transition.

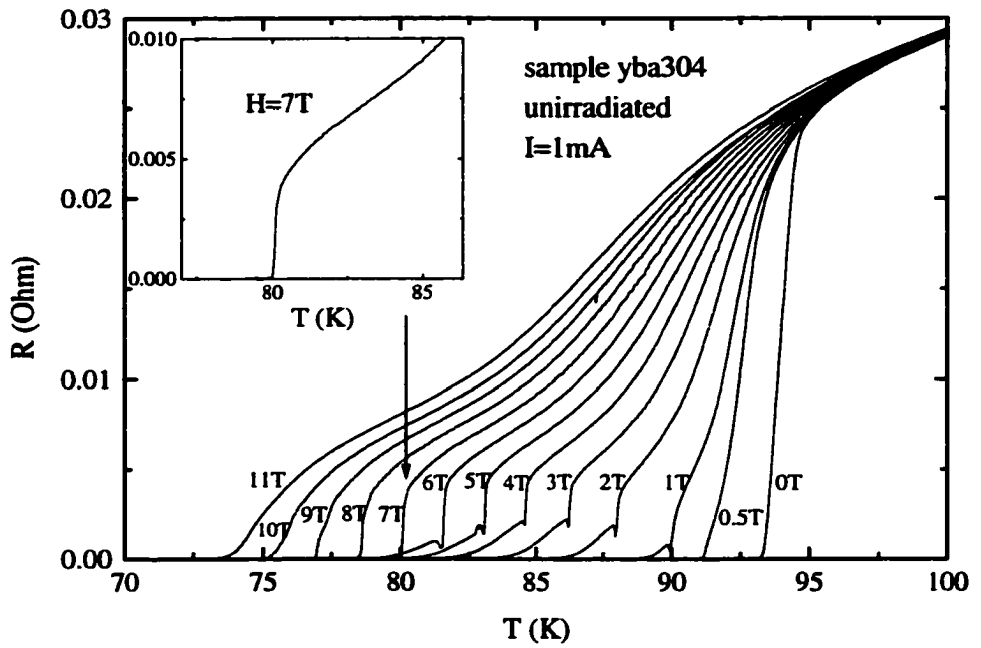

Figure 31. Electrical resistance versus temperatures of an untwinned YBCO single crystal at various magnetic fields. The arrow indicates the kink associated with the first order liquid-solid transition at 7T. The inset shows the tail of the resistive transition at 7T.

The arrow in Figure 31 indicates the sharp drop in the temperature dependence of the resistance taken at a constant field of 7T, which is shown enlarged in the inset of Figure 31. Below the transition temperature the measured resistance is zero, indicating that as soon as the vortices have solidified, they become pinned as a whole by the point defects present in the crystal. As a consequence, the Lorentz force is unable to move the vortices and the total dissipation is zero.

According to thermodynamics, for a first order phase transition of a magnetic system to occur, there must be a discontinuity in the first partial derivative of the free energy, the magnetization. Therefore, thermodynamic evidence of a first order phase transition in YBCO was obtained in magnetization measurements (12,13). A direct correlation between the kink in the resistivity and the thermodynamic first order vortex melting transition was established afterwards by a simultaneous measurement of the resistivity and magnetization on an untwinned YBCO crystal; this confirmed that the jump in the magnetization coincided with the onset of the kink in the resistivity (56). There have been also calorimetric measurements (14) and torque-magnetometry experiments (71), all of these providing evidence for a first order transition from a vortex liquid state to a solid lattice phase. For magnetic fields smaller than 1T and larger than 9T, a jump is no longer detected. Instead, the resistive drop becomes gradual. I have already defined the upper critical point in the previous chapter as the magnetic field above which the first order transition disappears, which for the sample from Figure 31 would appear to be slightly greater than 9T. Correspondingly, I will define here a lower critical point as the magnetic field below which the jump in the resistive tail is not observed. In our case, the lower critical point seems to be somewhere between 0.5 and 1T.

Finally, the last distinctive features, which are noticeable in Figure 31, are the long tails that appear in the temperature dependencies of the electrical resistance immediately below the kinks. This feature has been called the peak effect (72). Note that it appears only for a reduced magnetic field range between 1 and 6T. The peak effect was explained by a softening of the

vortex lattice followed by a rearranging of the vortex positions with respect to the pinning centers locations in order to minimize the total energy of the system. This is the reason why the electrical resistance does not fall to zero, like in the inset of Figure 31. Instead, the long tail is observed. The peak effect is the result of the competition between the elastic energy of the vortex lattice and the pinning potential of the columnar defects.

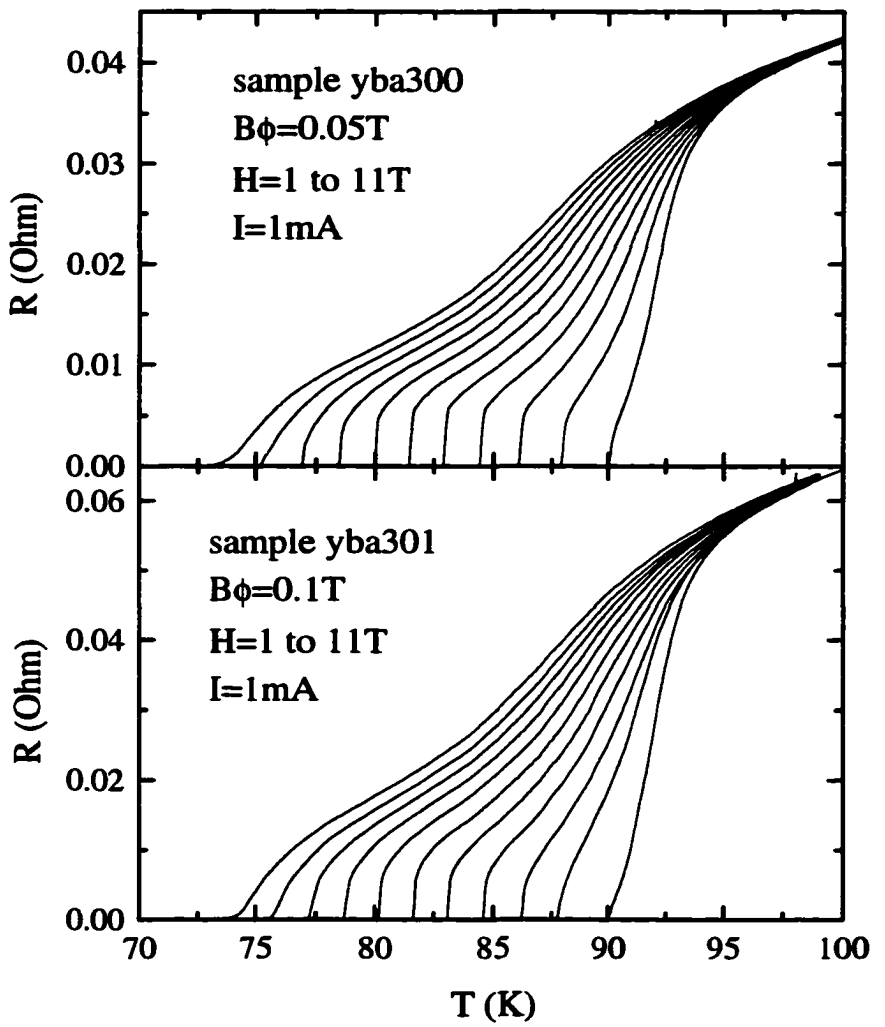

Figure 32. Temperature dependence of the ac resistance for magnetic fields between 1 and 11T of sample yba300 irradiated with a dose matching field of 500G.

In Figure 32, I show the resistive transitions for magnetic fields ranging from 1 to 11T (with an interval of 1T) for the samples irradiated with the smallest doses of columnar defects, B_Φ=0.05T (upper panel) and 0.1T (lower panel). As one can see, the samples still exhibit first order melting. However, the peak effect has disappeared, implying that the quantity of defects that were introduced through irradiation are capable of better pinning the vortex lattice at all temperatures below the transition for an applied current of 1mA.

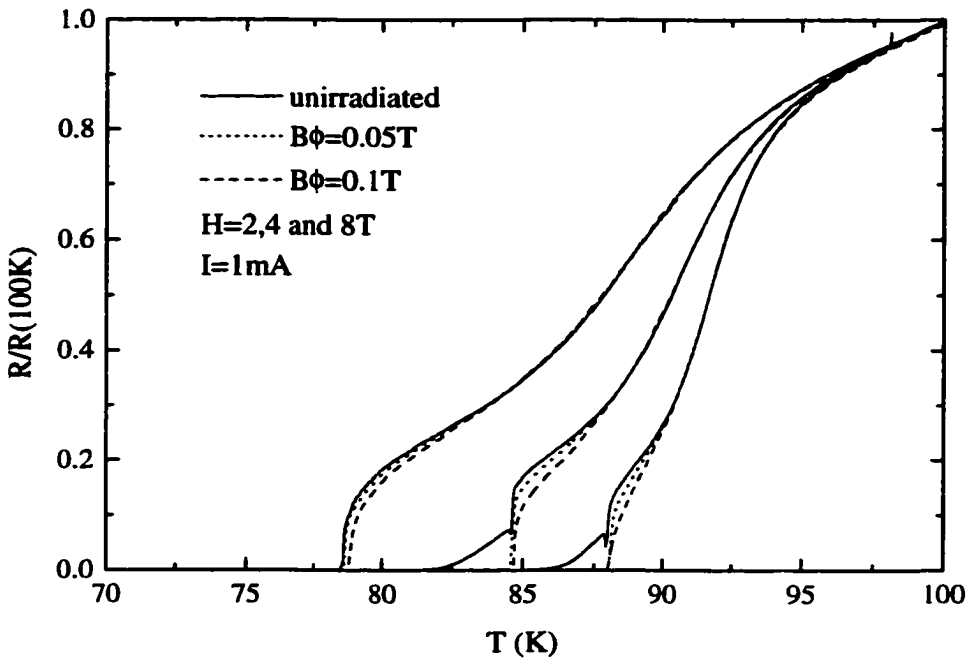

Figure 33. Comparison of the electrical resistance in the vortex liquid phase for the unirradiated and the low dose samples for various magnetic fields.

Thus, the peak effect will also not be present for the samples irradiated with higher doses.

At the first glance, there is no obvious difference between the data for 500G-dose and the 1000G-dose samples. A more careful comparison (Figure 33) reveals that the resistivity in the

vortex liquid state has diminished due to pinning from the added columnar tracks. The position of both the upper and lower critical points is also affected by the introduction of the columnar defects in the system (73). The authors in reference 19 have found that both critical points are shifted towards higher magnetic fields. In my samples, I do not see a change in the position of the upper critical point, but the lower critical point has increased for the sample with B_Φ=0.1T.

One can also show how the pinning increased by performing magnetization measurements. In such an experiment the crystal is cooled down to the temperature of interest, the magnetic field is gradually swept up and then down and all this time the magnetic moment of the sample is measured through any of the following methods: SQUID magnetometry, Hall probe magnetometry, etc. A high-temperature superconductor has a negative magnetization while in the mixed state due to the fact that the magnetic field is expelled from some regions of the sample.

If the crystal has defects that pin the vortices, the magnetization will acquire an irreversible characteristic (the magnetization of the sample when the field is increased will be different from the one when the field is decreased). As a consequence, such a magnetization measurement will look like a loop after a complete sweep of the magnetic field. According to Bean's model, the width of the magnetization loop is proportional to the pinning strength of the defects present in the crystal.

I have setup the measurement system for taking a magnetization loop using the Hall probe magnetometry technique. I have performed magnetization measurements on a YBCO single crystal not involved in the transport experiment described in this chapter. In Figure 34, I am showing a comparison of magnetization loops taken before (upper panel) and after (lower panel) the irradiation of this crystal with a dose matching field of 1500G, a value close to the low doses studied in the transport experiment (500and 1000G in samples yba300 and 301). I have maintained the same scale on the upper and lower plots in order to make the comparison easier. As one can see, as a consequence of the irradiation, the width of the magnetization loops has

increased - therefore, the pinning has increased - although not by much since this crystal has only a low density of columnar defects. Similar measurements obtained for crystals irradiated with higher densities of defects show an even larger enhancement of the pinning (74).

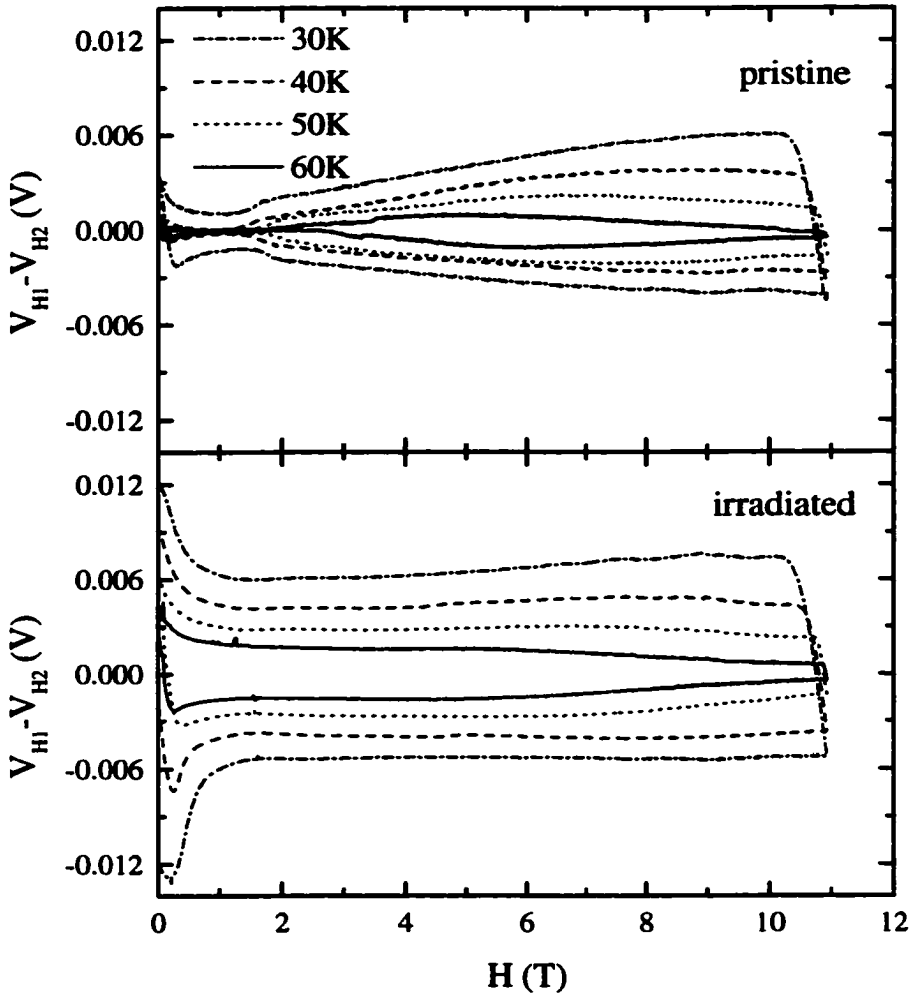

Figure 34. Magnetization loops on a untwinned YBCO single crystal before (upper panel) and after (lower panel) the irradiation with B_Φ=1500G.

Returning to the transport experiment, after the irradiation with B_Φ=1 and 6T, the kink has been replaced by a smooth monotonic decrease in the electrical resistance, indicating that the first order melting has been completely suppressed by the irradiation and transformed into a transition of second order or higher (Figures 35 and 36). The vortices cannot form a lattice anymore, since they are pinned by the columnar defects that are randomly distributed throughout the sample, thus determining a disordered solid phase. This indicates that the pinning from the columnar defects is very effective and stronger than the vortex-vortex interaction. The resistance curves also shrink closer together as the dose is increased. At the highest dose, the slopes of the resistivity curves taken at different fields are nearly parallel, as shown in Figure 36. Clearly, the freezing temperatures, or the temperatures when the dissipation vanishes, are much higher than for the unirradiated sample. This effect will be of importance in chapter 7, where the properties of irradiated BSCCO Corbino samples are discussed.

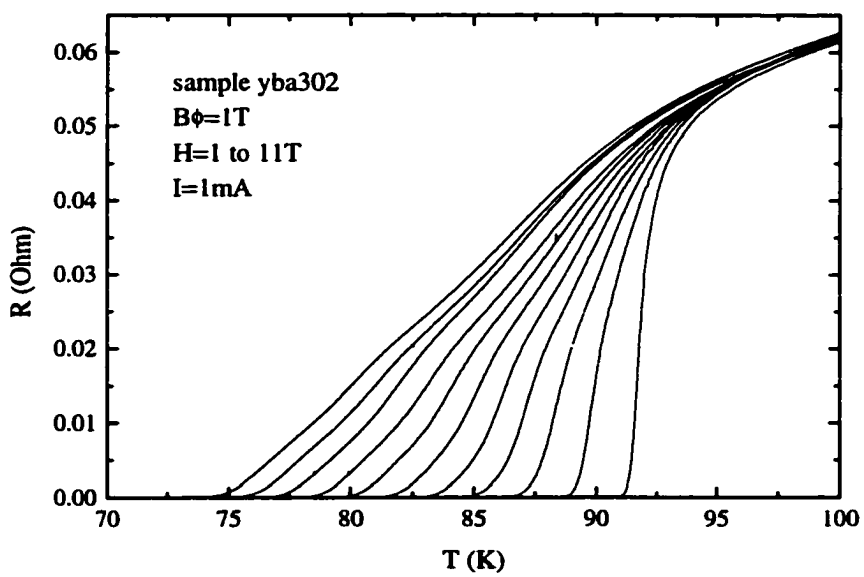

Figure 35. Temperature dependence of the electrical dependence for magnetic fields between 1 and 11T of sample yba302 irradiated with a dose matching field of 1T.

Other consequences of the defect introduction are: the zero field transition temperature, T_c, determined from the maximum in the temperature derivative of the resistivity, $d\rho/dT$, is shifted to lower temperatures, and both the width of the transition, ΔT_c, and the normal state resistivity, $\rho_n(100K)$, are increased. Before irradiation, the zero field transition temperature of the crystal was T_c=93.16K and as a result of irradiation it decreases down to 91.88K for B_Φ=6T. An increase in the normal state resistivity near T=100K of about 3.4% is observed between the unirradiated and the B_Φ=0.1T irradiated crystal. Moreover, the crystals irradiated with B_Φ=1T and 6T showed larger increases in the normal state resistivity, 20% and 27.5% respectively. This is attributed to the large damage inflicted upon the sample at these high doses.

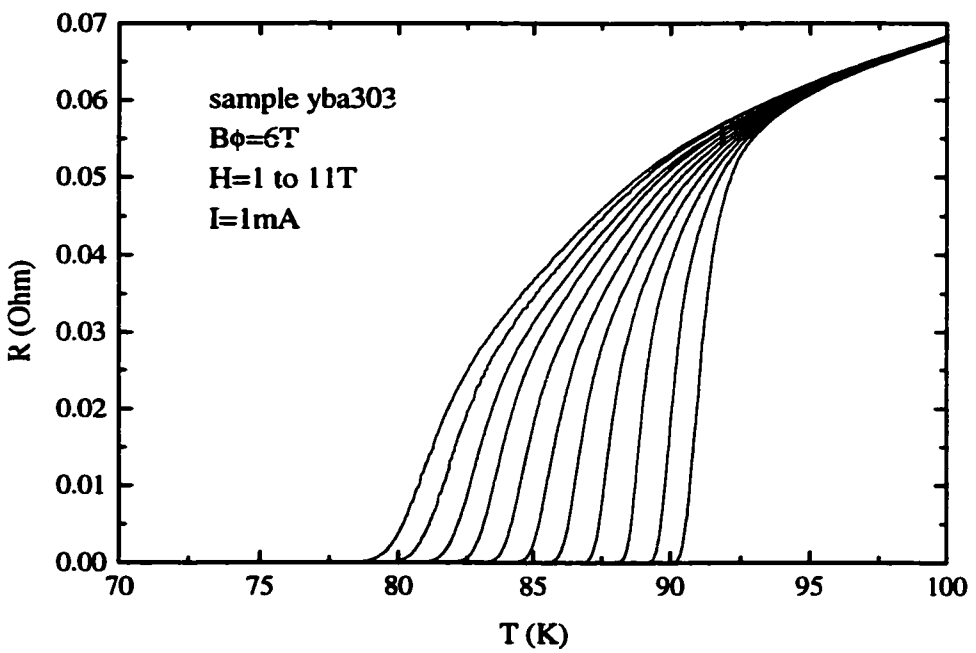

Figure 36. Electrical resistance versus temperatures of sample yba303 with B_Φ=6T at various magnetic fields between 1 and 11T.

For example, a dose of B_Φ=6T produces a columnar defect spacing of about 187Å. Since the columnar defect cores are about 100Å in diameter, this suggests that there is no separation between the perimeter of the columnar defects, implying a completely damaged sample. However, it is clear from the data presented in Figure 36 that the sample still has superconducting properties. This issue is not yet very well understood.

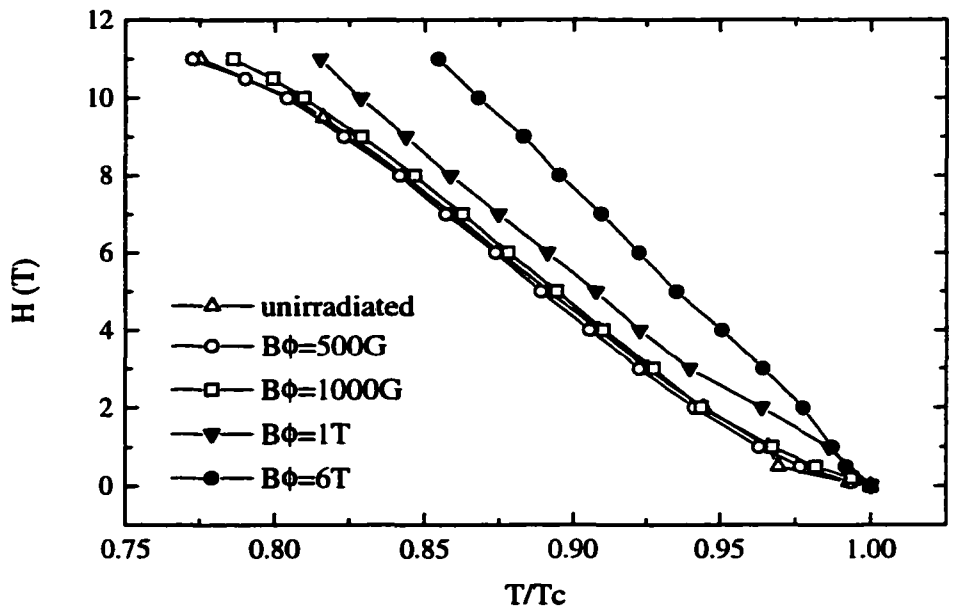

Figure 37. Melting lines (open symbols) for the unirradiated sample and the low dose crystals and irreversibility lines (full symbols) for the high dose samples. Each line has been plotted versus the normalized temperature T/Tc, where Tc is each crystal's critical temperature.

By tracing the field dependence of the zero resistance temperature ($10^{-5}\Omega$), the irreversibility lines can be mapped in the phase diagram for all studied YBCO samples. Figure 37 displays the irreversibility lines for samples yba302 and 303 together with the vortex lattice

melting lines for samples yba300, 301 and 304. Notice the distinct change in slope of the irreversibility line of sample yba302 at the matching field 1T, which is shown by the solid triangles in Figure 37. The irreversibility line displays a linear behavior above H=1T, following a faster variation with the temperature below 1T. This change in slope indicates a change in vortex pinning behavior.

For magnetic fields below B_Φ=1T, there are more columnar defects than vortices, so that each vortex can be pinned by a columnar defect. For this regime, the irreversibility line is characterized by a concave upward rise. However, for magnetic fields above B_Φ the number of vortices exceeds the number of defects, ensuring that the defects are not as efficient at pinning the vortices. Moreover, at higher vortex densities there are bundling effects that reduce even more the effective pinning. Consequently, the sharp rise in the irreversibility line is replaced by a linear behavior with a reduced slope.

Similar results were obtained by A. Mazilu and coauthors (27) in a series of twinned YBCO thick films irradiated with various high doses of columnar defects (Figure 38). As one can see, the irreversibility line is shifted towards higher temperatures as the dose increases. However, the shift seems to be greater than the one presented in Figure 37. I believe that the difference comes from the fact that the samples used in the two experiments are different, untwinned crystals versus twinned films. Also, the heavy ions used for the defect creation were different; gold for the crystals and uranium for the films, and it has been shown that the columnar tracks produced by uranium irradiation are the most effective pinners (Olsson R. J., submitted for publication). Nonetheless, the irreversibility lines of the irradiated twinned samples exhibit the same sharp upward rise observed for the untwinned crystals at temperatures close to Tc.

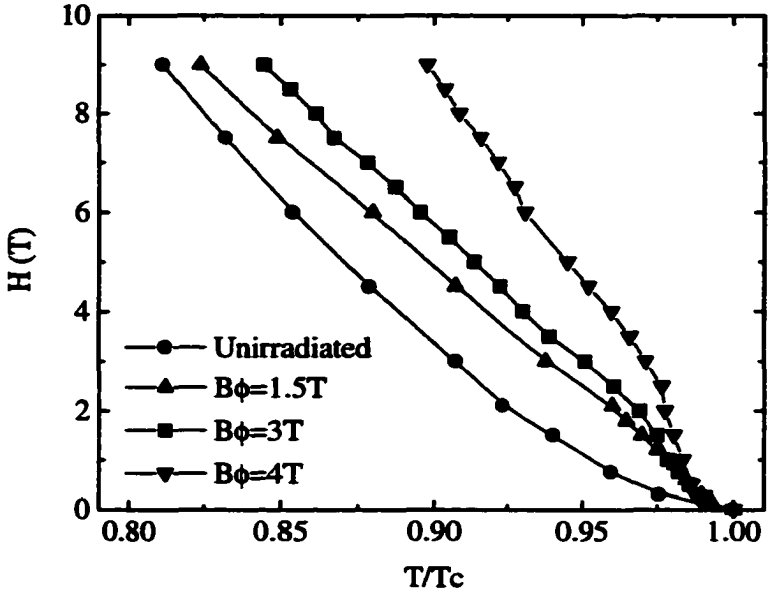

Figure 38. Irreversibility lines for the unirradiated and irradiated YBCO thick films.

The results indicate that the irradiation of crystals with a low dose creates only minor changes in the transport properties; that is, a slight reduction of the electrical resistivity in the vortex liquid state, without affecting the liquid to solid transition temperature. For the experiment in chapter 7, when parts of a BSCCO Corbino sample will be irradiated, a dose of 1T will be chosen to make sure that the vortices in the irradiated regions are strongly pinned and their irreversibility line has considerably shifted towards higher temperatures. In other words, a condition is required in which the vortices in the irradiated areas freeze at a temperature higher than the corresponding temperature in the pristine parts of the crystal. A dose matching field of 1T will have a much larger influence on the transport properties of BSCCO compared to YBCO since the former is very sensitive to disorder. Recall that the upper critical point of an as-grown BSCCO single crystal could reach only a few hundred gauss in a clean specimen, while in YBCO it can be hundred times larger. This shows that the electrical properties of BSCCO single crystals

in the mixed phase are strongly affected by even a small quantity of disorder. As has been demonstrated, a dose of 1T of columnar defects will enhance the freezing temperature of the vortex liquid in YBCO single crystals. Therefore, this is expected to be an appropriate value for the experiment in chapter 7. I should add that we used the same heavy ions with the same energy to irradiate the BSCCO Corbino samples.

6. TRANSVERSAL VORTEX CORRELATION IN UNIRRADIATED BSCCO CORBINO

6.1 Introduction

This chapter contains a study of correlated vortex motion in pristine BSCCO single crystals patterned as Corbino disks. Three single crystals of BSCCO 2212 coming from different batches were cleaved several times in order to achieve the thickness between 15 and 30μm and then prepared into circular geometries. Recall that in chapter 4, I applied only one pair of voltage contacts along one radius of the disk, which was enough to serve the purpose of measuring the bulk properties of the superconducting material. In the present chapter, at least two pairs along the disk radius are required since we are interested in measuring the transport properties from different regions and comparing them. Here, I am going to exploit the second property of the Corbino geometry described in chapter 3, the fact that the current density is nonuniform. The typical sample used in our electrical transport experiments looks like the one depicted in Figure 39.

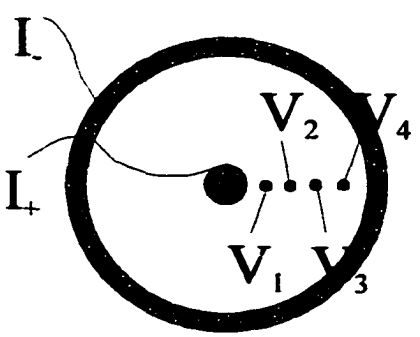

Figure 39. Corbino disk geometry showing typical voltage contact notation used in the present chapter. The number of voltage probes on each of the used samples differ, depending of the size of the crystal.

6.2 Experimental results

I performed electrical transport measurements on three Corbino samples with multiple radial voltage contacts: Kado4, Corbi1 and Corbi2. More precisely, the ac resistivity of all contact pairs, usually two at a time, at different magnetic fields and with different currents were measured while the sample was cooling down. Figure 40 shows typical temperature dependence of the signal collected from one of the voltage pairs of sample Kado4. For low fields, between 30G and 110G, one observes the abrupt jump associated with the first order transition; when the vortex liquid freezes and forms a lattice. The height of the jump decreases and vanishes at larger magnetic fields, where the transition is continuous. In this regime, the vortex liquid freezes gradually into a disordered solid through a continuous transition of second order or higher.

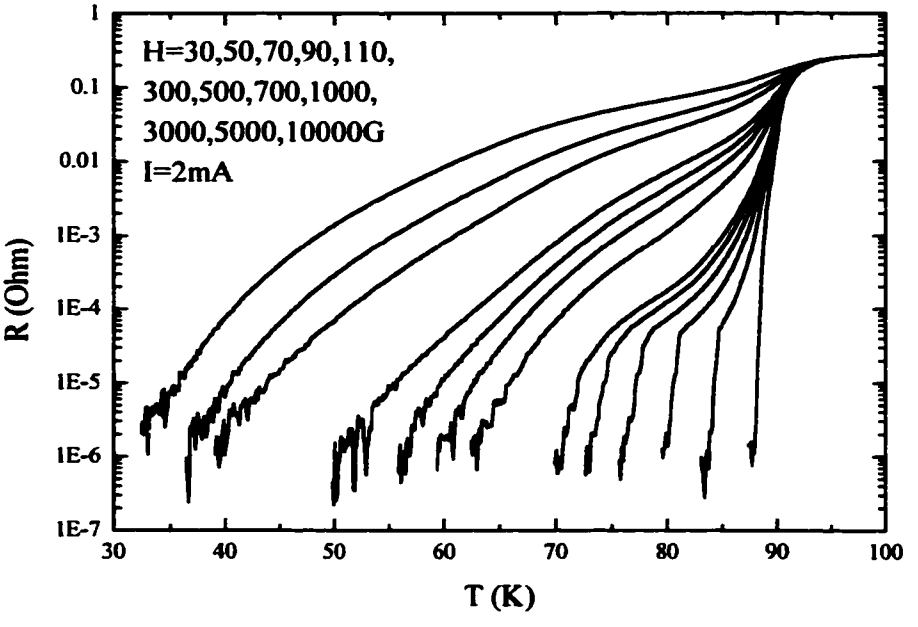

Figure 40. Electrical resistance versus temperature at various magnetic fields measured on sample Kado4. Low field data exhibit a first order transition from the vortex liquid state to a flux line lattice.

Comparing this crystal with the ones used in the experiments presented in chapter 4, one can say that the quality of Kado4 is superior to the ones of the BSCCO samples from the surface barrier study. The upper critical point of Kado4 is around 130G, higher than the ones of the crystals from chapter 4, which had an upper critical point of approximately 60G. This fact implies that the single crystal from which Kado4 is made is clean, containing only few structural defects. Samples Corbi1 and Corbi2 are also very good quality crystals, their transport properties being similar to the ones of Kado4. However, a slight difference between Kado4 and the other two Corbino samples is expected, because they were grown by different experimental groups.

Due to the fact that the current density is nonuniform in the ab-plane, the Corbino geometry is the only kind of geometry that allows the observation of transverse vortex correlation. Here, transverse implies the direction perpendicular to the vortices, therefore the correlation direction is along the ab-plane. Initially, when analyzing the data, I was looking to see if the vortex liquid state in BSCCO samples exhibits the 1/r electrical field behavior described in chapter 3. This would have been a confirmation of the Lopez *et al.*(45) data, which show that the 1/r behavior is respected in the vortex liquid flow in YBCO Corbino samples. If there were no transversal correlations in the vortex liquid state, so that the vortices move as fast as dictated by the local Lorentz force, the signals collected from any radial pair would be given by expression (3.8). For an anisotropic material like BSCCO, the radial signals will no longer follow expression (3.8), as discussed in section 3.6. However, they will satisfy the hierarchy relation (3.9), $V_{12}>V_{23}>V_{34}$. As a consequence, the data measured from various radial pairs (n,n+1) can be scaled with the scaling factors being either $\ln(r_{n+1}/r_n)$ or some constants given by our simulation in section 3.6. If, for any reason, the vortex liquid exhibits transversal vortex correlations, then we expect to see deviations from the 1/r-behavior, with the size of the deviation depending on how strong the correlation is. The vortex dynamics will then be nonlocal, meaning that the motion of the vortices in one region of the sample will be affected by the motion of vortices located in a

different region. The transverse vortex correlation can be created by shear viscosity, for example. Until now, it was believed that the shear modulus is always zero in the vortex liquid state and only different from zero in the vortex solid, where it is associated with strong interactions between the vortices. However, deviations from the 1/r behavior in the liquid state in BSCCO Corbino samples are observed, the evidence for which I will present below.

In Figure 41, the ac signals from different radial pairs for each of the studied samples is compared. Plotted are the electrical resistance versus temperature curves measured on the two radial voltage pairs, V_{12} and V_{23}, of sample Kado4 at different applied magnetic fields.

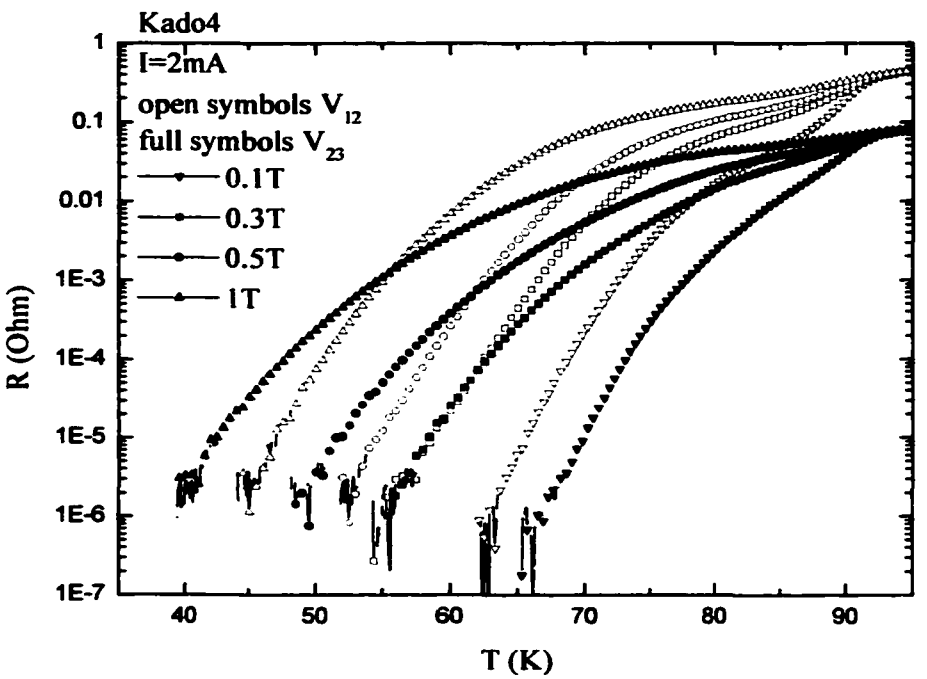

Figure 41. Temperature dependence of the electrical resistance of V_{12}, shown in open symbols and V_{23}, shown in full symbols. Data were taken simultaneously for the two radial pairs using a current of 2mA. Each symbol shape corresponds to a different applied magnetic field.

In Figures 42 and 43, I show the temperature dependencies of the outermost radial pairs of samples Corbi1 and Corbi2. This is the central result of the chapter. While at low fields the order relation (3.9) is respected, one notices that at high fields the voltage from the pair located closest to the outer frame of the Corbino disk becomes larger than the signal from the pair adjacent to it as the temperature is reduced. More explicitly, for sample Kado4 we have $V_{23}>V_{12}$, for Corbi1 $V_{34}>V_{23}$, and for Corbi2 $V_{56}>V_{45}$; the numbering of the voltage probes starting at the center of the disk.

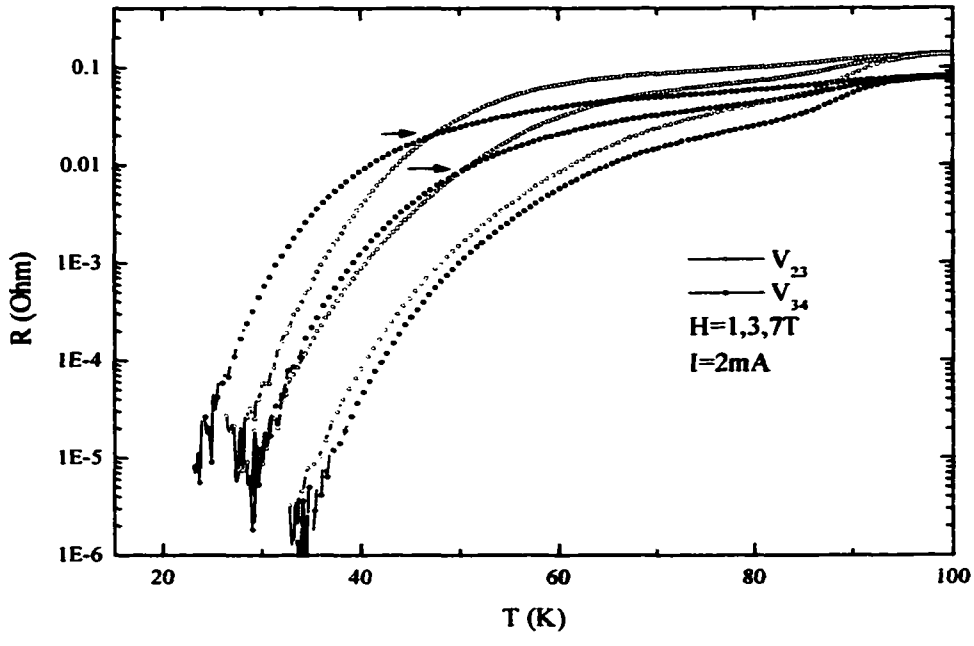

Figure 42. Electrical resistance versus temperature versus temperature for the two outermost radial contact pairs of sample Corbi1 at three different magnetic fields. The arrows indicate the crossing between V_{23} and V_{34} signals, which is an indication of transverse vortex viscosity.

The fact that the order relation is not respected anymore is the first indication that the vortex liquid does not exhibit the 1/r behavior. Obviously, these data cannot be scaled anymore; the

crossing between any two pairs of contacts making it impossible. Now, since the Lorentz force is very small close to the outer frame, one would expect the vortex velocity to be very small in this region. Instead, the experiment shows that there is a temperature range for which the outer ring of vortices rotates faster than they are supposed to move, as if they were dragged by the adjacent vortices that move with a larger velocity. Thus, the experiment provides evidence for the dynamic transverse vortex correlation.

I wish to point out that this effect seems to be dependent of the material properties and of the size of the geometry. For example, sample Kado4 exhibits vortex correlation at much lower fields than sample Corbi1. Recall that the sources of these two BSCCO crystals are different.

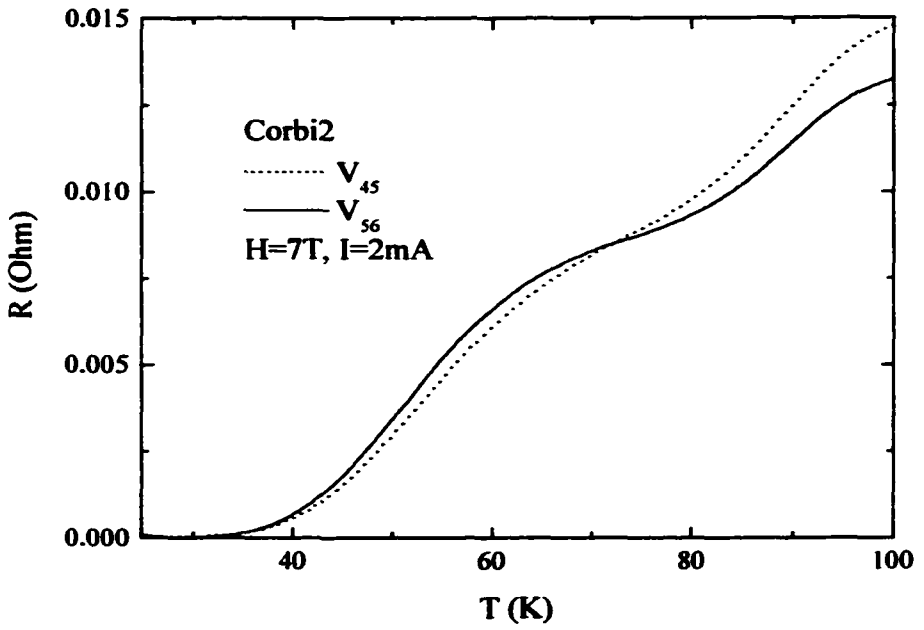

Figure 43. Temperature dependence of the outermost voltage pairs of sample Corbi2 taken at an external field of 7T. The displayed effect is much weaker than the one presented in figures 3 and 4.

Also, the sample size explains the difference between Corbi1 and Corbi2. Sample Corbi2 is larger than sample Corbi1 and, although it has similar intrinsic properties with the latter, it displays a weaker deviation from the 1/r behavior than Corbi1. Moreover, there are no reports in the literature about transverse vortex correlation in YBCO Corbino disks. As we learned in chapter 5, YBCO is a superconducting material with a critical temperature very close to that of BSCCO when both materials are optimally doped. However, the properties of the vortex liquid state in YBCO are different than that in BSCCO. For example, the upper critical point is much higher in YBCO, usually around 8T, as opposed to a few hundred Gauss, which is typical for a very clean BSCCO single crystal.

Although all three samples show similar characteristics, from now on I will concentrate on sample Corbi1, since this sample has the most complete set of data. The data in Figure 42 were measured using an electrical current of 2mA. One could ask how the behavior of sample Corbi1 changes if the probing current is varied. Do we still see the effect of the transverse vortex correlation? To determine the answer the IV curves of all radial pairs were measured in the regime of temperatures and magnetic fields for which deviations from the 1/r behavior are expected. When taking an IV characteristics the temperature and external field are kept constant, while the dc probing current is applied in increasing steps and the voltage signal is measured by a nanovoltmeter. To avoid thermal drifting effects, the current is applied successively in both directions and the two potential difference readings are subtracted and averaged to provide the actual voltage signal. Using the already acquired temperature dependence of the resistance shown in Figure 42 as a guide, I chose to perform this measurement at H=7T for three different temperatures 44,47 and 50K. The obtained IV characteristics are presented in Figure 44. As one can see, at T=50K the voltage pairs exhibit the hierarchy dictated by the radial dependence of the Lorentz force, $V_{12}>V_{23}>V_{34}$, for all probing currents.

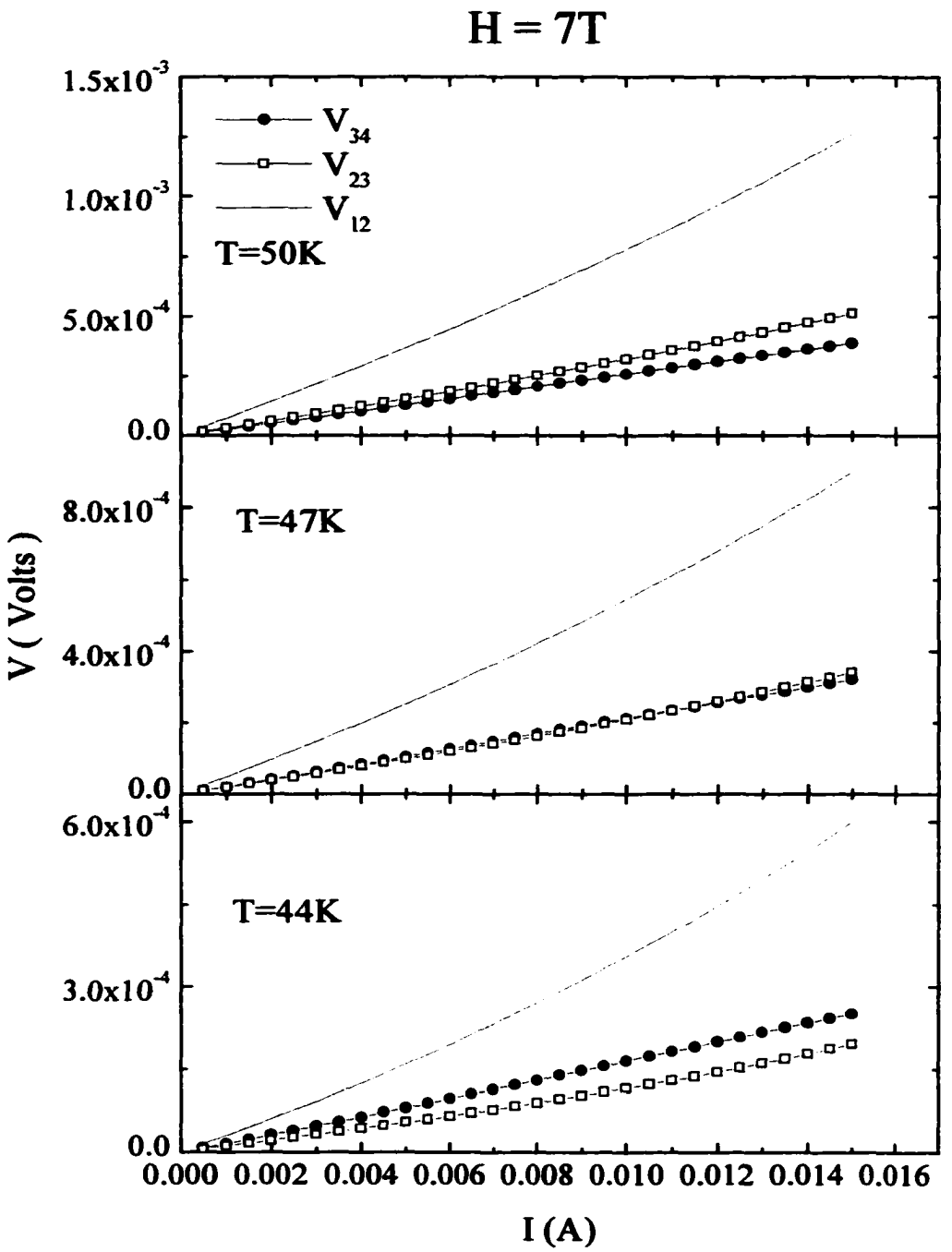

Figure 44. IV characteristics for all radial pairs of sample Corbil, V12, V23 and V34, taken at three temperatures, 44, 47 and 50K, at an applied magnetic field of 7T.

At a lower temperature, 47K, the signals measured on the two outermost contact pairs almost coincide, while at the lowest temperature, 44K, V_{34} becomes larger than V_{23} for any current up to 15mA. Therefore, one can conclude that the transverse vortex correlation can be observed in transport measurements for any applied electrical current.

In Figure 45, I show the normalized resistance versus temperature data for the same contact pairs on sample Corbil as in Figure 42. For each external magnetic field, one can clearly see the temperature where the deviation from 1/r occurs. Above this temperature, the normalized signals overlap, meaning the motion of the vortices is uncorrelated. Below the onset of deviation temperature, the scaling does not work anymore and one can clearly see the regime where the edge vortices move faster than they would under the Lorentz force.

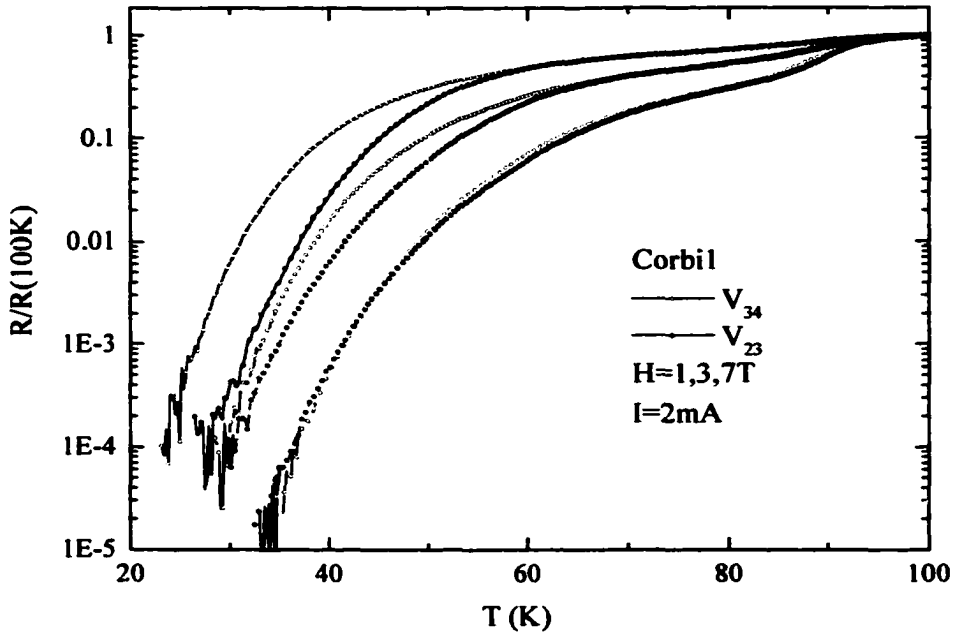

Figure 45. Normalized electrical resistance versus temperature of V_{23} and V_{34} in sample Corbil, same applied magnetic fields as figure 4.

Similar results were also obtained by Eltsev and coauthors (48) on a optimally doped BSCCO crystal patterned into a Corbino geometry. However, they did not observe the strong deviation evident in our experiment, in the sense that their outermost voltage never crossed any of the other radial signals. Eltsev *et al.* could only illustrate the deviation from uncorrelated flux motion when the data from the two radial voltage pairs was normalized and plotted together. A possible explanation of this could be that the authors of reference (48) used only low magnetic fields. In addition, we know that the effect is material and size dependent. After studying the graphs from reference (48), one can say that the single crystal used by Eltsev and coauthors has better quality than ours. Also, the size of their Corbino disk is larger than the dimension of any of our three samples. Thus, one would expect a smaller influence from vortex correlation since the data in this thesis suggests that the effect weakens for large samples.

Consistent in all data is that the innermost voltage pair V_{12} is always larger than any of the other two radial pairs, no matter the temperature, magnetic field and electrical current. One explanation would be that close to the center of the disk the Lorentz force is much stronger than the transversal drag due to the viscosity and therefore, the vortices in this region are not influenced by the viscosity. This is similar to what Lopez et al see in the vortex solid state in a YBCO Corbino sample. Due to the fact that the Lorentz force is very large close to the inner current contact, the lattice does not rotate as a whole and instead breaks in independent solid rings. Once the lattice broke, there is no interaction between the adjacent rings. In my experiment since it involves the vortex liquid phase, I cannot talk about solid rings, but I can still say that the vortex matter separates in two regions that do not interact with each other. There is a central region, which moves according to the local Lorentz force, and an outer region, in which the vortex dynamics is nonlocal and there is transverse vortex drag.

One other important feature that is observed in the data is a very weak nonlinearity of the electrical resistance. It becomes clear when the resistance versus temperature curves taken for

different values of the probing current at the same applied magnetic field are plotted together (see Figure 46). As one can se, at high temperatures all the curves overlap, implying that the response of the vortex liquid to the Lorentz force is local and linear. At low temperatures, there is a splitting between the various curves, in the sense that the resistance measured with high electrical current is larger than that taken with smaller currents. I said that this feature is weak since it is hardly observable in linear scale (Figure 46 is a semilogarithmic plot). The nonohmic behavior changes with the magnetic field as follows: at low fields the nonlinearity is very small, at 500G the splitting becomes more pronounced and at high fields it weakens again as shown in Figure 47. All Corbino samples display this nonohmic behavior, but one can see the nonlinear effects only in the contact pairs that are located closest to the center of the disk. All other radial pairs either exhibit a weaker nonohmic behavior or none at all.

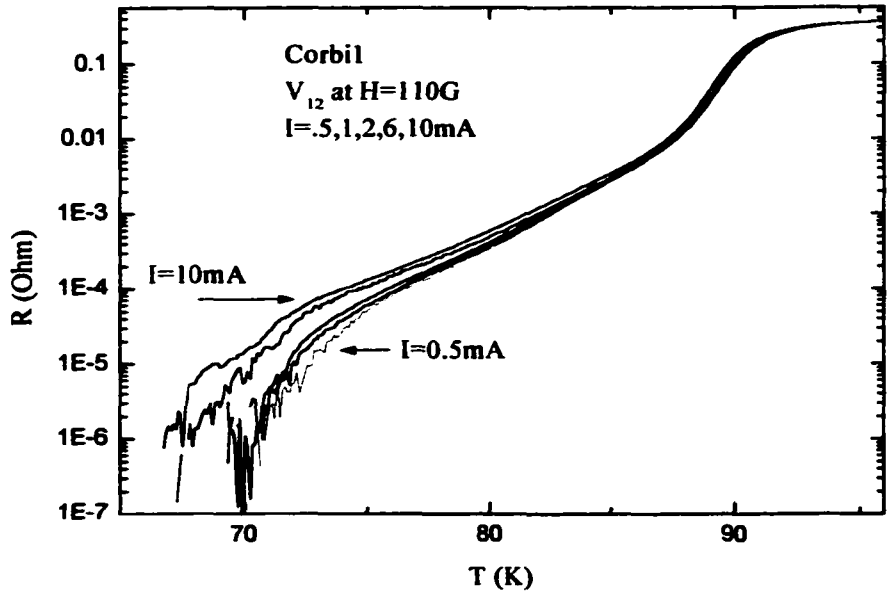

Figure 46. Temperature dependence of the electrical resistance taken with different probing currents at the innermost voltage pair, V_{12}, at a constant magnetic field of 110G. The arrows indicate the curves taken with the lowest and highest electrical current, respectively.

In fact, Kadowaki's group could not see any nonlinearity in a Corbino sample made out of a BSCCO single crystal (47). However they placed on their sample only one radial pair of voltage contacts. According to my study, it is possible that the position of their single contact pair was too far from the center of the disk to display the nonlinear effect: recall that in a Corbino geometry the current density is large in the central region of the disk.

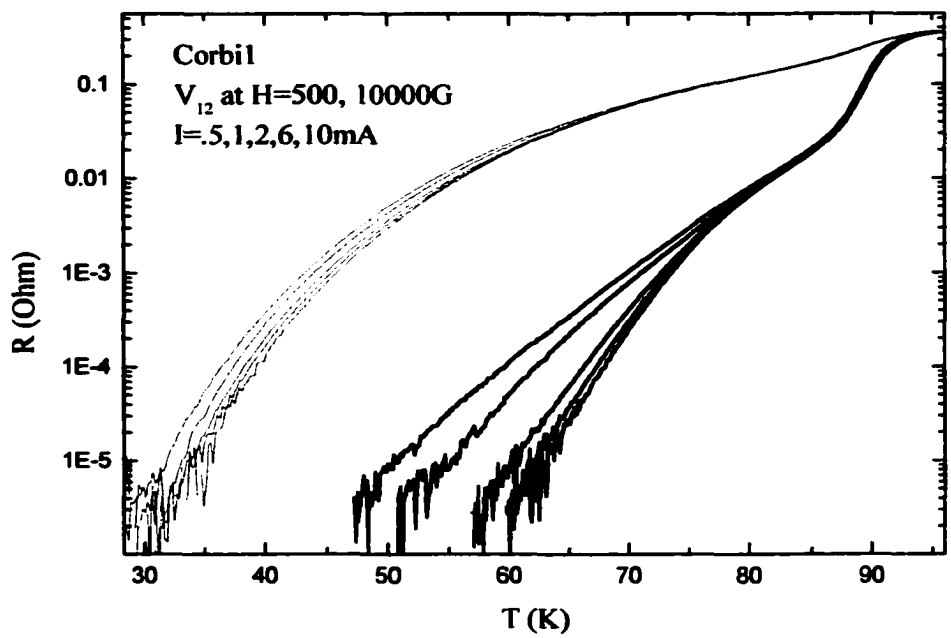

Figure 47. Electrical resistance versus temperature data of V_{12} of sample Corbi1. Each group of curves is taken at constant magnetic field using increasing probing currents from 0.5mA to 10mA.

At this time, there is no explanation as to why the nonlinear effects can only be observed in the regions with high current density. However, this fact does confirm that this feature is very weak and therefore needs a large driving factor to be triggered. Eltsev and coauthors also observed the nonlinear characteristic of the electrical resistance in their Corbino sample (48), and again in the

contact pair that is the closest to the center of the disk. It is believed by some that the behavior of the vortex liquid in BSCCO single crystals is actually linear and that the nonohmic behavior, seen in measurements on four-probe samples, is produced by the surface barriers. However, the data in this thesis show the nonlinear characteristic in a Corbino geometry, where the surfaces have no contribution to the transport properties, as discussed in chapter 3.

6.3 Discussion

I would like to attempt to explain the vortex correlation in the liquid state, presented in the previous section, using the concept of vortex shear viscosity. In the literature, this property is usually associated with a solid state or a state where the interactions between the components of the system are strong. In support of my case, I argue that at high magnetic field the vortices are very close to one another and therefore, as one can see from the following expression, the vortex-vortex interaction energy E_{12} is very large (75):

$$E_{12} \approx \frac{{\Phi_0}^2}{8\pi^2\lambda^2}\left(\ln\frac{\lambda}{r}+0.12\right) \tag{6.1}$$

for $\xi<<r<<\lambda$. In the above expression, r is the distance between the centers of the two vortices, ξ is the correlation length and λ is the London penetration length.

In their work, Eltsev et al. suggest that the vortex liquid state in BSCCO 2212 should be subdivided in two separate phases with different degrees of transverse vortex correlation (48). Let us plot on a H-T diagram the temperature and field ranges where I detect vortex correlation in my experiment. In Figure 48, the full squares represent the irreversibility line of V_{23}, obtained using a low resistivity criterion. The low resistivity criterion consists of determining the temperature at which the signal falls below a low value, which I chose to be $10^{-5}\Omega$. The irreversibility line, as it has been defined, gives information about the moment when vortices inside the disk stop moving

and a transition to a solid state occurs. Note that close to T_c in the irreversibility line, a few open square symbols are plotted. Those correspond to the melting line when the vortex liquid freezes into a solid through first order transition. The full circles represent the onset of nonohmic behavior for V_{12}, the only contact pair that displays electrical nonlinearity. For each magnetic field, I estimated the temperature where the splitting between the data taken with different currents is observed and call this the onset of nonohmic behavior. The full triangles in the center of the phase diagram mark the positions in the (H,T) space where the crossing between V_{23} and V_{34} occurs. Although the crossing is an excellent indication that there is a deviation from the 1/r behavior in the Corbil sample, it is not a very good approximation of the temperatures when the viscosity effect sets in. One can estimate these temperatures from Figure 45, where the normalized signals coming from V_{23} and V_{34} are plotted, so that the onset of the deviation is at the point where the two curves do not coincide anymore. In Figure 48, I represent the onset of transverse correlated vortex motion with the open triangles. It is interesting to note that the onset of deviation symbols form a continuation of the line representing the onset of nonohmic behavior. I do not know if there is a connection between these two effects. From the experimental data, it is observed that the nonlinearity is strongest for fields lower than 1T, where there is no sign of vortex correlation. On the other hand, the nonohmic behavior becomes very weak for $H \geq 1T$, but the vortex correlation sets in. Thus, one can state that for applied magnetic fields larger than 1T the vortex liquid can be subdivided into uncorrelated and correlated phases.

For this discussion, I would also like to remind the reader of the results presented in section 3.6. Due to the anisotropic nature of BSCCO 2212, the current distribution can alter the voltage signals collected from the radial contact pairs. More precisely, the voltage pairs located close to the inner or the outer current contacts of the Corbino sample could be larger than expected for a current uniformly distributed in the z direction. The main result of this chapter is also that the outer contact pair has a signal larger than what the 1/r law would dictate. Therefore,

it is possible that the effect in the data could be artificially created by the current distribution and is not really vortex correlation.

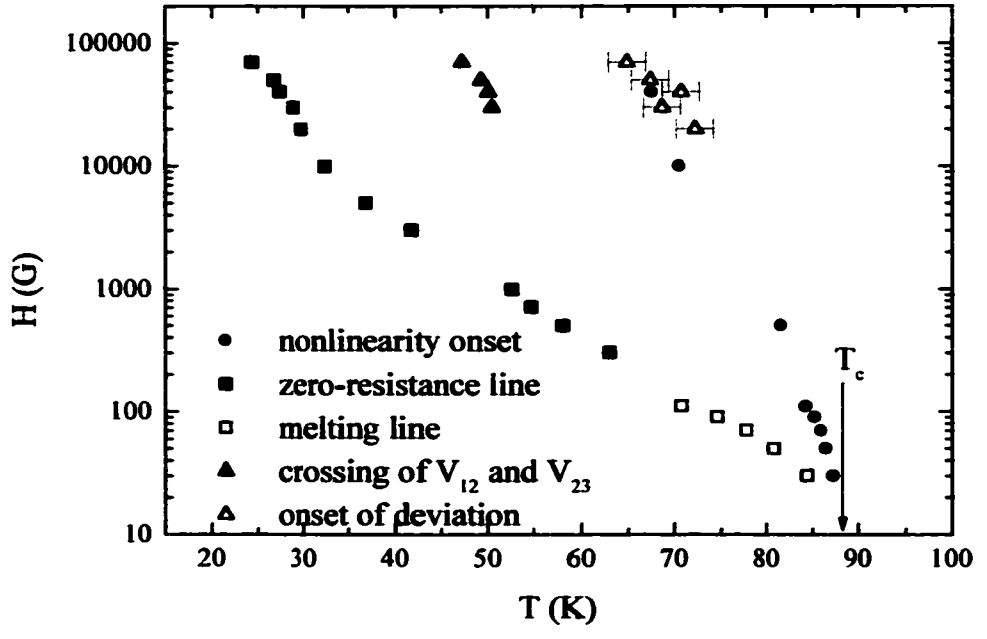

Figure 48. Phase diagram of sample Corbil containing the melting line, symbolized with squares, and the onset of nonlinearity line in full circles. Also mapped are the position of the crossing and the onset of deviation from 1/r-behavior.

However, the simulation of the radial dependence of the potential in section 3.6 showed that the peripheral region of the disk is hardly affected by the current redistribution: there is a little tail situated close to the edge of the disk (see Figure 19 in chapter 3), but it is very small and so it cannot be responsible for the observed effect. Besides, if the current distribution were responsible, another question would arise: why does the current distribution affects the size of the outermost voltage pair only for some magnetic fields and not for others? Shouldn't the current distribution be the same for any magnetic field? As a result, I believe that the data presented in

figures 41,42 and 43 are actually a consequence of vortex viscosity and not due to the current distribution.

Some theorists believe that the effect is due to a premature solidification of the outermost ring of vortices; so that what I actually see in the data is not vortex viscosity in the liquid state, but the rotation of a solid rigid ring of vortices. Now, the rotation motion of a solid ring of vortices could produce the crossing of the signals observed in the data. Moreover, at magnetic fields up to 500G the outer pair signal vanishes 10K above the temperature where the signal of the adjacent pair goes to zero. This could be an indication that the outermost vortices freeze early; but then, why isn't this solid ring of vortices rotating? Even if the ring has solidified, it should rotate no matter the size of the applied magnetic field since the current distribution is invariant. Furthermore, why would the outermost vortices freeze before the rest of the vortex matter? As one can see from the data for sample Corbil in Figure 48, at high magnetic fields there is a temperature difference of approximately 20K between the freezing temperature of the middle region of the sample (given by the irreversibility line) and the temperature of so-called freezing of the outer ring marked by the onset of deviation from 1/r behavior. I do not believe that the Lorentz force produced by a current of 2mA would be able to move a solid ring of vortices especially since the driving force is very small at the periphery of the disk, where this solid ring is located. Lopez et al., in his experiment conducted on a YBCO Corbino sample (45), was able to observe the rotation of the vortex lattice only for very large values of the current, 8mA or more.

Numerical values for the viscosity coefficient and correlation length cannot be extracted at this moment from the experimental data, because one would need at least three radial measured signals that show the effect in order to make a rough estimation of η from the equation of motion (3.11). In the present experiments, only two radial pairs seem to show the correlated motion. Moreover, there is the argument that in order to determine the viscosity correctly, one must solve the motion equation and then fit the measured data to the solution. However, the equation cannot

be solved unless the boundary conditions are specified. We do not know the boundary conditions for our pristine BSCCO Corbino samples. The task of adding boundaries to the samples and the estimation of the healing length will be completed in the following chapter.

7. TRANSVERSAL VORTEX VISCOSITY IN IRRADIATED BSCCO CORBINO SAMPLES

7.1 Introduction

The hydrodynamic vortex motion equation cannot be solved for an arbitrary sample geometry without having set boundary conditions. We do not know the exact boundary conditions for a pristine crystal patterned into a Corbino geometry. In principle, the Lorentz force for the vortices under the current contacts should be zero or very close to zero since the current is perpendicular to the current pads and the flux lines are also perpendicular to the plane of the contacts. Therefore, in the regions under the current contacts $J \times B = 0$, so that the Lorentz force is zero. As a consequence of the missing driving force, the vortices in these particular regions should not move. However, when electrical current is applied, we do know that the vortices immediately next to the boundaries will move under the influence of a nonzero Lorentz force. Now, this vortex flow could also set in motion the vortices at the boundaries through the vortex-vortex interaction. It is not yet known if this is true or not; therefore, we need to impose useful boundary conditions in some manner.

At the suggestion of Marchetti and Nelson (53), we can achieve this goal in the Corbino geometry by irradiating the boundary regions (the inner central dot and the outer circle) with high energy heavy ions. The columnar tracks produced inside the crystal by the ions constitute one of the most efficient vortex pin sites in high temperature superconductors (17). As a result, the vortices located in the boundary regions will not be able to move, thus providing us with a known boundary condition: zero vortex velocity. Experimentally, this can be achieved by covering the Corbino samples with special circular masks during irradiation. Using this method, I irradiated two BSCCO disc samples, Corbi1 and Corbi2 that were described in chapter 6.

The purpose of irradiating the boundaries is not only to create boundary conditions necessary for solving the equation of motion, but also to introduce a large scale inhomogeneity in the sample which is necessary to probe the viscous drag. The idea of introducing inhomogeneities has been already used in the past. In 1988, A Pruymboom *et al.* designed a thin film sample of Nb_3Ge with weak-pinning channels of nanometer scale separated by wide strong-pinning regions made of NbN to study flux-line shear through narrow constraints (76). In this work, the authors have probed the shear strength of the flux line lattice, while we are aiming to study the viscosity of the vortex liquid phase. In 1995, H. Pastoriza and P. H. Kes reported seeing shear viscosity of the vortex liquid phase of BSCCO 2212 in an experiment also involving a sample with weak and strong pinning channels (77). This time the strong pinning environment was created by irradiating the sample with high energy ions through an appropriate mask. The width of the weak pinning channels, where the vortices that exhibited viscosity move, was about 3μm, orders of magnitude larger than in the previous reference. In our Corbino disk samples, since the contacts are placed at least at 30μm apart, we are able to observe vortex viscosity on a scale of 30μm or larger. Neither of the above cited works determined the numerical value of the viscosity coefficient for the studied material. This was accomplished for the first time in 1996 by Theunissen et al.(78), who studied vortex liquid viscosity on Nb_3Ge/NbN samples with channels, similar to the ones used by A. Pruymboom *et al.*

I have explained the experimental results in chapter 6 using the concept of vortex viscosity. However, since a pristine crystal was used, I could not prove that the observed effect was indeed due to viscosity, simply because the data could not be matched to the theory due to the absence of appropriate boundary conditions. I believe that this purpose has been achieved in the present chapter. I should add that the post irradiation data shows a completely opposite trend than the unirradiated sample (chapter 6), simply because we introduced defects in the crystal structure. Nonetheless, the physics behind both sets of results is the same.

As stated above, the purpose of irradiating the boundary regions is to produce columnar defects, which will pin down the vortex lines, thus impeding their motion and resulting in a velocity equal to zero. However, this is not the case under all conditions. Usually, we investigate the temperature range from 100K, when the superconducting material is in the normal state, down to approximately 20K when there is no more dissipation and no detectable signal in the sample. At temperatures just bellow the regime of superconducting fluctuations, assuming there is an applied magnetic field, the vortex lines form a disordered state (called vortex liquid state) due to their high thermal energy. While in the liquid state, the flux lines cannot be pinned by any kind of defects, even if their shape and dimensions are favorable, because the thermal energy of the system is too large. As the temperature is reduced, the thermal energy becomes comparable to the pinning potential and the vortex lines begin to be pinned by the columnar defects. At the same time, the vortices become stiffer and they undergo a phase transition towards a solid state. The vortices then stop moving. When the number of vortices present in the system is less or equal to the number of columnar defects, one expects most of the flux lines to be pinned. This is the situation when the pinning is most efficient. Once we increase the applied magnetic field above the value of the dose matching field, some of the vortices will not be pinned and the overall pinning strength decreases. Here one could argue that even if only some of the vortices are pinned, it would still be difficult for the Lorentz force to make the vortices move since they form a solid state. This statement would be true if the solid were a regular lattice. However, BSCCO, the material that is used for this experiment, does not form a lattice, but a disordered solid state. Therefore, we expect that the strength of the boundary conditions to decrease for fields larger than the dose matching field.

We know from chapter 5 that the transition temperature for an irradiated superconducting crystal is higher than the melting temperature before the irradiation. If we denote with T_{BC} the transition temperature in the irradiated regions, which in our case are the boundary regions, and

with T_{zero} the freezing temperature inside the disk, then we will have $T_{BC}>T_{zero}$. Therefore, when taking an R vs T experimental curve, which is usually measured as the sample is cooling down, the vortices in the boundary regions freeze at T_{BC} before the vortices in the disk. Thus, the boundary conditions are only rigorously valid at temperatures between T_{zero} and T_{BC} (T_{BC} being different for each applied field), when the vortices inside the boundary region are frozen and pinned to the defects while vortices inside the disk are still in the liquid state and able to move. This regime is rather fortunate since we aim to study the vortex shear viscosity, a property that becomes observable at temperatures just above the vortex transition T_{zero}.

Both samples, Corbi1 and Corbi2, had the boundary regions irradiated, but only the latter was also hit inside the disk, in the region where the vortices move under the influence of the Lorentz force. I irradiated Corbi2 in a different manner for two reasons. One of them has to do with the study of the vortex viscosity in the Bose glass state and will be described in section 7.3. The second reason was to be able to measure an irradiated BSCCO crystal, since this will give an insight into what is going on inside the boundary regions, which obviously one cannot directly probe. In other words, by measuring the transport properties of Corbi2, one can extract information about the thermodynamic state of the boundary vortices at different temperatures and fields, which will be very useful for the data analysis of sample Corbi1.

Throughout chapter 7 we will use the notations Corbi1* and Corbi2* to denote the irradiated samples as opposed to Corbi1 and Corbi2 which remain associated with the unirradiated samples.

7.2 Irradiation experimental details

The irradiation took place at Michigan State University Superconducting Accelerator and used a beam of Au^{62+} ions with the energy of 2 GeV. The direction of the columnar defects was chosen to be parallel to the c-axis of the crystal since all transport measurements are performed

with an applied magnetic field perpendicular to the ab-plane. As stated, the Corbi1 and Corbi2 samples were irradiated at the inner and outer boundaries and the dose matching field was chosen to be 1T for both crystals. Afterwards, Corbi1* was removed from the target chamber while the Corbi2 sample received a second irradiation this time without mask. In the second part of the irradiation process, sample Corbi2 is irradiated everywhere with another dose of approximately 1T. This means that the boundary regions of sample Corbi2* have now accumulated a total of 2T-equivalent columnar tracks while the inside of the disk, where vortices move, has received only a 1T dose. Technical difficulties with the ion beam during the bombardment of Corbi2 makes us believe that the real dose was actually a bit smaller than 1T.

Figures 49 and 50 illustrate the irradiation procedure. The mask has a central orifice that is about the size of the inner current contact and an outer diameter corresponding to the inner diameter of the outer contact.

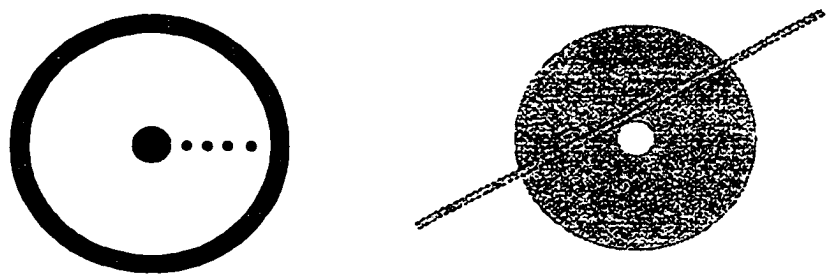

Figure 49. a) Crystal patterned into a Corbino geometry viewed from above; b) mask used for protecting the disk while irradiating the center and periphery of the sample

For clarity reasons, the gold wires that are attached to all contacts are omitted from the figure 49a. The mask was made of gold foil with the thickness of 100μm (Figure 49b), which ensures the total blocking of the beam. What is left uncovered by the mask, the current pads, will be of course

irradiated to produce the boundaries for our hydrodynamic flow problem, as shown in Figure 50. Since we had performed electrical measurements on these samples before we irradiated them, there were golden leads attached to the upper surfaces of the crystals. It is very important that these leads are not harmed during the process of irradiation, because any attempt to fix them afterwards will involve heating the sample, which will modify the oxygen content of the crystal. All superconducting properties of cuprates depend on the oxygen content, therefore by changing it one would create a different set of background properties in addition to the columnar defects. In such a case, a comparison between data taken before and after irradiation would not be trustworthy. It is also important that the mask is mounted as close as possible to the surface of the region of the crystal that is not supposed to be irradiated in order to avoid any shadowing effects. Therefore, I carefully flattened the golden leads until they touched the crystal and then applied the mask.

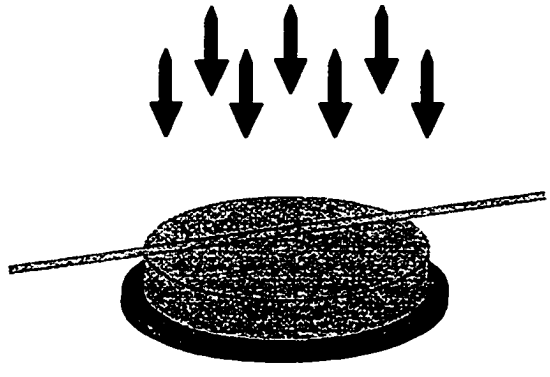

Figure 50. Corbino sample covered with mask setup for the irradiation. The arrows indicate the motion direction of the high energy ions.

I should also mention that the same mask was initially used for the gold evaporation of the current contacts, therefore we have a perfect match of the pads shape with the one of the mask. After the irradiation the mask is removed and the leads are brought back to the original upward position, without touching each other or the surface of the crystal.

7.3 Theoretical overview

In this section, I will mostly follow Marchetti and Nelson's idea (53) concerning the Corbino geometry. However, this discussion will be more detailed and will contain the complete analysis with all needed explanations.

In the Corbino disk geometry, a nonuniform current density given by equation (3.6), $J(r)=I/2\pi Wr$, is produced in the sample by injecting the current at the center and removing it at the outer circumference of the disk. When a magnetic field is applied along the disk axis, the vortices move in circles about the center of the disk. In the flux liquid state, the dynamics on scales larger than the intervortex spacing is described by the hydrodynamic equation (3.11) for the vortex velocity v:

$$-\gamma\vec{v}+\eta\bar{\nabla}_{\perp}^{2}\vec{v}+\vec{F}_{L}=0 \tag{7.1}$$

It would be easier in the end to obtain a solution for a quantity related to the electrical potential since this is what I measure experimentally. Therefore, one rewrites the hydrodynamic equation for the electrical field strength E using the substitution expression:

$$\vec{E}(r)=\Phi_{0}\hat{z}\times\frac{\vec{v}(r)}{c} \tag{7.2}$$

where Φ_0 is the flux quantum. Equation (7.1) now becomes scalar rather than vectorial:

$$-\delta^2\nabla_\perp^2 E + E = \rho_f J \tag{7.3}$$

where $\delta=(\eta/\gamma)^{1/2}$ is the viscous correlation length (or healing length) and ρ_f is the flux flow resistivity. The correlation length represents the size of the region of vortices affected by the boundary through shear viscosity effects. After specifying the boundary conditions the above equation can be solved. Having obtained a solution for E, all that is required to find the potential drop is to integrate the electrical field on the radial interval corresponding to each voltage pair:

$$V_{n,n+1} = -\int_{r_n}^{r_{n+1}} E(r)dr \tag{7.4}$$

The potential drop given by the above expression can be compared to the experimentally measured signal.

For completeness, the intermediary steps of the analysis from equation (7.1) to equation (7.3) are outlined below. We start by writing expression (7.1) explicitly for our case of a tangential vortex velocity, v_θ:

$$-\gamma v_\theta\hat{\theta} + \eta\hat{\theta}\frac{d}{dr}\left(\frac{dv_\theta}{dr}+\frac{1}{r}v_\theta\right) + \vec{J}\times\hat{z}\frac{\Phi_0}{c} = 0 \tag{7.5}$$

The equation is now multiplied by the $\hat{z}$ unit vector to yield:

$$-\gamma\frac{c}{\Phi_0}\vec{E} + \eta\hat{r}\frac{c}{\Phi_0}\frac{d}{dr}\left(\frac{dE}{dr}+\frac{1}{r}E\right) + \vec{J}\frac{\Phi_0}{c} = 0 \quad , \tag{7.6}$$

$$\Phi_0\hat{z}\times\frac{\vec{v}(r)}{c} = \vec{E}(r)$$

noting that . At this point, one may write:

$$\delta^2\left(\frac{d^2E}{dr^2}+\frac{1}{r}\frac{dE}{dr}-\frac{E}{r^2}\right)-E=-J\left(\frac{\Phi_0}{c}\right)^2\frac{1}{\gamma} \tag{7.7}$$

$$\delta^2\left[\frac{1}{r}\frac{d}{dr}\left(r\frac{dE}{dr}\right)-\frac{E}{r^2}\right]-E=-\rho_f J \tag{7.8}$$

where $\rho_f=\Phi_0^2/c^2\gamma$ is the flux flow resistivity. The last expression is identical with equation (7.3), the term between the brackets representing ∇^2E. We have seen in chapter 3 that the radial equation in the model was actually a Bessel equation. Since we are still studying the Corbino geometry, we should expect something similar. Indeed, the above equation can be written as:

$$\delta^2\frac{1}{r}\frac{d}{dr}\left(r\frac{dE}{dr}\right)-\left(1+\frac{\delta^2}{r^2}\right)E=-\frac{\rho_f I}{2\pi W r}, \tag{7.9}$$

which is easily recognized. If the right hand side term were zero and if a change of variable, r''= r/δ, were introduced, we would say that this is a modified Bessel equation with ν=1 (see equation (A.4) in the appendix). Equation (7.9) is an inhomogeneous equation having as the general solution the sum of the inhomogeneous term and the general solution of the modified Bessel equation:

$$E(r)=\frac{\rho_f I}{2\pi W r}+a_1 I_1\left(\frac{r}{\delta}\right)+a_2 K_1\left(\frac{r}{\delta}\right)=\frac{\rho_f I}{2\pi W\delta}\left[\frac{\delta}{r}+c_1 I_1\left(\frac{r}{\delta}\right)+c_2 K_1\left(\frac{r}{\delta}\right)\right] \tag{7.10}$$

The second expression of the solution is prefered and will be used from now on. I_1 and K_1 are the modified Bessel functions of order 1. The c_1 and c_2 coefficients are unknown and they can be calculated by applying the boundary conditions.

The boundary conditions are readily specified for a complete solution to the problem. We already know that by irradiating the center and the edge of the Corbino disk, we pin down the vortices so that our boundary condition is $v = 0$ both at the inner and outer boundaries. From equation (7.2) above, we see that the electrical field should also be zero at the boundaries and it actually represents the suitable boundary conditions for equation (7.3):

$$\begin{cases} E(r)\big|_{r=Ri} = 0 \quad \text{and} \\ \\ E(r)\big|_{r=Rout} = 0. \end{cases} \tag{7.11}$$

Inseting these relations into the solution (7.10), we obtain a system of two equations with two unknowns c_1 and c_2:

$$\frac{\delta}{R_i} + c_1 I_1\left(\frac{R_i}{\delta}\right) + c_2 K_1\left(\frac{R_i}{\delta}\right) = 0 \tag{7.12}$$

$$\frac{\delta}{R_{out}} + c_1 I_1\left(\frac{R_{out}}{\delta}\right) + c_2 K_1\left(\frac{R_{out}}{\delta}\right) = 0. \tag{7.13}$$

After solving the system we obtain:

$$c_1 = \frac{\frac{\delta}{R_i} K_1\left(\frac{R_{out}}{\delta}\right) - \frac{\delta}{R_{out}} K_1\left(\frac{R_i}{\delta}\right)}{K_1\left(\frac{R_i}{\delta}\right) I_1\left(\frac{R_{out}}{\delta}\right) - K_1\left(\frac{R_{out}}{\delta}\right) I_1\left(\frac{R_i}{\delta}\right)} \tag{7.14}$$

and

$$c_2 = \frac{\frac{\delta}{R_{out}} I_1\left(\frac{R_i}{\delta}\right) - \frac{\delta}{R_i} I_1\left(\frac{R_{out}}{\delta}\right)}{K_1\left(\frac{R_i}{\delta}\right) I_1\left(\frac{R_{out}}{\delta}\right) - K_1\left(\frac{R_{out}}{\delta}\right) I_1\left(\frac{R_i}{\delta}\right)} \tag{7.15}$$

The field's radial profile for three values of δ in sample Corbi1* is shown in Figure 51 with continuous lines. Note that δ is varied over three orders of magnitude from 3 to 300μm. The positions of the boundaries are: $r=R_i=30\mu m$ for the inner one and $r=R_{out}=320\mu m$ for the outer one.

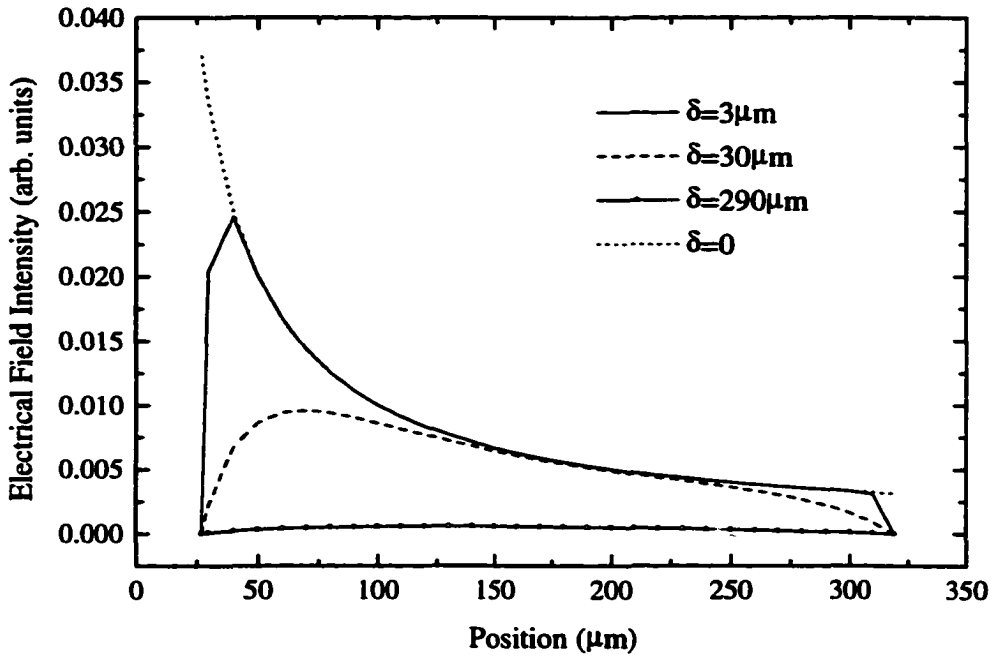

Figure 51. Radial profile of the electrical field intensity for various correlation lengths. The dotted line, which corresponds to zero correlation length, represents the 1/r-behavior.

As you can see, all three calculated profiles go to zero at the boundaries in order to meet the boundary conditions. The dotted line represents the 1/r behavior for the case when there is no vortex viscosity in the crystal (δ=0). As expected, for very small values of the correlation or healing length, δ, compared to the disk radius, most of the sample is not affected by the boundaries. As one can see in Figure 51, the uppermost curve corresponding to δ=3μm is almost identical to the 1/r curve, except for narrow regions next to the boundaries. As the healing length

increases, the profile departs from the dotted line and the suppressed regions widen. When δ reaches the size of the disk, the curve is almost flat.

Our final purpose is to calculate the voltage drop on the contact pair n,n+1:

$$V_{n,n+1} = \frac{\rho_f I}{2\pi W}\left\{\ln\left(\frac{r_{n+1}}{r_n}\right) + c_1\left[I_0\left(\frac{r_{n+1}}{\delta}\right) - I_0\left(\frac{r_n}{\delta}\right)\right] - c_2\left[K_0\left(\frac{r_{n+1}}{\delta}\right) - K_0\left(\frac{r_n}{\delta}\right)\right]\right\} \quad (7.16)$$

The temperature dependence of the correlation length at different magnetic fields can be extracted by fitting the measured voltage to the above expression. Equation (7.16) is the same for any Corbino sample with zero boundary conditions, whether the inside of the disk was irradiated or not. Therefore, the model by itself cannot distinguish between these two cases. However, this can be done by analyzing the temperature dependence of the correlation length close to the liquid-solid transition. If the disk were clean, then we would have a continuous transition to a disordered solid; but if it had been irradiated, we would have a continuous transition as well, but to a Bose glass. As Marchetti indicates in her work (79), the temperature dependence of the correlation length close to the transition is different for the two types of solids; in the former case it is exponential

$$\delta \propto \exp\left(\frac{c}{t^{0.369}}\right) \quad (7.17)$$

and in the latter case it is a power law

$$\delta \propto t^{-\nu_\perp}, \quad (7.18)$$

where $t=(T-T_{transition})/T_{transition}$ and $\nu_\perp$ is the transverse correlation length critical exponent, approximately 1 for the Bose glass.

7.4 Observations from measurements on Corbi1 irradiated

Recall from chapter 6 that, before the setting of the boundary conditions in sample Corbi1, the order relation (3.9) was always respected for magnetic fields smaller or equal to 1T. On the other hand, for fields larger than 1T V_{34} was increasing beyond than V_{23} as the magnetic field increased. The first thing that I noticed after the irradiation of the boundary regions is that V_{34} is never larger than V_{23}. Instead, for H≤1T, there is a temperature regime for which the voltages collected from the first and second contact pairs do not satisfy the order relation (3.9) anymore, more precisely V_{23} becomes larger than V_{12}. For example, we show for comparison in Figure 52 and 53 data taken at 1T field before and after irradiation of the boundaries respectively. As one can see, no change occurred in the normal state, the magnitude of the resistances corresponding to the three pairs remained almost the same after irradiation.

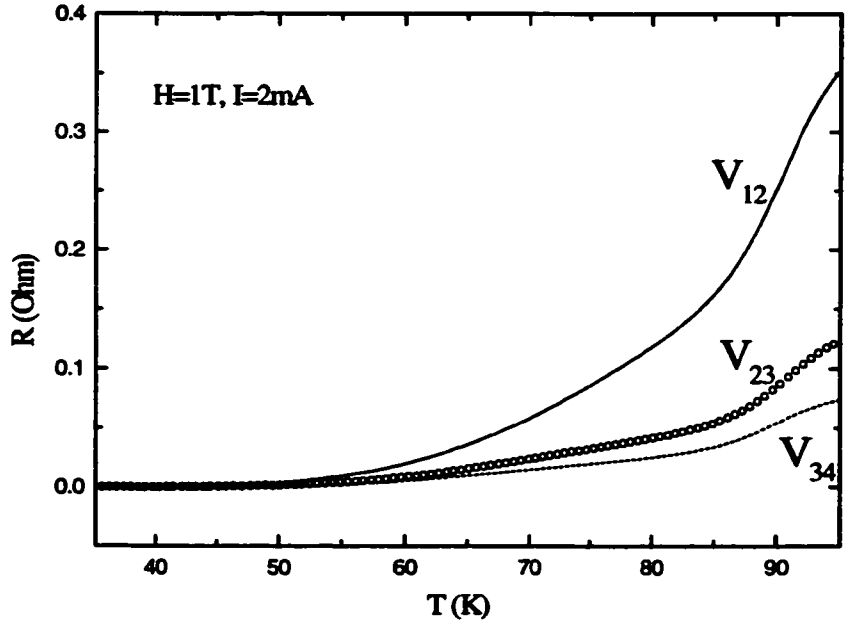

Figure 52. Electrical resistance versus temperature of all radial voltage pairs measured on sample Corbi1 before boundary irradiation.

This, together with the fact that T_c at zero field did not change, is encouraging because it strongly suggests that the experiment was successful; i.e., that the interior part of the disk was not hit by the high energy ions so that its properties were not altered. From Figure 53 you can see that for sample Corbi1*, at temperatures close to the liquid-solid transition, V_{12} decreases below V_{23} as if the vortices located in the proximity of the inner current contact (more precisely between the voltage probes 1 and 2) are slowed down.

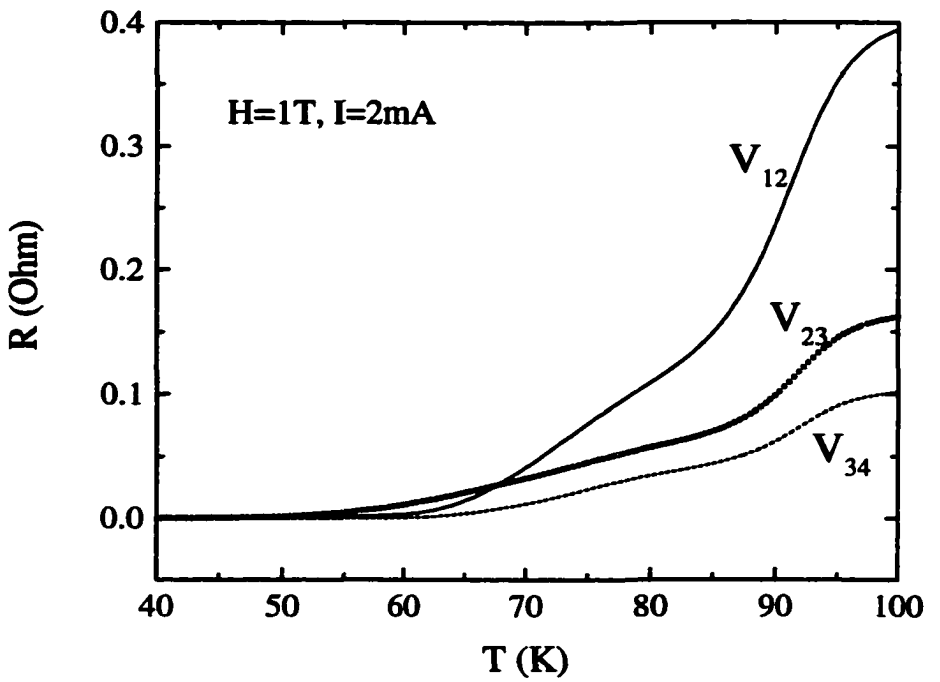

Figure 53. Temperature dependence of the electrical resistance of V_{12}, V_{23} and V_{34} measured on sample Corbi1 after irradiation at an applied magnetic field of 1T. The arrow points to the unusual crossing between the two innermost contact pairs.

Since on the graph it looks like the two curves intersect, from now on we will call this point the crossing of V_{12} and V_{23}. This result is exactly what we were hoping to obtain. Since this feature was not present in the pristine sample and it appeared after irradiation of the edges, we have no

reason not to think that it is connected to the boundary creation and hence to the existence of the vortex shear viscosity in our system.

If one were to build a radial profile using the voltages measured at 1T field, it would look like Figure 54. Each individual curve consists of three points, which correspond to the three voltage drops measured at the same temperature in our Corbi1* sample. The uppermost curve corresponds to the highest temperature and seems to follow a 1/r behavior. As the temperature is reduced, the shape of the profile changes. In fact, if we compare our experimental radial profile with the one resulting from solving the hydrodynamic equation (Figure 51), we clearly see a similarity.

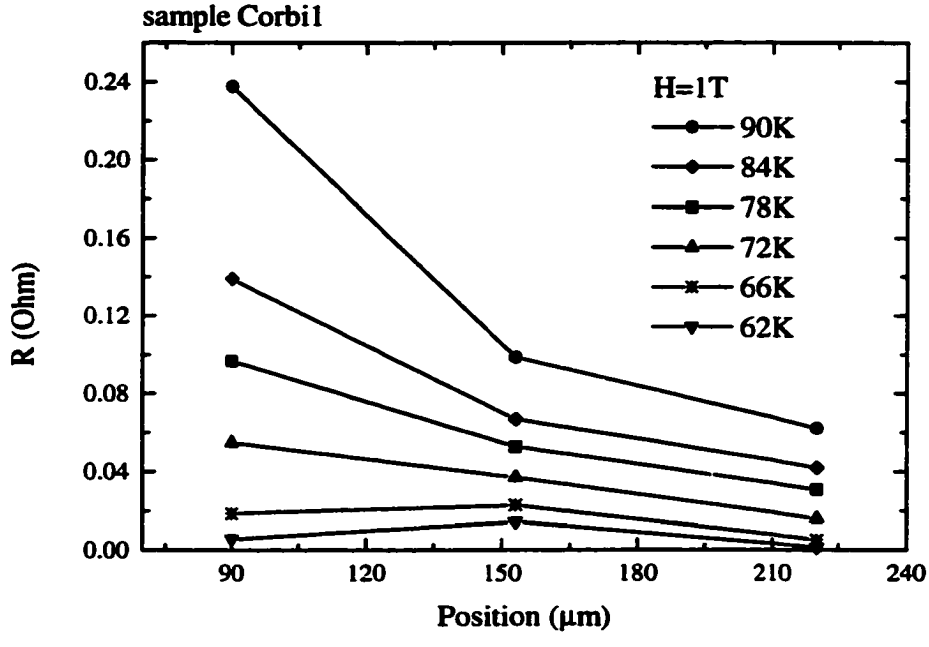

Figure 54. Electrical resistance versus position along the disk radius at constant field of 1T. Each curve corresponds to a fixed temperature.

The bell-like shape of the experimental radial voltage profile at low temperature corresponds to the situation in which the region affected by the boundary extends up to the voltage probes 1 and 2. Consequently, V_{12} is smaller than V_{23}. Moreover, this profile looks similar to the δ=30μm curve in Figure 51.

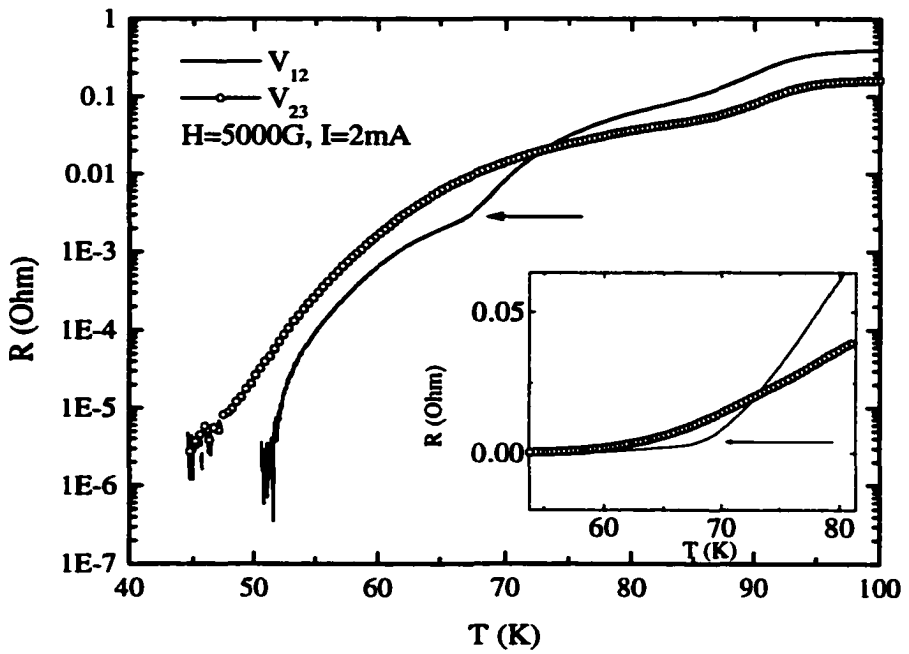

Figure 55. Electrical resistance versus temperature (semilogarithmic plot) for V_{12} and V_{23} of sample Corbi1* at a constant magnetic field of 5000G. The inset contains the same data in a linear scale. The arrows indicate the special feature described in text as a dip.

Figures 52 and 53 display the resistance as a function of temperature for a constant 1T magnetic field, which is coincidentally the value of the dose matching field, B_Φ, for the unirradiated boundaries. From section 7.3, we also know that the boundary conditions work very well for magnetic field strengths less than or equal to B_Φ. But what happens at other applied field

strengths? What is the effect of the crossing? The data shows that the crossing occurs for a wide range of magnetic fields around B_Φ, however the effect is the strongest at $H= B_\Phi$, meaning the relative difference between V_{23} and V_{12} is the largest at 1T.

The raw data displays another feature, which is visible in a linear R vs T graph, but is more obvious in a semilogarithmic scale (see Figure 55). It is a dip or a heel in the resistance curve at low temperatures. The data from the unirradiated sample do not exhibit it. A literature survey reveals that this is the first time that this feature has been observed and so is associated with the unique aspects of the experiment. This feature does not have a sharp characteristic like, for example, a first order melting; however, it can be identified if we make a comparison with unirradiated BSCCO data from chapter 6 or the literature, which all have a smooth round aspect. One can only observe the dip at low magnetic fields for $H \leq B_\Phi$. Furthermore, the feature is present only in data taken from the V_{12} and V_{34} voltage pairs and not V_{23} – as shown in Figure 56, where the arrows in the upper and lower plots indicate the heel or dip. Now, V_{12} and V_{34} are the closest contact pairs to the inner and outer boundaries respectively. Therefore, the special feature must be related to the new boundaries of Corbil* sample.

Finally, it is observed that all voltage pairs exhibit non-ohmic behavior for a very wide range of magnetic fields (see Figure 57). The resistance measured at the same contact pair at the same temperature and magnetic field is different for different driving currents. The non-ohmic behavior usually associated in HTS with some sort of spatial inhomogeneity present in the system that can trap the flux lines (68). Such inhomogeneities can be localized defects, like deviations from the stoichiometry at atomic scale, or can be extended defects, such as dislocations, twin planes or, like in our case, columnar tracks. However, columnar defects should determine the nonlinearity only indirectly, through the viscosity of the vortex matter, since the tracks are located outside the region where the vortices are moving.

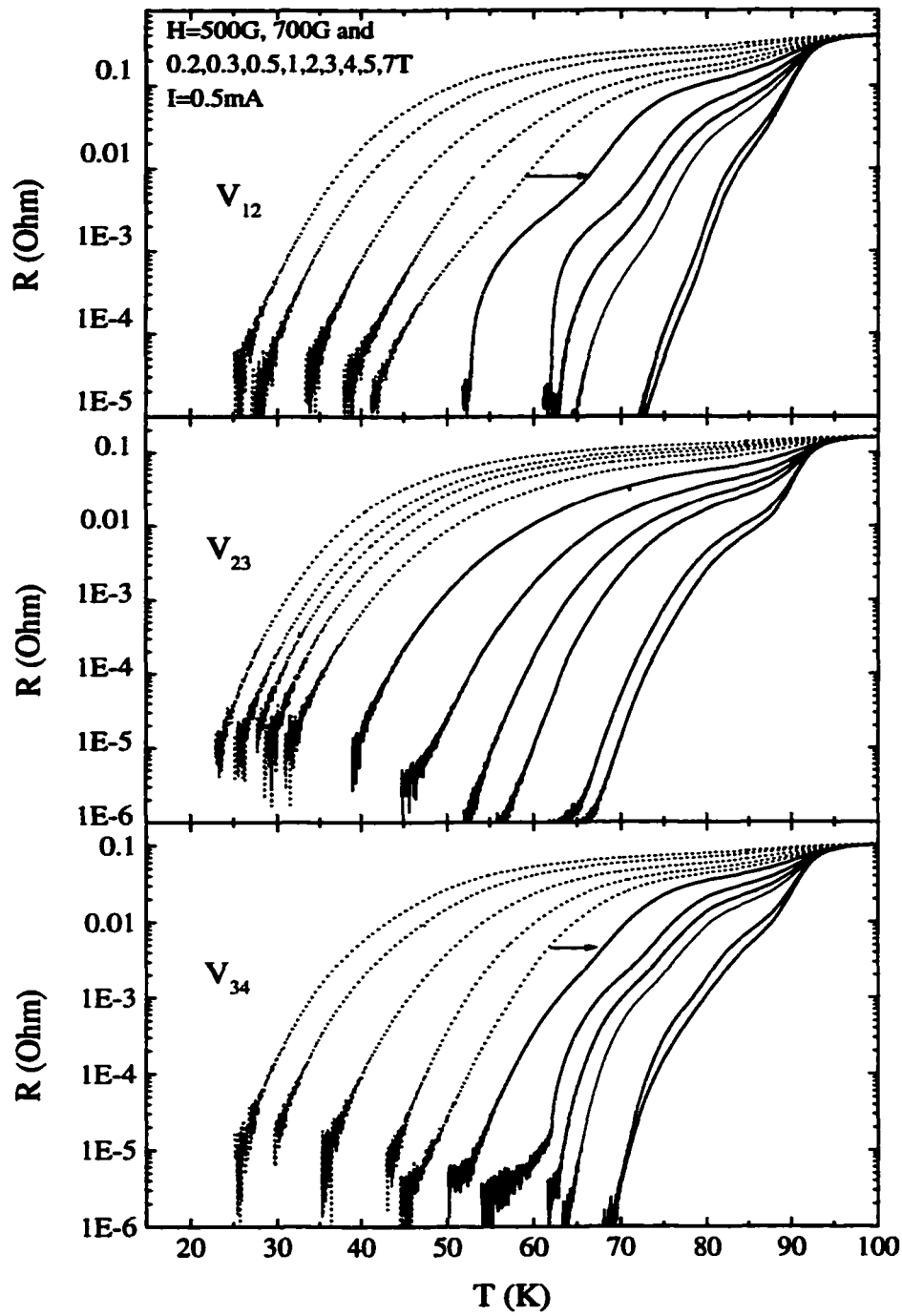

Figure 56. Temperature dependencies of all radial pairs of sample Corbi1* at various magnetic fields. Each plot corresponds to a different voltage pair. The R vs T curves shown in all plots are taken at the same values of the magnetic field. The arrows indicate the presence of the dip.

Although the effect is present for a wide range of fields, I can point out that the resistance nonlinearity is weak at low fields, increases gradually as the magnetic field is increased, is strongest at about 1T and suddenly becomes very weak for H>1T. Also, I notice that for fields around 1T the onset of nonohmic behavior occurs at temperatures where the in-plane resistivity is around 30% of the normal state value for all voltage pairs.

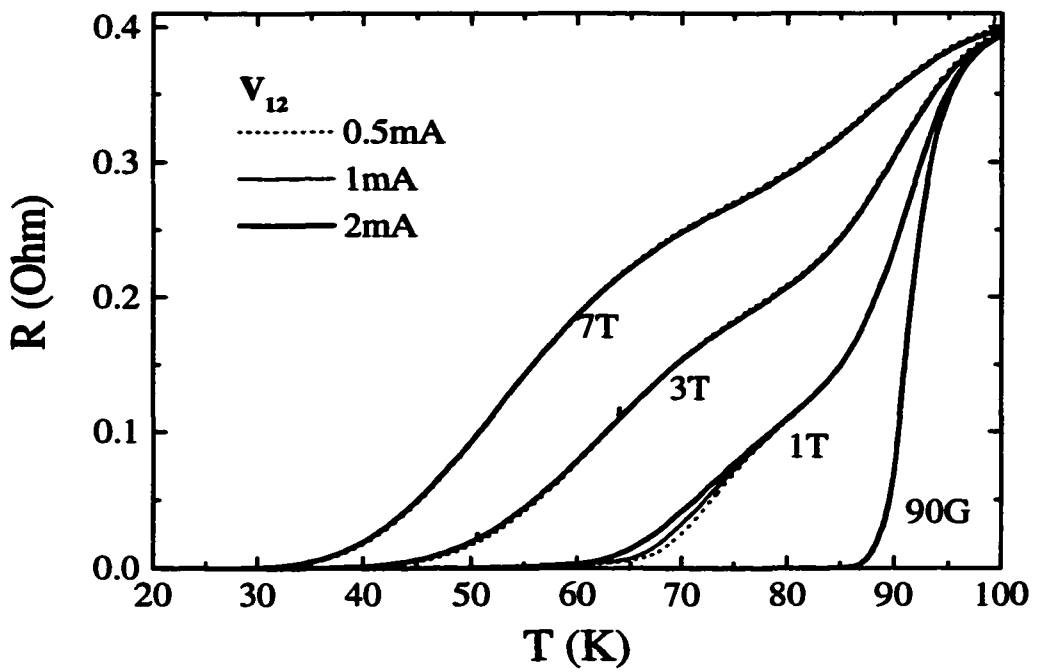

Figure 57. Electrical resistance versus temperature for V_{12} of sample Corbi1* taken at four different magnetic fields with the currents 0.5,1 and 2mA.

It is interesting to remember from chapter 6 that sample Corbi1 displayed only a very weak nonohmic behavior before the irradiation. The pre-irradiation nonlinearity is not visible in linear scale, it can only be observed in semilogarithmic scale as opposed to the post-irradiation nonlinearity which can be clearly seen in linear scale, as shown in Figure 57. Therefore, the

strong nonlinearity presented in Figure 57 must be related to the fact that we irradiated the boundaries. It should be added that the second sample Corbi2 after complete irradiation does not exhibit nonohmic behavior or, at least, it cannot be detected within the limits of measurement sensitivity (see Figure 58).

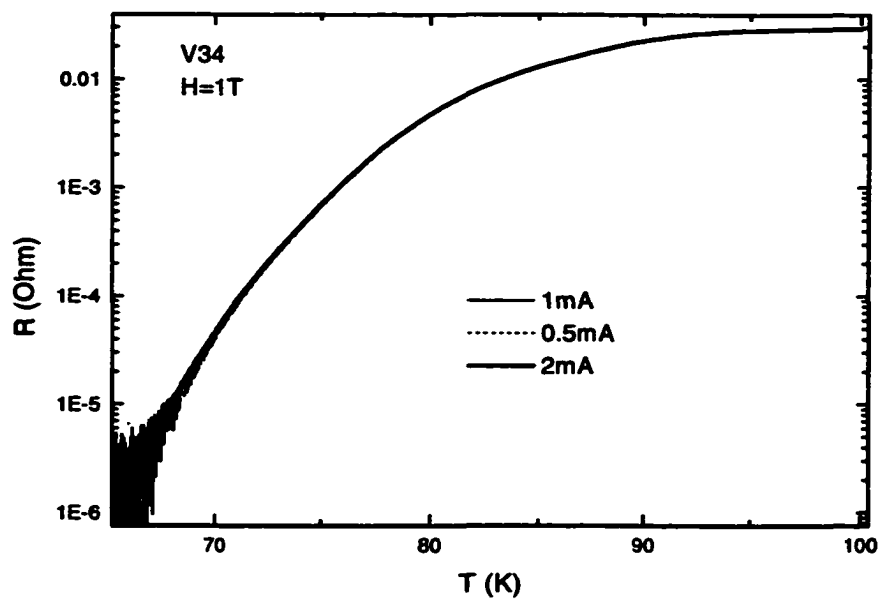

Figure 58. Temperature dependencies of the resistance of V_{34} of sample Corbi2* taken with three different probing currents at a constant magnetic field of 1T.

For the fields smaller or equal with 1T, when the heel is visible, the nonlinearity of the resistance seems to be enhanced by this specific feature. Later in this chapter, the position of the heel will be mapped on the H-T plane together with the onset of nonohmic behavior in order to see any correlation. For fields larger than the matching field, I cannot distinguish anymore the feature in a resistance vs temperature curve and the nonlinearity becomes very weak.

7.5 Irreversibility line of Corbi2 irradiated

After the irradiation, the irreversibility line of sample Corbi2* is clearly and strongly enhanced for all measured fields, as one can see from Figure 59.

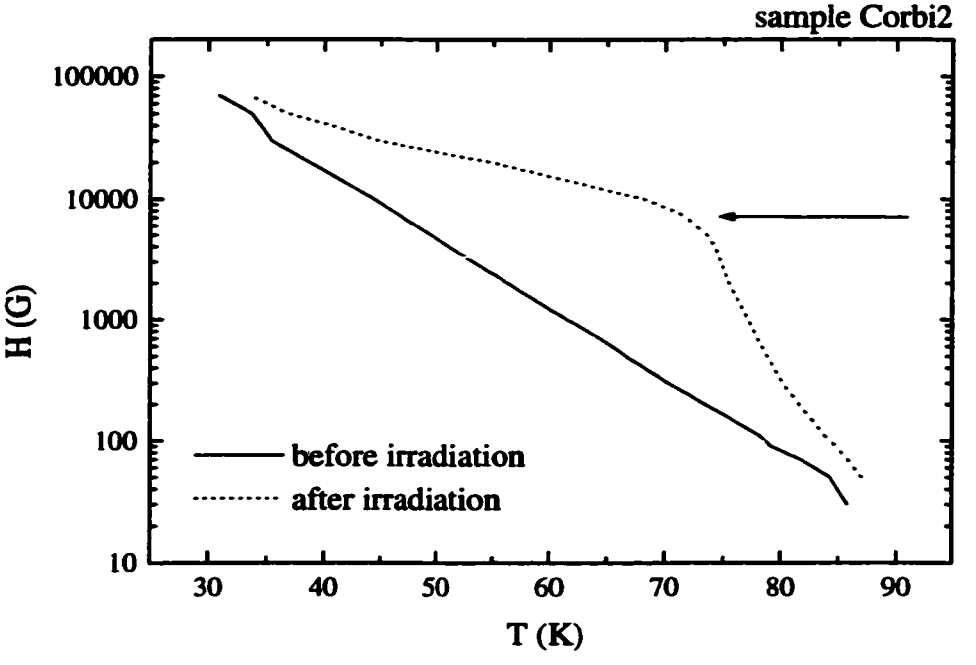

Figure 59. Irreversibility (zero resistance) lines for sample Corbi2 before and after the sample irradiation.

Due to the presence of columnar defects in the disk, the irreversibility line is shifted toward higher temperatures, an effect similar to that described in chapter 5. Pinning from the columnar defects is very effective at high temperatures and vortices freeze, forming a Bose glass.

In Figure 59, the irreversibility lines are obtained from the data measured before and after irradiation on the middle voltage pair of sample Corbi2. I chose this particular pair (see Figure 60) to ensure that the vortex motion is not affected by the boundaries. This is expected to be true

because sample Corbi2 is large so that the middle pair is located far enough from both boundaries and also because we recall that for sample Corbi1* the middle pair seems to be the least affected by the boundary introduction. Indeed, after a more attentive data analysis, it turns out that only the innermost voltage pair is slightly affected by the boundary conditions. In this sample, the effect of the viscosity is only observable very close to the boundaries. I believe this happens due to the fact that we have added to many columnar defects inside the disk and the pinning provided by these defects is much stronger than the vortex viscosity. In other words, I cannot perform a shear study on sample Corbi2*. However, the information obtained from this sample is very valuable for the analysis of the data obtained from sample Corbi1*.

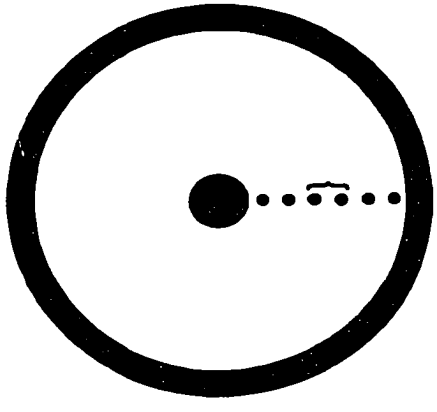

Figure 60. Voltage probe configuration for the sample Corbi2. The data analyzed in the text was measured on the contact pair indicated in the figure.

We notice that the irreversibility line of sample Corbi2* (Figure 59) exhibits a more structured shape than that of the pristine sample. Similar data were previously reported for irradiated BSCCO 2212 single crystals by D. Zech *et al* in 1995 (80). Two characteristic features are observed. First, as we decrease the temperature, there is a kink in the irreversibility line at

about T'=75K, where a very rapid temperature dependence occurs. Here the shift of the irreversibility line toward high temperatures is most pronounced, and it is believed to be associated with the moment when the flux lines are trapped by the columnar defects. We can then roughly identify T' as the depinning temperature where the thermal energy becomes comparable to the pinning energy, so that for T>T' the flux lines start to delocalize from the columnar defects. Note that we are using the term flux lines for BSCCO-a material that is renowned for its layered structure, which determines that vortices exist as 2D pancakes in the CuO_2 layers. However, it was showed that the presence of the columnar defects induces a longitudinal correlation along the c-axis so that pancakes from different layers couple into a flux line (81,82).

As the temperature is decreased, a second feature is encountered in the irreversibility line. At $H=B_\Phi=1T$, there is a clear cross-over from the fast temperature dependant regime to a slow temperature dependant regime. Zeck *et al* in ref (83) identify it as the crossover from the single-vortex strong pinning regime to plastic or collective weak pinning regime (68).

At low fields, the vortex ensemble is characterized by the competition between pinning and thermal fluctuations. For temperatures less than T' and fields smaller than the matching field, the defects give rise to correlated disorder along the track directions and constitute strong pinning sites for the flux lines that remain trapped despite the presence of thermal fluctuations. For temperatures greater than 75K, the strength of the anisotropic pinning is decreasing toward T_c, as thermally induced fluctuations cause increasing delocalization of the vortices.

For fields much larger than $B_\Phi$and low temperatures, the correlated disorder competes with the point disorder and vortex-vortex interaction. The influence of columnar defects becomes gradually isotropic and the irreversibility line of the irradiated sample approaches the one of the unirradiated crystal.

The upward portion of the irreversibility line between the two regimes was identified by Zech *et al* as the accommodation field line (83).

7.6 Phase diagram of Corbi1 irradiated

In order to better understand the preliminary observations made in section 7.4, I will collate the information available from both samples, Corbi1* and Corbi2*, on a common phase diagram. The compiled phase diagram in Figure 61 contains, for Corbi1*, the irreversibility line of V_{23}, the onset of non-ohmic behavior, the position of the special feature of the R vs T at fixed field curves, and the position of the crossing between V_{12} and V_{23} data, together with the irreversibility line of the central voltage pair from sample Corbi2*.

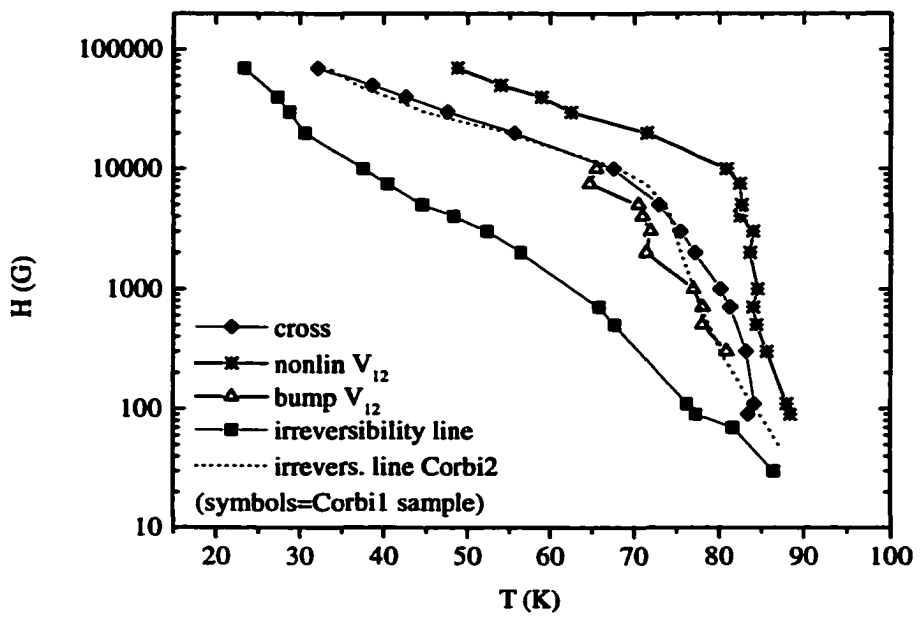

Figure 61. Composite HT diagram containing the zero resistance (irreversibility) lines for samples Corbi1* and Corbi2* together with the crossing line, the onset of nonlinearity line and the heel line for sample Corbi1*.

I should mention that all irreversibility lines consist of (H,T) pairs with T being the temperature at which the measured resistance reaches a low value(10^{-5} Ohm) situated just above the noise. The onset of nonohmic behavior is defined by the temperature where the splitting between the resistance curves taken on the same contacts pair occurs at the same applied magnetic field, but at different current values. Finally, the special feature is referring to the pronounced heel that we have described in section 7.4. Since this feature consists of a smooth change in slope of the resistance versus temperature curve, we need to establish a criterion for determining its position. I chose the temperature resulting from the intersection of two lines that follow the two slopes, shown in Figure 62, to be the value mapped in the H-T space.

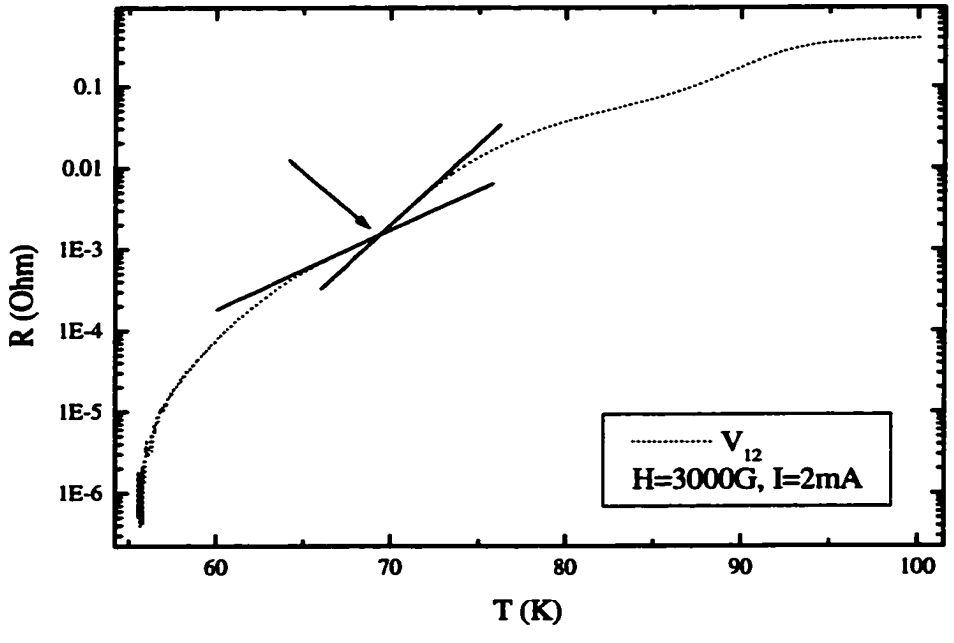

Figure 62. Electrical resistance versus temperature for V_{12} of sample Corbi1* at 3000G in a semilogarithmic plot. The temperature of the dip is determined as the intersection of the two slopes.

The leftmost line represents the irreversibility line of V_{23} from sample Corbi1* estimated from resistivity measurements conducted after the boundary irradiation. From Figure 63, where I plot together the irreversibility lines of V_{23} before and after the irradiation, one can see that the two curves are very close one to the other.

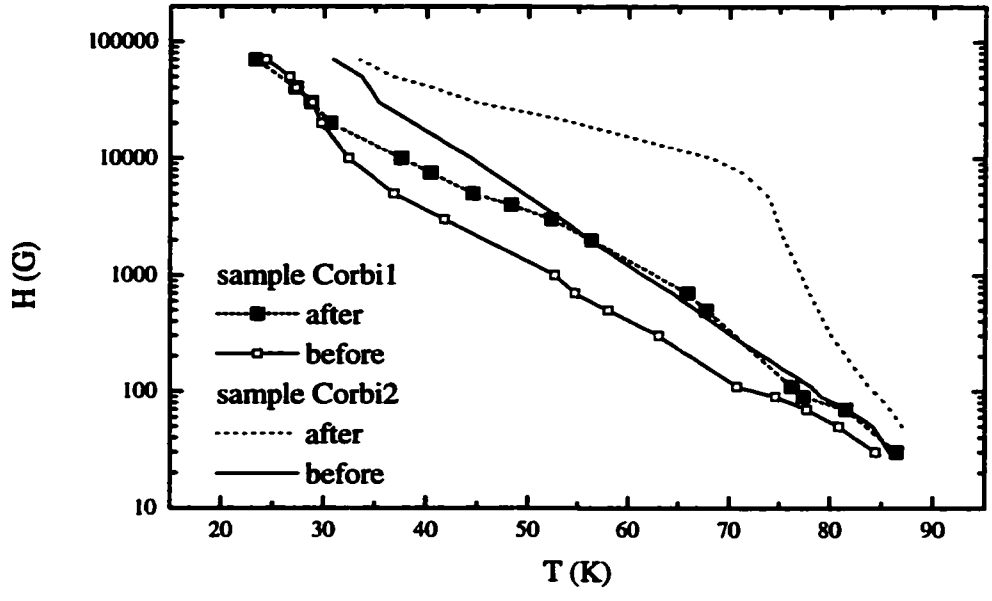

Figure 63. Irreversibility lines for samples Corbi1 (square symbols) and Corbi2 determined from data taken before (solid lines) and after the samples irradiation (dotted lines).

The dotted line in Figure 61 is the irreversibility line of sample Corbi2 that was described in section 7.5 and is situated above the irreversibility line of the unirradiated disk, as it should be. Recall that the dotted line gives an approximate measure of the temperatures and fields at which the flux lines in the boundary regions are frozen and pinned by the columnar defects. The space in the H-T plane between the two irreversibility lines gives us the temperature and field ranges where the vortex liquid motion inside the disk should be affected by the boundaries; this is when

one should see the effects of shear viscosity. And indeed, as seen in section 7.4, we do see a number of interesting features, which will be discussed below.

We start with the crossing line (the diamond symbols in Figure 61), which has a spectacular similarity in both position and shape with the irreversibility line of sample Corbi2* for fields both smaller and larger than the dose B_Φ=1T.

As far as the special feature is concerned (triangle symbols in Figure 61), the heel line agrees very well with the ascending portion of the irreversibility line of sample Corbi2, which corresponds to the temperatures when the flux lines get pinned in the irradiated regions (see section 7.5). However, the line of data is quite short since the heel appears only for a narrow window of applied magnetic fields. Also the line is very noisy due to a large estimation error; recall that the feature has a smooth characteristic, making it hard to determine its absolute position. Nonetheless, we could say that the dip in the resistance versus temperature curves, taken at the contact pairs close to the boundaries in sample Corbi1*, is caused by the freezing of the vortices in the boundary regions. Why is it that we do not see this distinctive feature above the dose matching field? As expected, the boundary's strength is reduced by the fact that some of the vortices in the boundary regions are not pinned. When an electrical current is applied, it is possible that the unpinned vortices from the boundaries are dragged by their immediate neighbors, which are moving under the influence of the Lorentz force. The behavior at magnetic fields above B_Φ, when the vortices outnumber the columnar defects, can be interpreted as a weakening of the overall pining efficiency as the vortex-vortex interaction begins to dominate.

It is obvious from Figure 61 that the line describing the onset of nonohmic behavior also follows closely the irreversibility line of sample Corbi2*, although it is situated at higher temperatures. The change in slope of the onset of nonlinearity line occurs at approximately H=1T, which coincides with the matching field for the irradiated region under the contact pads.

I suspect that there is a temperature shift between the irreversibility line of sample Corbi2 and the boundary regions of sample Corbi1. This shift could be caused by a slight difference between the superconducting properties of the two BSCCO crystals. For example, if sample Corbi2 had a smaller T_c than sample Corbi1, then the entire irreversibility line of the former would be shifted correspondingly towards lower temperatures. We have to remember that the disk dose is slightly smaller than 1T, this could also be the reason for the position of the irreversibility line. As we learned in chapter 5, the smaller the dose the lower the irreversibility line lies in the H-T plane. The shift could be artificially created by the fact that the irreversibility line of sample Corbi2 is determined from dynamical measurements, meaning vortices were set in motion, while the vortices in the boundary regions in Corbi1 do not experience a Lorentz force as we already discussed in section 7.1. Depending upon the magnitude of the electrical current with which the vortex matter is probed, the resulting irreversibility line could shift; the higher the current, the more the line is shifted toward lower temperatures. Any of the above could be true and lead to a temperature shift of the irreversibility line of the boundary. However, the cumulated shift cannot be greater than $\Delta T=5K$. Thus, since the position of the dotted line in Figure 61 will change only by a little, the discussion of the experimental results remains the same.

Keeping in mind that the irreversibility line of sample Corbi2* is representative for vortex physics in the boundary regions, I believe that the agreements found above provide a proof that the experimental results from sample Corbi1* are a consequence of the boundary irradiation.

7.7 Healing length

While trying to fit our experimental data to the theoretical expression (7.16), a difficulty was encountered. The fitting could not be performed. There were sometimes orders of magnitude difference between the model and the actual data. After some discussion with colleagues, it became clear that the problem in the model was with the flux flow resistivity factor, ρ_f, in

expression (7.16). All the values of ρ_f found in the literature were tried in the model and failed. It turns out that no pristine BSCCO crystal can exhibit flux flow because of the structural defects that exist in the crystal. Therefore, ρ_f is the correct factor only for the ideal case of flux flow. Thus in our case, we need to replace ρ_f with the resistivity of the sample before irradiation, and that we are able to do since we measured the sample before we introduced the boundary conditions. After making this adjustment in the model, I was able to fit the experimental radial profiles to expression (7.16) for the potential drop. The results are presented below. The fitting process involves two sets of experimental data, one taken on the pristine sample and the other one taken after the boundary irradiation. I would like to stress the importance of having the Corbino disk measured before the boundary creation, since the theoretical paper (53) implies that one can obtain information about the correlation length just by measuring the sample after the irradiation.

We start by fitting the potential measured from the first pair of contacts V_{12}. First, using the theoretical result and the pre-irradiation data set, I calculate the values of the potential drop for several values of the healing length (chosen to cover the entire allowed range) and then these are matched with the post-irradiation experimental data. The healing length estimation for the 5000G data taken with a current of I=2mA is presented in Figure 64. The error is approximately $\pm 15\mu m$. I chose to do the estimation at 5000G since the transport data show that for this magnetic field the combination between boundary conditions and vortex viscosity is most efficient. As one can see, for temperatures larger or equal to 78K the correlation length δ is zero, meaning that there is no shear viscosity or the zero vortex velocity boundary conditions are invalid.

I also compared the V_{12} data taken at H=5000G before and after the boundary irradiation. From Figure 65, we see that for $T \geq 78K$ the two curves coincide, corresponding to $\delta=0$. For $T<78K$, the post-irradiation data deviates towards smaller values, reflecting a reduced dissipation and, therefore, a reduced vortex mobility for the same applied Lorentz force.

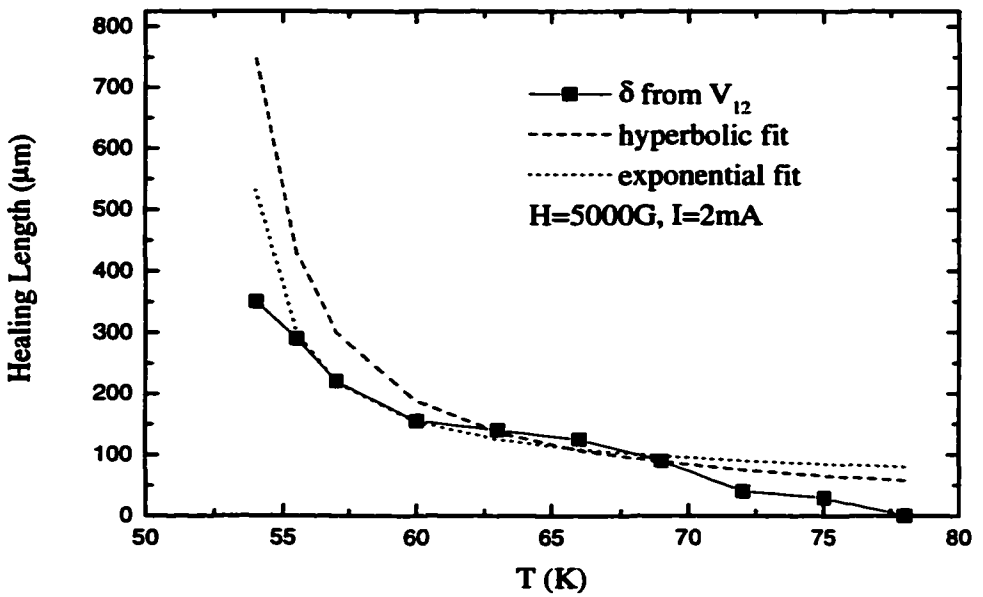

Figure 64. Estimated values of the healing length (square symbols) for sample Corbi1* obtained from fitting the signal collected from V_{12} at 5000G to the theoretical solution (see the text). The dashed and dotted lines represent hyperbolic and exponential fit to the estimations of δ.

The temperature dependence of the vortex viscosity can be understood intuitively. Assuming that at low temperatures the vortex-vortex interaction gives rise to the viscous behavior, as the temperature is increased, we expect that the thermal effects would wash out the interactions that produce viscosity. However, I cannot be certain of that, because we expect that the upper limit of the temperature range, for which the boundary conditions are zero, is also close to 78K at 5000G. One can see this from the irreversibility line of the irradiated sample in Figure 59. Now, according to Marchetti's model (53), having the boundary vortex velocity zero is a necessary condition for observing the shear viscosity.

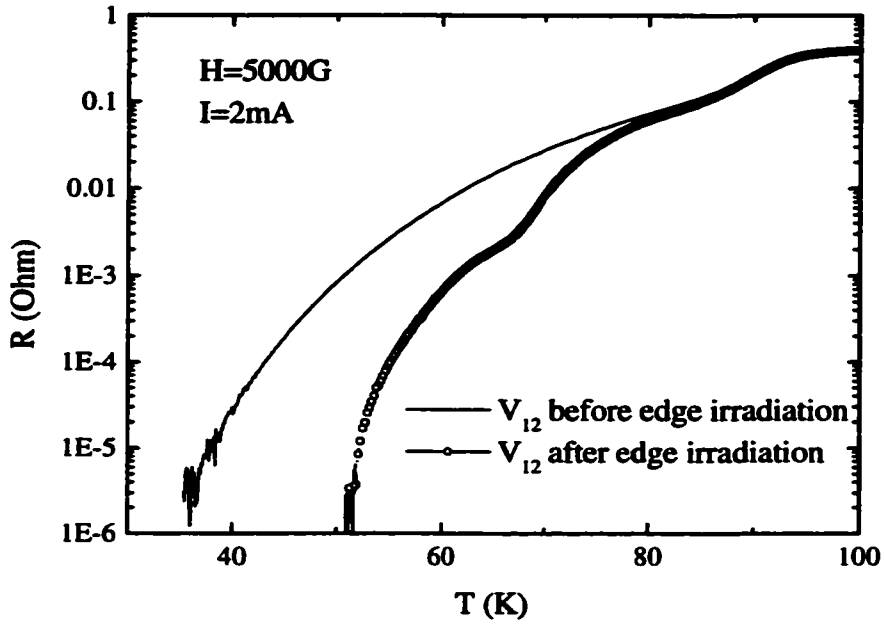

Figure 65. Temperature dependencies of the electrical resistance of V_{12} in sample Corbi1 at 5000G before (line) and after (symbols) the boundary irradiation.

I believe it is possible to also observe vortex viscosity in a Corbino sample without boundary conditions, as the experiment presented in chapter 6 shows. In Marchetti's model the moving vortices interact to each other as well as with an inhomogeneity (present in the boundary region) and as a result, they are slowed down, which is exactly what we observe in chapter 7. In the experiment described in the previous chapter, the moving vortices interact among themselves only, modifying each other's velocity.

The fitting analysis can be repeated for measurements done at different driving currents; for example, I looked at data taken with I=0.5mA. We already saw earlier that the sample resistivity is nonohmic for temperatures above the freezing transition associated with each magnetic field. These are exactly the regimes where viscosity becomes observable. Therefore, clearly, there is going to be a difference in the fitting results. Since lower current produces a

smaller dissipation, we can say that the correlation length will be larger for smaller currents, as illustrated in Figure 66.

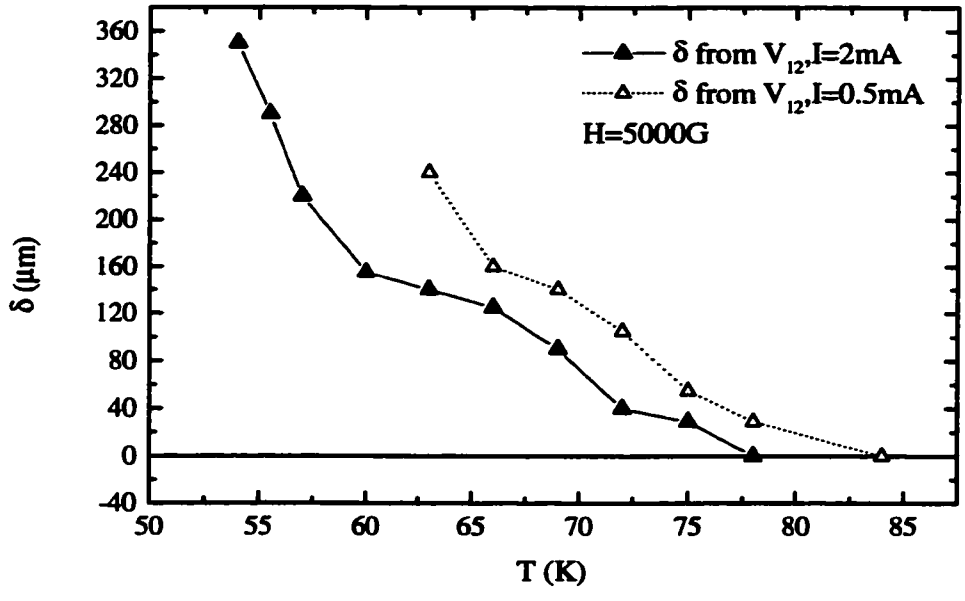

Figure 66. Correlation length estimated from data measured on V_{12} of sample Corbi1* at 5000G with two different currents 0.5 and 2mA.

A fitting similar to the one in Figure 64 can be performed for the other two radial voltage pairs. When we compare the healing lengths estimated for the three voltage pairs we notice differences. The correlation length resulted from fitting the V_{34} data to the model is larger than the one given by V_{12} (see Figure 67), while the values estimated for δ from V_{23} are smaller than the ones from V_{12}. There is an explanation for this trend. I will start by comparing V_{12} and V_{34}, the two pairs of contacts situated closest to the boundaries. One might expect that the estimated values for δ from these two voltage pairs to be very close since the two boundaries are similar to the extent that they both contain columnar defects that can trap the flux lines. Instead, we see a

clear difference between the two upper curves in Figure 67. This is because they are not equivalent, since one is convex and the other is concave.

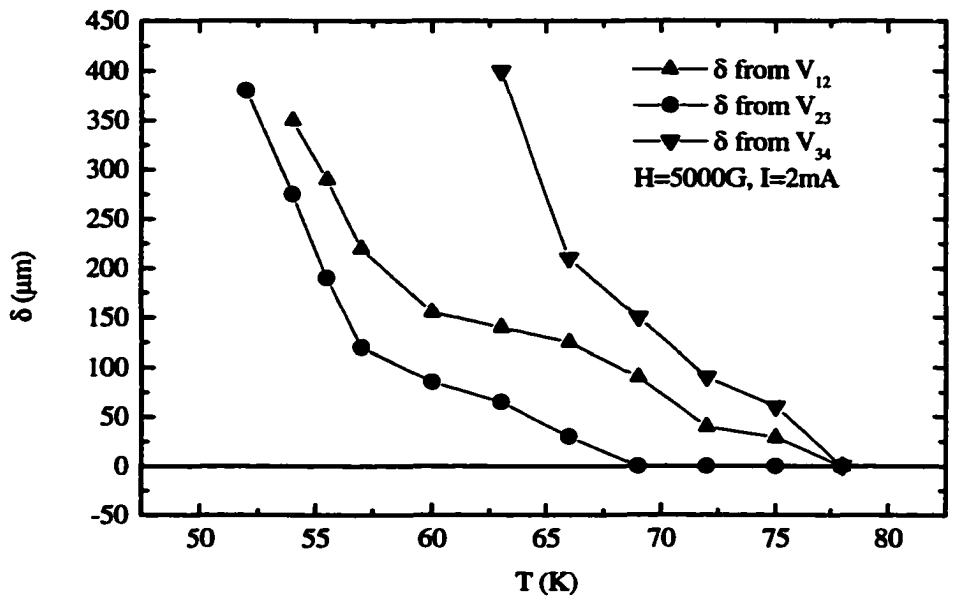

Figure 67. Estimations of the healing length obtained from analyzing the data measured on the three radial voltage pairs of sample Corbi1* at 5000G.

Furthermore, their sizes are not equal; the inner boundary has a much smaller contact surface with the moving vortex fluid than the outer boundary. This difference can account for our fitting result: the estimation of the correlation length from V_{34} data is larger due to the fact that the vortices feel a stronger influence from the outer boundary. In addition, the current density is much smaller closer to the outer edge than at the center of the sample. It is possible that when the vortices have a smaller velocity due to the Lorentz force at the outer boundary, they have increased interactions with the boundary resulting in a further reduced velocity. Actually, this behavior has been seen before when we talked about the nonlinearities. There are temperatures and fields for which a

lower current density is associated with a lower dissipation; therefore, slower motion which is equivalent with a larger healing length.

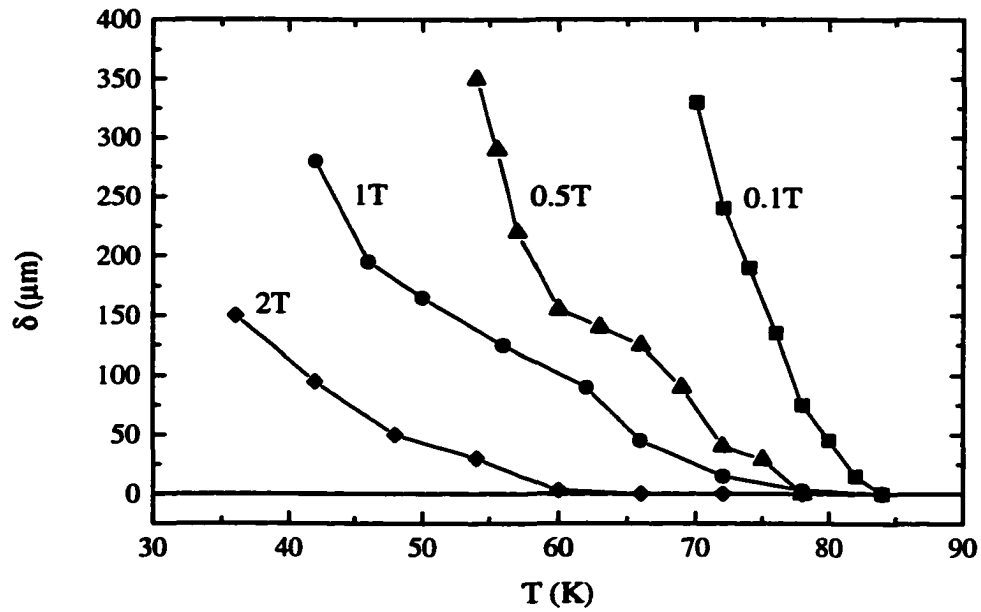

Figure 68. Correlation length estimated from data measured on V_{12} of sample Corbi1* with a current of 2mA at 0.1,0.5,1 and 2T.

The correlation length estimated from data taken on V_{23} is smaller than any of the estimations obtained from the other two pairs. We have noticed when analyzing the data that the middle pair is only slightly affected by the irradiation of the boundaries. Therefore, it is not a surprise that the correlation is weaker at the mid-point between the boundaries.

Finally, we have estimated the healing length for various magnetic fields around 5000G and we present the results in Figure 68. A consistent trend is noticed. At the same temperature the correlation length is decreasing if the magnetic field is increased. This can be connected with the

fact that as the magnetic field is increased the boundary conditions set in at a lower temperature, making the vortex viscosity effect observable at lower temperatures.

In conclusion, the effect of the boundaries on the vortex motion depends of the viscosity of the vortex matter. From the 5000G data (Figure 67), one can see how the healing length δ increases gradually from zero as the temperature decreases below 78K. At low temperatures, just before the freezing, δ exhibits an upturn that corresponds to enhancement of the viscous effects due to the solidification of the vortex liquid. However, the estimation for δ at low temperature falls below the hyperbolic fitting shown as dashed line in Figure 64. Clearly, the shear viscosity of the vortex matter in the present experiment is not as strong as predicted in reference (53) since it is induced by vortex-vortex interactions only. In their work (53), Marchetti and Nelson expect to see a greater viscosity due to vortex line cutting close to the transition to a Bose glass. Since the annulus Corbi1 has not been irradiated, there could be no Bose glass in this sample. However, the healing length estimation comes very close to the exponential fit shown as a dotted line in Figure 64. This type of temperature dependence confirms that I detected viscosity effects close to the transition from a vortex liquid to a disordered vortex solid phase, as described in section 7.3.

8. CONCLUSIONS

The subject treated in the present work is part of the vortex physics in high temperature superconductors. In particular, I have studied aspects of the vortex dynamics in $Bi_2Sr_2CaCu_2O$ single crystals prepared into the Corbino disk geometry. The Corbino geometry, named after the scientist who first used it, provides a contact configuration with cylindrical symmetry. As a consequence, the electrical current flows radially from the inner central electrode towards the outer one. Thus, the current density is not uniform, its radial dependence being dictated by the charge conservation. When an external magnetic field is applied, the BSCCO crystal, as a type II superconductor, is penetrated by vortex flux lines each carrying a flux quantum Φ_0. As of result of the interaction between the vortices and the electrical current applied to the Corbino sample, the flux lines move on closed circular trajectories inside the disk without crossing the edges of the crystal. Therefore, the Corbino disk geometry is the perfect sample configuration for the study of the bulk transport properties of the material, BSCCO 2212 in our case.

I have investigated the surface barrier effects on the transport properties of BSCCO in the mixed phase by comparing the transport measurements obtained from crystals patterned in the Corbino disk geometry and the four-probe configuration. In the latter contact configuration, when the electrical current is applied, the vortices cross both edges of the sample. Therefore, the transport measurements obtained from such a sample must contain contributions from both bulk and surface properties. The crystal edges affect the vortex motion through such mechanisms as the Bean-Livingston barrier and the geometrical barrier. I have prepared multiple Corbino and standard bar samples from BSCCO 2212 single crystals and measured their electrical properties. I have then compared the transport data measured on samples with different configurations and noticed no considerable difference. Furthermore, I have cut three of the Corbino samples into standard bar geometries and then I have measured them again. In this case, the very same crystal with the same bulk properties is investigated in two different contact configuration. Any

difference between the two sets of data must consist of surface effect contributions. Again, I have found perfect agreement between the electrical resistance measurements of the Corbino sample and the corresponding data from the laminar sample. The conclusion from this experiment is that the surface barriers have no or negligible effect on the transport properties for the studied BSCCO 2212 crystals. However, the ratio between the bulk pinning and the surface pinning depends on the crystal quality. The quality of BSCCO depends on the growth conditions and, as a consequence, some crystals could have more defects than others. It is possible that for crystals with high levels of disorder, the surface pinning is much smaller than that in the bulk so that the surface effect cannot be detected in the transport measurements. On the other hand, in clean specimens, the contribution from the surface barriers becomes important and could affect the transport properties measured on four-probe samples. This problem can be avoided if Corbino configurations are used instead.

A very interesting and important physical quantity of the vortex physics is the vortex shear viscosity. As the name indicates, the viscosity is due to shear of the vortex matter. Usually the shear is associated with a vortex solid state, when the shear modulus is different from zero. However, there are cases in which the viscosity appears also in the vortex liquid state due to a large vortex-vortex interaction or due to vortex entanglement. In any case, the viscosity is rarely observed since specially patterned samples are necessary to highlight this phenomenon. It is even more difficult to directly probe and measure the viscosity coefficient. In chapter 6 of this work, I show evidence of transverse vortex correlation due to the viscosity in the transport measurements done on BSCCO Corbino samples with multiple radial voltage contacts. Mainly, what I have found is that at high magnetic fields the vortices located close to the outer frame are moving faster than they should if they were following the local Lorentz force. The fast motion of these outer vortices can be explained by the fact that they are dragged by the adjacent moving flux lines, which have a larger velocity since they are driven by a larger Lorentz force. The observation of the vortex viscosity in the vortex liquid was possible only in a Corbino sample,

because it exhibits a velocity gradient different from zero. I believe that the results presented in chapter 6 are an evidence of the vortex viscosity. However, since the experimental data could not be fitted to the theoretical prediction, a numerical value for the viscosity coefficient could not be derived from them.

In chapter 7 I have gone a step further by determining the correlation length from the transport data taken on a BSCCO Corbino sample with irradiated boundaries. Columnar defects were introduced in the boundary regions with the purpose of creating known boundary conditions. These in turn were necessary in order to obtain a solution for the electrical potential that could be fitted to the experimental data. Specifically, there is a temperature and field regime when the vortices in the boundary regions will be trapped by the columnar defects and therefore their velocity will be zero, which constitutes the required boundary condition. The analysis of the transport measurements obtained from such a sample show the effects of the vortex viscosity in the vortex liquid state. I have solved the equation of motion for a Corbino disk with zero velocity boundary conditions and obtained a solution for the electrical potential. Lastly, I have fitted the experimental results to the solution and obtained numerical values for the healing length associated with the vortex viscosity, which are presented in chapter 7.

The experiment presented in chapter 7 could be continued by irradiating a Corbino sample differentially, with a high dose in the boundary regions and a much lower dose inside the disk. The entire experiment can be repeated in different materials for the purpose of deriving the values of the vortex viscosity for those materials and also for studying the various kinds of phase transitions. For example, one could also introduce point defects in the crystal, not only columnar defects. As shown in chapter 7, the magnitude of the dose matching field has to be chosen carefully. In other words, a systematic study, similar to the one in chapter 5, has to be completed in order to establish which is the appropriate value for the dose in order to put in evidence the vortex viscosity phenomenon. While the columnar defect study from chapter 5 involved the full irradiation of the crystals, in the experiments that I propose, the dose received by the boundary

regions should be much larger than in the rest of the sample. The investigation of the vortex viscosity can also be extended by performing measurements at various values of the ac frequency. As seen from this work, a large number of voltage probes is necessary for a better spatial analysis of the data. Despite the difficulties encountered while preparing the Corbino samples, this geometry is a powerful tool for the study of vortex correlation associated with various phases of the vortex matter.

APPENDIX

The inverse Fourier transform of f(r) is:

$$f(\vec{k}) = \int d^2 r f(r) e^{-i\vec{k}\cdot\vec{r}} = \int d\theta \int r dr f(r) e^{-ikr\cos\theta} = 2\pi \int r dr f(r) J_0(kr)$$

since

$$\int_0^{2\pi} d\theta e^{ia\cos\theta} = 2\pi J_0(a)$$

The conjugated relation is:

$$f(\vec{r}) = \int \frac{d^2 k}{(2\pi)^2} f(\vec{k}) e^{i\vec{k}\cdot\vec{r}} = \frac{1}{2\pi} \int k dk f(k) J_0(kr)$$

The simplified relations used in Chapter 3 are the following:

$$f(r) = \frac{1}{2\pi} \int k dk f(k) J_0(kr) \qquad \text{(A.1)}$$

$$f(k) = 2\pi \int r dr f(r) J_0(kr) \qquad \text{(A.2)}$$

Bessel equation:

$$\frac{d^2Y}{dx^2}+\frac{1}{x}\frac{dY}{dx}+\left(1-\frac{v^2}{x^2}\right)Y=0 \tag{A.3}$$

Modified Bessel equation:

$$\frac{d^2Y}{dx^2}+\frac{1}{x}\frac{dY}{dx}-\left(1+\frac{v^2}{x^2}\right)Y=0 \tag{A.4}$$

CITED LITERATURE

1. Onnes H. K., *Leiden Comm.*, 120b, 122b, 124c, 1911.
2. Meissner W. and Ochsenfeld R., *Naturwissenschaften*, 21: 787, 1933.
3. London F. and H.: The electromagnetic equations of the supraconductor. *Proc. Roy. Soc. (London)*, A149: 71-88, 1935.
4. Ginzburg V. L. and Landau L. D., *Zh. Eksperim. i Teor. Fiz.*, 20: 1064, 1950.
5. London F.: *Superfluids*, vol. I, pp. 152, New York, Wiley, 1950.
6. Abrikosov A. A.: On the magnetic properties of superconductors of the second group. *Sov. Phys. JETP*, 5: 1174-1182, 1957.
7. Anderson P.W.: Theory of flux creep in hard superconductors. *Phys. Rev. Lett.*, 9: 309-311, 1962.
8. Lynn J. W., Rosov N., Grigereit T. E., Zhang H., and Clinton T. W.: Vortex dynamics and melting in niobium. *Phys. Rev. Lett.*, 72: 3413–3416, 1994.
9. Safar H., Gammel P. L., Huse D. A., Bishop D. J., Lee W. C., Giapintzakis J., Ginsberg D. M.: Experimental evidence for a multicritical point in the magnetic phase diagram for the mixed state of clean untwinned $Yba_2Cu_3O_7$, *Phys. Rev. Lett.*, 70: 3800–3803, 1993.
10. Safar H., Gammel P. L., Huse D. A., Bishop D. J., Rice J. P. and Ginsberg D. M.: Experimental evidence for a first-order vortex-lattice-melting transition in untwinned, single crystal $YBa_2Cu_3O_7$. *Phys. Rev. Lett.*, 69: 824-827, 1992.
11. Kwok W. K., Fleschler S., Welp U., Vinokur V. M., Downey J. and Crabtree G. W.: Vortex lattice melting in untwinned and twinned single crystals of $YBa_2Cu_3O_{7-delta}$. *Phys. Rev. Lett.*, 69: 3370-3373, 1992.

12. Liang, R., Bonn, D.A. and Hardy, W.N.: Discontinuity of reversible magnetization in untwinned YBCO single crystals at the first order vortex melting transition. *Phys. Rev. Lett.*, 76: 835-838, 1996.

13. Welp, U., Fendrich, J.A., Kwok, W.K., Crabtree, G.W. and Veal, B.W.: Thermodynamic evidence for a flux line lattice melting transition in $YBa_2Cu_3O_{7-delta}$. *Phys. Rev. Lett.*, 76: 4809-4812, 1996.

14. Schilling A., Fisher R. A., Phillips N. E., Welp U., Dasgupta D., Kwok W. K. and Crabtree G. W.: Calorimetric measurement of the latent heat of the vortex lattice melting in untwinned $YBa_2Cu_3O_{7-\delta}$. *Nature*, 382: 791-793, 1996.

15. Civale L., Marwick A. D., McElfresh M. W., Worthington T. K., Malozemoff A. P., Holtzberg F. H., Thomson J. R. and Kirk M. A.: Defect independence of the irreversibility line in proton-irradiated Y-Ba-Cu-O crystals. *Phys. Rev. Lett.*, 65; 1164-1167, 1990.

16. Giapintzakis J., Lee W. C., Rice J. P., Ginsberg D. M., Robertson I. M., Wheeler R., Kirk M. A., Ruault M.–O.: Production and identification of flux-pinning defects by electron irradiation in YBa2Cu3O7-x single crystals. *Phys. Rev. B*, 45: 10677-10683, 1992.

17. Civale L., Marwick A. D., Worthington T. K., Kirk M. A., Thompson J. R., Krusin–Elbaum L., Sun Y., Clem J. R., and Holtzberg F.: Vortex confinement by columnar defects in YBa2Cu3O7 crystals: Enhanced pinning at high fields and temperatures. *Phys. Rev. Lett.*, 67: 648-651, 1991.

18. Fasano Y., Herbsommer J. A., de la Cruz F., Pardo F., Gammel P. L., Bucher E., Bishop D. J.: Observation of periodic vortex pinning induced by Bitter decoration. *Phys. Rev. B*, 60: R15047-R15050, 1999.

19. Lyuksyutov I. F. and Pokrovsky V.: Magnetization controlled superconductivity in a film with magnetic dots. *Phys. Rev. Lett.* 81: 2344-2347, 1998.

20. Baert M., Metlushko V. V., Jonckheere R., Moshchalkov V., and Bruynseraede Y.: Composite flux-line lattices stabilized in superconducting films by a regular array of artificial defects. *Phys. Rev. Lett.*, 74: 3269-3272, 1995.

21. Bednorz J. G. and Muller K. A., *Z. Phys. B*, 64: 189, 1986.

22. Papst G., Gamble B. and Schottler M.: Development of synchronous motors and generators with HTS field windings. *The Third European Conference of Applied Superconductivity Netherlands*, 1997.

23. Salingaros N. A.: Optimal current distribution for energy storage in superconducting magnets. *J. Appl. Phys.*, 69: 531, 1991.

24. Gallop John: Microwave applications of high-temperature superconductors. *Supercond. Sci. Technol.*, 7A: A120-A141, 1997.

25. Larbalestier D. C., Cooley L. D., Rikel M. O., Polyanskii A. A., Jiang J., Patnaik S., Cai X. Y., Feldmann D. M., Gur A.: Strongly linked current flow in polycrystalline forms of the superconductor MgB_2. *Nature*, 410: 186–189, 2001.

26. Mazilu A., Safar H., Lopez D., Kwok W. K., Crabtree G. W., Guptasarma PHinks. D. G.: Experimental comparison of the effect that bulk pinning and surface barriers have on vortex motion in the vortex liquid state of $Bi_2Sr_2CaCu_2O_8$ single crystals. *Phys. Rev. B*, 58: R8913-R8916, 1998.

27. Mazilu A., Safar H., Maley M. P., Coulter J. Y., Bulaevskii L. N., and Foltyn S.: Vortex dynamics of heavy-ion-irradiated $YBa_2Cu_3O_{7-\delta}$: Experimental evidence for a reduced vortex mobility at the matching field. *Phys. Rev. B*, 58: R8909-R8912, 1998.

28. Guptasarma P. and Hinks D. G.: Floating zone growth and characterization of large high-quality single crystals of $Bi_2Sr_2CaCu_2O_x$ and control of oxygen stoichiometry. *Bull. Am. Phys. Soc.*, 42: 713, 1997.

29. Mochiku T. and Kadowaki K., *Trans. Mater. Res. Soc. Jpn.*, 19A: 349, 1993.

30. Kaiser D.L., Holtzberg F., Scott B.A. and McGuire T.R.: Growth of $YBa_2Cu_3O_x$ single crystals. *Appl. Phys. Lett.*, 51: 1040-1042, 1987.

31. Fleshler S., Kwok W.–K., Welp U., Vinokur V. M., Smith M. K., Downey J., and Crabtree G. W.: Anisotropy and Lorentz-force dependence of twin-boundary pinning and its effect on flux-lattice melting in single-crystal $YBa_2Cu_3O_{7-delta}$. *Phys. Rev. B*, 47: 14448–14461, 1993.

32. Kaiser D. L., Gayle F. W., Roth R. S., Swartzendruber L. J.: Thermomechanical detwinning of superconducting $YBa_2Cu_3O_{7-x}$ single crystals. *J. Mater. Res.*, 4: 745-747, 1989.

33. Welp U., Grimsditch M., You H., Kwok W.K., Fang M.M., Crabtree G. W. and Liu J.Z.: The upper critical field of untwinned $YBa_2Cu_3O_{7-\delta}$ Crystals. *Physica C*, 161: 1-5, 1989.

34. Ziegler J. F., Biersack J. P., and Littlemark U.: *The Stopping and Range of Ions in Solids*, New York, Pergamon, 1985.

35. Biersack J. P. and Ziegler J. F., http:// www.SRIM.org.

36. Cava R. J., Batlogg B., van Dorer R. B., Murphy D. W., Sunshine S., Siegrist T., Remeika J. P., Rietman E. A., Zahurak S., and Espinoza G. P.: Bulk superconductivity at 91 K in single-phase oxygen-deficient perovskite $Ba_2YCu_3O_{9-delta}$. *Phys. Rev. Lett.*, 58: 1676-1679, 1987.

37. Palstra T. T. M., Batlogg B., Schneemeyer L. F., van Dorer R. B., and Waszczak J. V.: Angular dependence of the upper critical field of $Bi_{2.2}Sr_2Ca_{0.8}Cu_2O_{8+delta}$. *Phys. Rev. B*, 38: 5102-5105, 1988.

38. Szenes G.: Formation of columnar defects in high-T_c superconductors by swift heavy ions. *Phys. Rev. B*, 54: 12458-12463, 1996.

39. Wheeler R., Kirk M. A., Brown R., *Materials Research Society Symposium Proceedings*, pp. 683, 1992.

40. Fleischer R. L., Price P. B., and Walker R. M.: Ion explosion spike mechanism for formation of charged –particle tracks in solids. *Journal of Applied Physics*, 36: 3645-3652, 1965.

41. Schiwietz G., *NATO ASI Series B*, edited by R. A. Baragiola, vol. 306, pp. 197-214, New York, Plenum Press, 1993.

42. Bean C. P. and Livingston J. D.: Surface Barrier in Type-II Superconductors. *Phys. Rev. Lett.*, 12: 14-16, 1964.

43. Fuchs D. T., Zeldov E., Rappaport M., Tamegai T., Ooi S., Shtrikman H.: Transport properties governed by surface barriers in $Bi_2Sr_2Ca_2CuO_8$. *Nature* (London), 391: 373-376, 1998.

44. Shaw M. P. and Solomon P. R.: Flux-Flow Resistivity in a Superconducting Disk. *Phys. Rev.*, 164: 535-537, 1967.

45. Lopez D., Kwok W. K, Safar H., Olsson R. J., Petrean A. M., Paulius L., and Crabtree G. W.: Spatially resolved dynamic correlation in the vortex state of high temperature superconductors. *Phys. Rev. Lett.*, 82: 1277-1280, 1999.

46. Rycroft S. F. W. R, Doyle R. A., Fuchs D. T., Zeldov E., Drost R. J., Kes P. H., Tamegai T. and Ooi S., Foord D. T.: Bulk transport properties of $Bi_2Sr_2CaCu_2O_8$ crystals in the Corbino disk geometry. *Phys. Rev. B*, 60: R757-R760, 1999.

47. Mirkovic J., Kadowaki K.: Nonlinear resistivity in vortex liquid and surface barriers in single crystals $Bi_2Sr_2CaCu_2O_{8+\delta}$. *Physica B*, 284-288: 759-760, 2000.

48. Eltsev Y., Nakao K., Shibata S., Koshizuka N.: Transverse dynamic vortex correlation in a $Bi_2Sr_2CaCu_2O_{8+\delta}$ Corbino disk. *Physica C*, 341-348: 1107-1108, 2000.

49. Bardeen J. and Stephen M.J.: Theory of the motion of vortices in superconductors. *Phys. Rev.*, 140: A1197-A1207, 1965.

50. Kopnin N. B. *et al.*, *JETP Lett.*, 23: 578, 1976.

51. Iye Y. *et al.*: Hall effect in high temperature superconductors near T_c. *Physica C* (Amsterdam), 159: 616-624, 1989.

52. Marchetti M. Cristina and Nelson David R.: Hydrodynamics of flux liquids. *Phys. Rev. B*, 42: 9938-9943, 1990.

53. Marchetti M. Cristina and Nelson David R.: Patterned geometries and hydrodynamics at the vortex Bose glass transition. *Phys. Rev. B*, 59: 13624-13627, 1999.

54. Koshelev A.E.: Mechanism of thermally activated c-axis dissipation in layered high-T_c superconductors at high fields. *Phys. Rev. Lett.*, 76: 1340-1343, 1996.

55. Busch R., Ries G., Werthner H., Kreiselmeyer G., Saemann-Ischenko G.: New aspects of the mixed state from six-terminal measurements on Bi2Sr2CaCu2Ox single crystals. *Phys. Rev. Lett.*, 69: 522-525, 1992.

56. Fendrich, J.A., Welp, U., Kwok W. K., Koshelev A. E., Crabtree G. W., and Veal B. W.: Static and Dynamic Vortex Phases in $YBa_2Cu_3O_{7-delta}$. *Phys. Rev. Lett.*, 77: 2073-2076, 1996.

57. Kadowaki K. and Kimura K.: Precise magnetization measurements of single crystalline $Bi_2Sr_2CaCu_2O_{8+\delta}$. *Phys. Rev. B*, 57: 11674-11683, 1998.

58. Bean C. P.: Magnetization of hard superconductors. *Phys. Rev. Lett.*, 8: 250-253, 1962.

59. Kazumata Y., Kumakura H. and Togano K.: Vortex pinning in $Bi_2Sr_2CaCu_2O_8$ tapes irradiated by ions. *Phys. Rev. B*, 54: 16206-16210, 1996.

60. Zeldov E., Larkin A. I., Geshkenbein V. B., Konczykowski M., Majer D., Khaykovich B., Vinokur V. M., and Shtrikman H.: Geometrical barriers in high-temperature superconductors. *Phys. Rev. Lett.*, 73: 1428-1431, 1994.

61. Palstra T. T. M., Batlogg B., Schneemeyer L. F., and Waszczak J. V.: Thermally activated dissipation in $Bi_{2.2}Sr_2Ca_{0.8}Cu_2O_{8+delta}$. *Phys. Rev. Lett.*, 61: 1662-1665, 1988.

62. Zeldov, E., Majer, D., Konczykowski, M., Geshkenbein, V.B., Vinokur, V.M. and Shtrikman, H.: Thermodynamic observation of first-order vortex-lattice melting transition in $Bi_2Sr_2CaCu_2O_8$. *Nature*, 375: 373-377, 1995.

63. Fendrich, J.A., Kwok, W.K., Giapintzakis, J., Beek, C.J.v.d., Fleshler, S., Welp, U., Viswanathan, H.K., Downey, J. and Crabtree, G.W.: Vortex liquid state in an electron irradiated untwinned $YBa_2Cu_3O_{7-delta}$ crystal. *Phys. Rev. Lett.*, 74: 1210-1213, 1995.

64. Fisher, Matthew P.A.: Vortex-glass superconductivity: A possible new phase in bulk high-T_c oxides. *Phys. Rev. Lett.*, 62: 1415-1418, 1989.

65. Nelson, D.R. and Vinokur, V.M.: Boson localization and pinning by correlated disorder in high-temperature superconductors. *Phys. Rev. Lett.*, 68: 2398-2401, 1992.

66. Nelson, D.R. and Vinokur, V.M.: Boson localization and correlated pinning of superconducting vortex arrays. *Phys. Rev. B*, 48: 13060-13097, 1993.

67. Hwa, T., Doussal, P.L., Nelson, D.R. and Vinokur, V.M.: Flux pinning and forced vortex entanglement by splayed columnar defects. *Phys. Rev. Lett.*, 71: 3545-3548, 1993.

68. Blatter, G., Feigel'man, M.V., Geshkenbein, V.B., Larkin, A.I. and Vinokur, V.M., *Rev. Mod. Phys.*, 66: 1125, 1994.

69. Oussena M., de Groot P. A. J., Porter S. J., Gagnon R., and Taillefer L.: Vortex channeling along twin planes in YBCO. *Phys. Rev. B*, 51: 1389-1392, 1995.

70. Yan Y. and Kirk M. A.: Observation and mechanism of local oxygen reordering induced by high-energy heavy-ion (U + , Au + , Xe +) irradiation in the high-T_c superconductor $YBa_2Cu_3O_{7-\delta}$. *Phys. Rev. B*, 57: 6152-6164, 1998.

71. Willemin M., Schilling A., Keller H., Rossel C., Hofer J., Welp U., Kwok W. K., Olsson R. J., and Crabtree G. W.: First-order vortex-lattice melting transition in $YBa_2Cu_3O_{7-\delta}$ near the critical temperature detected by magnetic torque. *Phys. Rev. Lett.*, 81: 4236-4239, 1998.

72. Pippard A. B.: A possible mechanism for the peak effect in type II superconductors. *Philosophical Magazine*, 19: 217-220, 1969.

73. Kwok W. K., Olsson R. J., Karapetrov G., Paulius L. M., Moulton W. G., Hofman D. J., and Crabtree G. W.: Critical points in heavy ion irradiated untwinned $YBa_2Cu_3O_{7-\delta}$ crystals. *Phys. Rev. Lett.*, 84: 3706-3709, 2000.

74. Klein L., Yacoby E. R., Wolfus Y., Yeshurun Y., Burlachkov L., Shapiro B. Y., Konczykowski M., and Holtzberg F.: Flux flop in Y-Ba-Cu-O crystals irradiated with 5.3-GeV Pb ions. *Phys. Rev. B*, 47: 12349-12352, 1993.

75. Abrikosov A. A.: The magnetic properties of superconducting alloys. *J. Phys. Chem. Solids*, 2: 199-208, 1957.

76. Pruymboom A., Kes P. H., van der Drift E., Radelaar S.: Flux-line shear through narrow constraints in superconducting films. *Phys. Rev. Lett.*, 60: 1430-1433, 1988.

77. Pastoriza H. and Kes P. H.: Direct shear probe of vortex lattice melting in $Bi_2Sr_2CaCu_2O_8$ single crystals. *Phys. Rev. Lett.*, 75: 3525-3528, 1995.

78. Theunissen M.H., Van der Drift E., and Kes P. H.: Size effects in flow of flux-line solids and liquids. *Phys. Rev. Lett.*, 77: 159-162, 1996.

79. Marchetti M. C.: Driven vortices in confined geometry: the Corbino disk. *Physica C*, 341-348: 991-994, 2000.

80. Zech D., Lee S.L., Keller H., Blatter G., Kes P. H., Li T. W.: Phase diagram of Bi2.15Sr1.85CaCu2O8+ delta in the presence of columnar defects. *Phys. Rev. B*, 54: 6129-6132, 1996.

81. Klein L., Yacoby E. R., Yeshurun Y., Konczykowski M. and Kishio K.: Evidence for line vortices in $Bi_2Sr_2CaCu_2O_8$. *Phys. Rev. B*, 48: 3523-3526, 1993.

82. Seow W. S., Doyle R. A., Campbell A. M., Balakrishnan G., McK. Paul D., Kadowaki K., Wirth G.: Influence of columnar defects on vortex dynamics in $Bi_2Sr_2CaCu_2O_8$ from out-of-plane and flux transformer transport measurements. *Phys. Rev. B*, 53: 14611-14620, 1995.

83. Zech D., Lee S. L., Keller H., Blatter G., Janossy B., Kes P. H., Li T. W., Menovsky A. A.: Correlation of flux lines in single-crystal $Bi_2Sr_2CaCu_2O_8$ with columnar defects. *Phys. Rev. B*, 52: 6913-6919, 1995.

VITA

NAME: Ana Mazilu

EDUCATION: B.S., Physics, University of Bucharest, Bucharest, Romania, 1996

M.S., Physics, University of Illinois at Chicago, Chicago, Illinois, 2000

TEACHING EXPERIENCE: Department of Physics, University of Illinois at Chicago, Chicago, Illinois: Physics 101 and 144 Laboratories, 1996-1997

HONORS: Paul Raccah award for best achievement in the Preliminary Doctorate Exam at the Department of Physics, University of Illinois at Chicago, Chicago, Illinois, 1997.

European Physical Society scholarship, Bucharest, Romania, 1995-1996.

PROFESIONAL MEMBERSHIP: American Physical Society since 1997

ABSTRACTS: Mazilu A., Lopez D., Kwok W. K., Kadowaki K., Crabtree G.W.: Non-uniform force induced vortex dynamics in BiSrCaCuO8 single crystals. *Bull. Am. Phys. Soc.*, 44: 1929, 1999.

Mazilu A., Kwok W. K., Crabtree G. W., Zhao Y.: Evidence of vortex shear viscosity in BSCCO Corbino disk. *Bull. Am. Phys. Soc.*, 46: 517, 2001.

Kwok W. K., Mazilu A., Olsson R.J., Crabtree G. W.: Behavior of the vortex liquid state near the upper critical point in YBCO. *Bull. Am. Phys. Soc.*, 46: 174, 2001.

Tobos V., Paulius L.M., Petrean A.M., Olsson R.J., Mazilu A., Kwok W. K., Crabtree G. W.: Effects of columnar defects on the phase diagram of YBCO single crystals. *Bull. Am. Phys. Soc.*, 46: 175, 2001.

PUBLICATIONS: Mazilu A., Safar H., Maley M. P., Coulter J. Y., Bulaevskii L. N., and Foltyn S.: Vortex dynamics of heavy-ion-irradiated $YBa_2Cu_3O_{7-\delta}$: Experimental evidence for a reduced vortex mobility at the matching field. *Phys. Rev. B,* 58: R8909, 1998.

Mazilu A., Safar H., Lopez D., Kwok W. K., Crabtree G. W., Guptasarma PHinks. D. G.: Experimental comparison of the effect that bulk pinning and surface barriers have on vortex motion in the vortex liquid state of Bi,Sr,CaCu,O, single crystals. *Phys. Rev. B,* 58: R8913, 1998.